Title
Direct concentrated solar synthesis of graphene

Author
Alghfeli, Abdalla Mohamed Ahmed Saif

Publication Date
2022

Peer reviewed|Thesis/dissertation

UNIVERSITY OF CALIFORNIA

Los Angeles

Direct concentrated solar synthesis of graphene

A dissertation submitted in partial satisfaction

of the requirements for the degree

Doctor of Philosophy in Mechanical Engineering

by

Abdalla Mohamed Ahmed S Alghfeli

2022

ABSTRACT OF THE DISSERTATION

Direct concentrated solar synthesis of graphene

by

Abdalla Mohamed Ahmed S Alghfeli

Doctor of Philosophy in Mechanical Engineering

University of California, Los Angeles, 2022

Professor Timothy S. Fisher, Chair

Fabrication of electronic materials typically require intensive energy, even when its predominant use is heating. Such energy is usually derived from local utilities that harness fossil fuels, nuclear power, wind, and solar photovoltaics, among other resources. Thus, direct solar-thermal capture provides a compelling option to drive heating processes, reducing greenhouse gas emissions from the industrial sector. Graphene is one of numerous materials of heightened interest in the semiconductor and energy conversion industries. It consists of carbon atoms arranged in a two-dimensional hexagonal structure. Graphene's exceptional properties make it applicable to many photonic and electronic devices. Several approaches have been employed to synthesize graphene; however, chemical vapor deposition (CVD) is mostly used, consuming high energy using plasma or electric heating sources. Nevertheless, CVD techniques provide an effective methodology for mass production by roll-to-roll mechanisms and control of graphene's number of layers and quality through growth kinetics.

Here, a high-flux solar simulator (HFSS) that mimics the sun's spectrum was built to study solar-thermal energy in graphene fabrication. A simple, accurate, and inexpensive methodology is necessary to characterize the HFSS radiative flux. In this work, an inverse mapping technique that uses a custom radiometer and infrared camera, validated by a direct characterization method (heat flux gauge), is used to characterize the output from a 10 kW_e xenon lamp solar simulator. The heat flux profile is determined in a vacuum chamber using a readily available graphite target and an inverse numerical heat transfer model. Such an approach allows characterization in practical conditions, such as inside the reactor and including effects from the viewport. Results indicate that the solar simulator produces peak fluxes in the 1.5-4.5 MW/m^2 range, and its output can be controlled using a variable power supply. The HFSS is then integrated into a cold-wall CVD reactor equipped with a gas supply and vacuum auxiliaries, automated with precise controls and safety interlocks to monitor graphene growth parameters. A related numerical heat transfer model of a copper substrate atop a tungsten mount is derived and validated to predict the peak temperature at various HFSS supply currents and vacuum pressures, facilitating graphene growth under different conditions.

A parametric study of graphene growth parameters was conducted using a probabilistic Bayesian regression model. The regression model utilizes Gaussian processes and an information acquisition function to find conditions that yield high-quality graphene products. Characterization tools such as backscattered electron images and Raman mapping were employed to assess the effects of growth conditions on graphene film quality, uniformity, and preferential graphene growth characteristic size. We report the synthesis of high-quality single-layer graphene (SLG) and AB-stacked bilayer graphene films with I_D/I_G of 0.21 and 0.14, respec-

tively. Synthesis was carried out in a one-step and short-time process of 5 min. Electron diffraction analysis illustrates peak intensities resembling SLG and AB-bilayer graphene with up to 5 and 20 μm grain sizes, respectively. The measured optical transmissivity of SLG and AB-bilayer graphene in this work falls in the 0.959-0.977 and 0.929-0.953 ranges. Additionally, the sheet resistances by a 4-point probe with 1 mm spacing were measured as 15.5±4.6 and 3.4±1.5 kΩ/sq, respectively.

To exploit graphene's extraordinary properties, mass production methods are warranted. By flattening the heat flux profile, a larger area on the copper substrate reaches a temperature of 1060℃, enabling larger-area graphene synthesis. Synthesis of high-quality (I_D/I_G = 0.13) AB-stacked bilayer graphene has been achieved with greater than 90% coverage in a one-step and short time process of 5 min. Synthesized graphene exhibits spatial uniformity over a large area up to 20 mm in radius with large grain sizes up to 20 μm. Graphene film transmissivity and sheet resistance fall in the 92.8-95.3% and 2-4 kΩ/sq range, respectively. However, a roll-to-roll mechanism in solar-thermal chemical vapor deposition is necessary for scaling-up graphene growth. Moderate-quality (I_D/I_G of 0.7) films were achieved at a speed of 200 mm/min with at least 72% SLG coverage suitable as transparent conductive electrodes. Lower-quality graphene synthesized in this work can still be applied as an oxidation barrier for metals. Therefore, direct-solar capture provides a compelling option to harvest a renewable energy resource and drive graphene synthesis.

The dissertation of Abdalla Mohamed Ahmed S Alghfeli is approved.

Laurent Pilon

Mitchell Spearrin

Richard Kaner

Timothy S. Fisher, Committee Chair

University of California, Los Angeles

2022

Contents

List of Figures

List of Tables

Acknowledgments

I would like to express my gratitude and appreciation to my advisor, Prof. Timothy Fisher, for his tremendous support and encouragement. His guidance, throughout each step, played an essential role in extending my knowledge and defining my research path. His inspiration made me passionate about this topic, achieve this work objective and progress in my academic and personal life. I would also like to thank the following whose contribution to this research development is highly appreciated:

- Prof. Laurent Pilon, Prof. Mitchell Spearrin, and Prof. Richard Kaner for their support, insightful feedback, and involvement in my research and academic development.

- Members of Nanoscale Transport Research Group (NTRG), especially Mostafa Abuseada and Akshay Bharadwaj Krishna, for their prompt help and constant support. Mostafa Abuseada helped greatly in building the lab's infrastructure and the high flux solar simulator with its characterization methodology.

- Adam Z. Stieg, Sergey Prikhodko, and Matthew Mecklenburg for their support and training in using imaging and spectroscopy equipment.

- Members of the Mechanical and Aerospace department, especially Miguel, Ben, Anthony, Amanda, and Marla, for their help and support.

- California NanoSystems Institute at UCLA and its Noble Family Innovation Fund for the support of this work.

- United Arab Emirates University for a doctoral fellowship.

Finally, I would like to thank my mom; Nawal, sisters; Fatima and Eman, aunties; Fatima, Salwa, and Ameera, uncle; Abdulwahid, and Jen, for their undying love, support, and encouragement. Thanks to my father; Mohamed, although the path you guided me towards was hard but I would not have made it to where I am today without it. A special thanks to my cousins and friends.

Vita

Education

Master of Science in Mechanical and Aerospace Engineering 2016 - 2018

University of Florida, Gainesville, USA

Bachelor of Science in Mechanical Engineering 2009 - 2004

American University of Sharjah, Sharjah, UAE

Journal publications

Mostafa Abuseada, **Abdalla Alghfeli**, and Timothy S. Fisher, "Indirect inverse flux mapping of a concentrated solar source using infrared imaging", Review of Scientific Instruments 93, 073101 (2022) https://doi.org/10.1063/5.0090855

Abdalla Alghfeli, Mostafa Abuseada, and Timothy S. Fisher, "Solar-thermal cold-wall chemical vapor deposition reactor design and characterization for graphene synthesis", Journal of Vacuum Science & Technology B 40, 064205 (2022) DOI: 10.1116/6.0002091

Abdalla Alghfeli and Timothy S. Fisher, "High-quality AB bilayer graphene films by direct solar-thermal chemical vapor deposition", ACS Sustainable Chemistry & Engineering, Under review

Abdalla Alghfeli and Timothy S. Fisher, "Sequential Bayesian-optimized graphene synthesis by direct solar-thermal deposition", In preparation

Abdalla Alghfeli and Timothy S. Fisher, "Scalable graphene production by solar-thermal roll-to-roll chemical vapor deposition", In preparation

Mostafa Abuseada, **Abdalla Alghfeli**, and Timothy S. Fisher, "Graphitic surface layer formation on organic substrates for electronics using a concentrated solar simulator", MRS Advances (2022). https://doi.org/10.1557/s43580-022-00339-7

Yuan Hu, Mostafa Abuseada, **Abdalla Alghfeli**, Saurin Holdheim, and Timothy S. Fisher, "High-Temperature Thermal Diffusivity Measurements Using a Modified Ångström's Method With Transient Infrared Thermography.", ASME. J. Heat Transfer. February 2022; 144(2): 023502. https://doi.org/10.1115/1.4053108

Chapter 1: Introduction and outline

1.1 Introduction: Motivation and thesis purpose

Graphene consists of carbon atoms arranged in a two-dimensional honeycomb lattice structure [1] whose thickness varies between one and a few stacked layers. Its exceptional properties include high thermal and electrical conductivities [1, 2], optical transmissivity [3], excellent chemical stability [4], and high mechanical flexibility [5] and strength [6]. Consequently, graphene has been studied in many energy conversion and storage applications such as flexible solar cells [5, 7], sunlight-activated transparent electrodes [4], supercapacitors [8–10], lithium-ion batteries [10, 11] and water splitting processes [10]. In addition, Bernal-stacked ("AB") bilayer graphene has a tunable bandgap by an external electric field that can be employed for transistor applications [12, 13]. Graphite exfoliation techniques by liquid-phase [14] and shear-mixing [15] processes can potentially scale up graphene production for industrial needs. For example, graphene production by exfoliation using tannic acid in an aqueous medium has been developed with an efficient methodology [16]. However, chemical vapor deposition (CVD) remains the most efficient method for mass production by employing roll-to-roll processing [17, 18].

Despite graphene's use in many sustainable energy applications, its synthesis process is ecologically and economically costly. Graphene synthesis, specifically by CVD, consumes high energy whether using plasma or electric heating sources. Semiconductor industries are also known for intensively using CVD techniques to deposit thin films and etch wafers, consuming high energy and polluting the environment. Studies have shown that the semicon-

ductor industry contributes up to 2% of the manufacturing sector's electricity consumption in the US [19], where such expenses contribute up to 40% of fabrication costs [20]. Additionally, large semiconductor fabrication plants consume up to 100 MWh of energy each hour [20], and approximately 0.386 kg of carbon dioxide is released per kWh [21].

In 2020, CVD technologies in the semiconductors and microelectronics industries were found to contribute up $14-15 billion to the US economy and were associated with up to 62% of total market revenues [22]. Nevertheless, electrical energy consumption and CO_2 emissions for 300 mm wafer fabrication were estimated to be 1400 kWh/wafer and 300 kg/wafer [22], respectively, and continue to increase with new technologies to achieve smaller Moore's law nodes. For a typical CVD reactor, the heater and electronic instruments consume about 3-3.5 kW, whereas plasma reduces consumption to 1 kW [22]; however, extra energy is required for supplemental heating and plasma processes.

Many prior studies have used plasma CVD to synthesize single layer graphene (SLG) [18, 23] and free-standing graphene layers [24]. Others have focused on manufacturing supercapacitors and electrode materials such as bioinspired micro-conduits [8] and polygonal carbon nanofibers [9]. One important feature of plasma CVD is that it allows graphene synthesis at relatively low temperatures [18, 24]. It also provides localized heating without physical contact and thus enables the scale-up of graphene synthesis through fast roll-to-roll processes [17, 18]. However, plasma often requires specific flow conditions of inert gases such as Ar or N_2 for arc stabilization, and the resulting ion impingement adversely affects graphene quality [18, 25].

Hot-wall furnace CVD with electric heating, yet another thermal source, offers the ability to synthesize high-quality SLG and bilayer graphene films as well [13, 26–31]. However, this

approach requires additional time-consuming procedures, such as long pre-heating of the entire reactor. In contrast, cold-wall CVD, which provides localized electric heating and reduced synthesis time, has been employed to produce high-quality graphene layers on Cu [25, 32–34] and Ni [34–36] foils suitable for electronic and photonic applications. Therefore, utilizing solar heating provides an opportunity to harvest a renewable energy resource with higher electromagnetic radiant energy flux than infrared sources to heat a sample locally in a short time without physical substrate contact or the need for a stabilizing medium.

A custom-designed high flux solar simulator (HFSS), which closely approximates the solar spectrum [37], has been built to achieve the objectives of this research. At first, its output heat flux profile on the target plane has been characterized [38] by solving an indirect inverse heat transfer model using infrared temperature imaging of a readily available graphite sample. Afterward, the HFSS was integrated into a custom-built CVD system [39] equipped with a cold-wall reactor, gas supply system, vacuum auxiliaries, and automated controls to enable graphene growth on copper substrates. A related numerical heat transfer model for a copper substrate has been derived and validated [39] at various conditions with temperature measurements acquired by a pyrometer. Varying the temperature of the substrate (by controlling the HFSS power supply) is one of the most crucial parameters in graphene growth. Other design parameters in graphene synthesis are gas ratio (CH_4/H_2), vacuum pressure, and residence time.

A probabilistic Bayesian regression model [40] using Gaussian processes and an information acquisition function has been employed to deal with the stochastic single-objective (I_D/I_G) optimization and to determine new experimental conditions. Hence, experiments were carried out based on the proposed design parameters, increasing the model's confidence

about conditions that yield better graphene quality. Such an algorithm was solved iteratively until process optimization or a threshold value was achieved. Synthesized graphene films on copper were analyzed with Raman spectroscopy to assess their quality by measuring the intensity ratio of graphene lattice defects to C-C in-plane vibrations [41], which serves as the objective function being optimized. Scanning and transmission electron microscopy were also acquired to study graphene's uniformity, grain sizes, and lattice structure. Characterization tools have demonstrated the synthesis of high-quality monolayer and AB-stacked graphene in this work.

Further scale-up of graphene synthesized at optimized conditions can be achieved by displacing the lamp 4.8 mm towards the target, out of its focal plane, to flatten the heat flux and achieve a more uniform profile. Therefore, a larger area on the copper substrate reaches a uniform temperature of 1060±10℃, but at the expense of consuming more power by the HFSS. Based on Raman measurements (I_D/I_G ratio), spatial uniformity up to 20 mm in radius was achieved, which represents one order of magnitude increase in graphene area.

Graphene mass production has been achieved by modifying the solar-thermal CVD design with a roll-to-roll mechanism and studying the effect of various conditions. Results show moderate-quality graphene suitable as transparent conductive electrodes [18], where lower-quality can be applicable as metals oxidation barrier [17, 42]. However, synthesizing graphene on a conductive catalyst such as a copper foil generally introduces a limiting factor in achieving high-quality products. The aforementioned limit is due to the deposition of lower-quality graphene grade at low temperatures [43] in the upstream foil prior to reaching the HFSS focal point. To improve the quality of roll-to-roll graphene, synthesis at different CH_4:H_2 concentrations and web speeds has been studied alongside design modifications to

add a tungsten slit to lower the temperatures upstream below graphene nucleation limits [44] by enhancing conduction heat transfer. Additionally, the slit polishes the surface and peels off lower-quality graphene prior to reaching the growth zone. Thus, using a heat source that approximates the solar spectrum provides new understanding and methodology to enable green solar manufacturing as a compelling option in the semiconductor industry.

1.2 Outline

Chapter 2 illustrates solving the indirect inverse flux mapping of a concentrated solar source using infrared imaging. Solar-thermal cold-wall chemical vapor deposition (CVD) reactor design and thermal modeling are demonstrated in Chapter 3. Chapter 4 explains the sequential Bayesian-optimized graphene synthesis by direct solar-thermal deposition. Using solar-thermal CVD, Chapter 5 describes a scalable graphene production by flattening the heat-flux profile to achieve a large-area synthesis of AB-stacked graphene films, and Chapter 6 shows employing a roll-to-roll mechanism for mass production.

Chapter 2: Indirect inverse flux mapping of a concentrated solar source using infrared imaging*

With the growing interest in high-flux solar sources, a need exists for simple, accurate, and inexpensive strategies to characterize their output radiative flux. In this chapter, the irradiation output from a 10 kW_e xenon lamp solar simulator is characterized by an inverse mapping technique that uses a custom radiometer and infrared camera, validated by a direct characterization method (heat flux gauge). The heat flux distribution is determined in a vacuum chamber using an easily obtainable graphite target and an inverse heat transfer model. The solar simulator produces peak fluxes in the range of 1.5-4.5 MW/m^2 as measured directly by a heat flux gauge, and its output can be controlled using a variable power supply. Spectral measurements indicate that minor variations in the simulator's output with respect to its current supply occur in the spectral range of 450-800 nm. The radiometer presented in this work allows for characterizing solar irradiation under practical conditions (e.g., inside a solar reactor) and thus accounts for deviations due to additional components, such as viewport effects. Additionally, it provides an inexpensive and efficient means of monitoring any deterioration in performance of solar sources over time without the need for complex recalibration.

* This chapter was written in equal contribution with M. Abuseada, and created the paper by Mostafa Abuseada, Abdalla Alghfeli, and Timothy S. Fisher , "Indirect inverse flux mapping of a concentrated solar source using infrared imaging", Review of Scientific Instruments 93, 073101 (2022). DOI: 10.1063/5.0090855

2.1 Introduction

High flux solar simulators (HFSSs) provide highly controllable and adjustable radiation that mimics the sun's spectral irradiance [37]. They provide a platform to conduct a wide range of experiments, which include producing solar fuels and commodities [45, 46], testing photovoltaic devices [47], processing materials under high irradiation fluxes [48], and characterizing thermal properties at high temperatures [49]. A HFSS consists of a single or multiple high-power lamps as the radiative source, where each is placed within its own truncated reflector, usually ellipsoidal, to concentrate radiation onto a single focal plane or target. The most common type of lamp used in prior work is the xenon short arc, while metal halide and argon lamps are alternatives [50]. By varying the current input to the lamps, their arrangement, and focus, the output power and distribution from a HFSS can be tailored to fit a variety of experimental needs.

As interest in using HFSSs for research grows, developing simple, accurate, and inexpensive strategies to characterize their output irradiation is warranted. This characterization not only indicates the thermal performance of the HFSS, but also provides thermal input parameters required for energy balance and efficiency calculations [51]. The current state-of-the-art method used for characterizing HFSSs involves an indirect grayscale heat flux mapping approach with minor variations in the experimental methodology and equipment incorporated [52–55]. Briefly, a heat flux gauge (HFG) [52, 56, 57] or equivalent [54] is used to calibrate a CCD or CMOS grayscale camera correlated to images of a water-cooled Lambertian (diffusely reflecting) target's illuminated front face with heat flux measurements. Once the grayscale camera is calibrated, the light source can be aligned, optimized, and

characterized across different planes using a two or three-dimensional sliding stage. In the usual manner, the HFG measurements and grayscale images are obtained using two different setups. However, slight misalignment can occur during the transition between setups and can lead to changes in the peak heat flux values as high as 6% [58].

To eliminate the setup transition and to reduce characterization time, a smaller uncooled 3 mm thick movable Lambertian target can be used to cover the HFG mounted at the center of a Lambertian target [59]. However, the uncooled target is subject to deterioration under high irradiation, which can significantly alter the grayscale camera correlation. Alternatively, the target can be moved away from its center to capture a smaller, but large enough, uninterrupted continuous area, and post-processing tools can be used to create a larger flux map by superposition [52]. The linear relationship between heat flux and grayscale values in addition to the inverse grayscale method's accuracy in instantly mapping the heat flux distribution makes it the most common in literature. However, any indirect grayscale mapping method suffers from high cost due to requiring a separately dedicated experimental configuration and additional expensive and uncommon thermal equipment (e.g., water-cooled Lambertian target and grayscale camera) to characterize and regularly monitor HFSS performance.

Apart from indirect grayscale heat flux mapping, researchers have attempted to characterize HFSSs using other techniques. For example, sources have been characterized directly using a thermogage [60] or a thermopile flux sensor [61] to measure heat flux values at discrete points in a plane using sliding stages that scan the area of interest to generate a heat flux map. This approach potentially provides measurements with a higher accuracy than the indirect grayscale mapping technique because it avoids calibration errors associated with additional equipment (mainly the grayscale camera), such as perspective shape distortion er-

rors [52, 54]. However, the direct method is time-consuming, especially for properly aligning the HFSS, and it provides a low map resolution as a result of the discrete captured locations.

A comparison among three different HFSS characterization techniques was performed by Garrido et al. [62]: a radiometer based on a thermopile sensor, a large flat-plate calorimeter to obtain total power, and the indirect grayscale heat flux mapping method. Through uncertainty analysis, the authors concluded that the indirect grayscale mapping method was not appropriate for characterizing the output from their Fresnel lens-based HFSS, and that the approach of coupling radiometer and calorimeter measurements improves characterization accuracy. Alternatively, a HFSS was characterized with an inexpensive experimental setup by obtaining transient temperature maps of a target placed in the plane of interest to determine the corresponding heat flux map via an inverse method [63]. Temperatures of the 0.8 mm thick stainless steel target were recorded using an infrared (IR) camera placed off the target's optical axis and facing its black painted front (illuminated) or back side, depending on the heat flux magnitudes (due to method limitations). Validation of the transient inverse method was presented away from the focal plane with relatively low heat flux values (up to 7 kW/m^2) to avoid deterioration of the front side's black paint. To map higher heat flux distributions at the focal plane, transient temperatures of the target's rear side were monitored up to 300 °C with a peak flux of 1.3 MW/m^2. However, solving an inverse transient problem that additionally includes an unaccounted temperature gradient between the front and back surfaces can induce significant errors.

The determination of heat flux, thermal properties, and volumetric heat generation can be realized by solving an inverse problem with different minimization algorithms. An iterative minimization solver based on the Broyden–Fletcher–Goldfarb–Shanno (BFGS) al-

gorithm with a simple step method was used to compute temperature-dependent thermal conductivity and specific heat from thermocouple measurements [64]. Others used methods of steepest descent and conjugate gradients to characterize heat transfer parameters such as surface/boundary heat flux [65, 66], convection coefficient [66], body surface temperature [66], and volumetric heat generation [67]. Non-iterative approaches were also introduced to determine thermal properties either by employing an integral method [68, 69], or by transforming the heat transfer differential governing equations into a linear matrix [70]. For solar systems, the heat flux distribution has been mapped by solving an inverse problem with a sensitivity matrix methodology [71, 72], golden section search method [63], and Levenberg-Marquardt algorithm [73] from IR camera temperature measurements. Although, generally, in-house numerical models have been developed for inverse problems, the incorporation of commercial software such as ANSYS is also possible [72, 73].

Using any of the aforementioned techniques, the heat flux distribution can be characterized at the focal plane but, due to practical considerations, the flux cannot be determined under the actual conditions of intended experimentation, such as on a substrate in a reactor/vacuum chamber [46]. Although numerical models such as Monte Carlo ray tracing (MCRT) can be fitted to experimental measurements of the HFSS and used to compensate for additional components, such as quartz windows and reactor cavity [74, 75], significant errors may arise.

Therefore, in this work, the heat flux from a 10 kW_e xenon short arc lamp HFSS is characterized inside a vacuum chamber using an inverse mapping technique with IR thermography. A readily obtainable sample of known properties is placed inside the vacuum chamber and used as a radiometer to measure the irradiation distribution on a target under

similar conditions. In contrast to prior literature, the camera is placed normal to the target to avoid errors associated with off-axis placement, and steady-state temperature measurements are used to increase the robustness of the inverse methodology. Additionally, the methodology targets characterizing solar sources with moderate to high heat flux distributions as compared to limited irradiation concentration in prior work [63], and with the potential of facile in-house and routine calibration (without requiring a sample of well-known properties) [49]. The accuracy of results obtained by this inverse technique is evaluated, and results are compared to two other independent methods: measurements recorded using a HFG and simulation results from a validated MCRT in-house code.

2.2 Experimental setup and procedure

2.2.1 High flux solar simulator

The custom-designed and built HFSS assembly shown in Fig. 2.1 encompasses a 10 kW_e xenon short arc lamp (Superior Quartz, SQP-SX100003) aligned at the first focal point of a truncated ellipsoidal reflector (Optiforms, E1023F). The aluminum reflector has two focal points at 7.49 and 102.3 cm from the ellipsoid's vertex and is coated with silver to enhance its reflective properties. The reflector is truncated at a diameter of 10.0 cm to allow for lamp placement at the first focal point without interference, and the reflector ends at a diameter of 38.7 cm. The HFSS is also equipped with a variable power supply to control the output power of the lamp by varying its supply current over the range of 100-200 A. The assembly is equipped with intake and exhaust fans to maintain proper cooling of the lamp. An IR temperature sensor (OMEGA, OS151-HT-K) is used to monitor the cathode's end seal temperature and to ensure that it remains below 200 °C. Finally, the HFSS is equipped

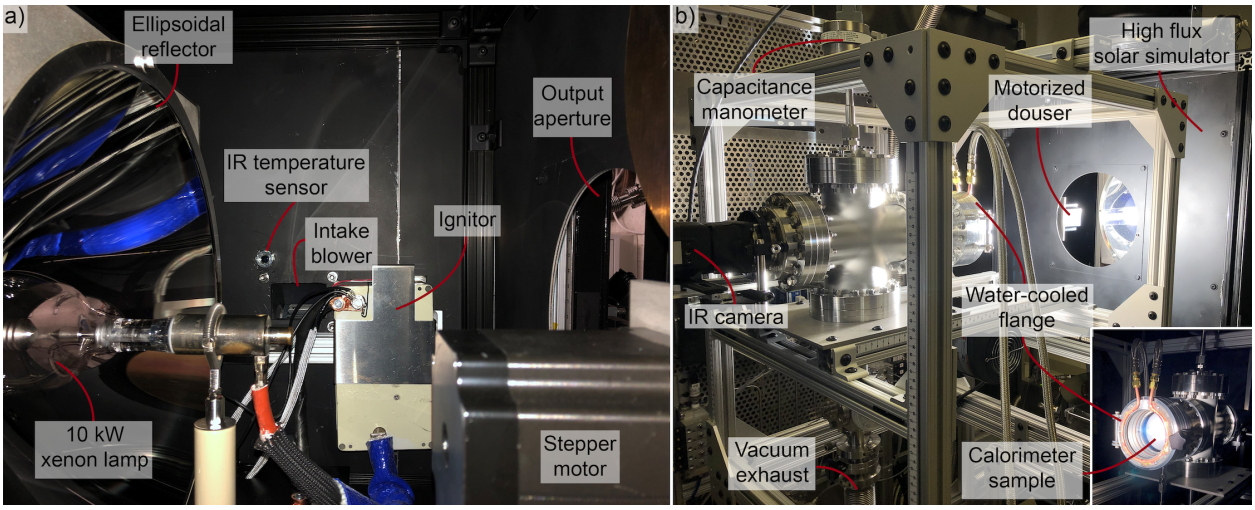

Figure 2.1: (a) Overview of the solar simulator and its main components. (b) Experimental setup used in characterizing the solar simulator, where the figure inset shows front view of vacuum chamber with target.

with a motorized douser to provide an additional degree of control over its output (e.g., cyclic or attenuated solar irradiation). An overview of the solar simulator and its main components in the horizontal orientation is shown in Fig. 2.1a; the HFSS can also be rotated to a beam-down configuration for future studies.

2.2.2 Radiometer and temperature measurements

The experimental setup, shown in Fig. 2.1b, consists of a stainless steel cylindrical vacuum chamber with an inner diameter of 9.7 cm (6" CF flange) and a 10.2 cm aperture with a fused quartz window. An additional water-cooled flange was added to maintain the window and vacuum chamber at relatively low temperatures. A titanium mount and thin graphite disk target for inverse characterization of the HFSS at different powers (supply currents) are placed into the vacuum chamber at the HFSS's focal plane (7 cm from chamber's front flange). A 0.8 mm thick isotropic graphite disk (Entegris/Poco Graphite, TM-grade) that

is 8.9 cm in diameter was used as the target for characterization and is hereafter referred to as the 'radiometer'. The vacuum chamber has a capacitance manometer port to monitor the chamber's vacuum pressure and a zinc selenide (ZnSe) viewport for monitoring the radiometer's back side temperature using IR thermography. A high-resolution science-grade longwave infrared camera (FLIR, A655sc) monitors and measures the temperature of the radiometer. The camera has a resolution of 640 x 480 pixels, 16-bit dynamic range, accuracy of $\pm 2\%$ over its full scale, spectral range of 7.5-14.0 µm, and can measure temperatures up to 2000 °C. During camera calibration to account for the ZnSe window's transmissivity (τ_{IR}), a flat transmissivity value of 0.72 from 7.5 to 10 µm was measured and validated across a reference temperature transducer to be appropriate for IR temperature monitoring.

2.2.3 Spectral characteristics

The spectral distribution output from a xenon short arc lamp has been measured in many prior studies, and it best simulates the air mass 1.5 solar standard spectrum [47, 76]. Here, the spectral distribution of the HFSS is also presented but with a focus on its variation in relation to output power (controlled by varying the supplied current from 100 to 200 A) since such measurements have not been reported elsewhere. This characterization was performed using an imaging spectrometer (Horiba, iHR 550) with a SynapsePlus CCD camera sensor and a blazed holographic grating of 1200 gr/mm to obtain measurements between 0.4-1 µm. The CCD camera is thermoelectrically cooled to -95 °C and has an active spectral range of 0.2-1.1 µm. The normalized spectral distribution output from the HFSS is shown in Fig. 2.2 at different supply currents, illustrating the variation of the spectral output under different operating conditions. As shown in Fig. 2.2, as the power output of the xenon short

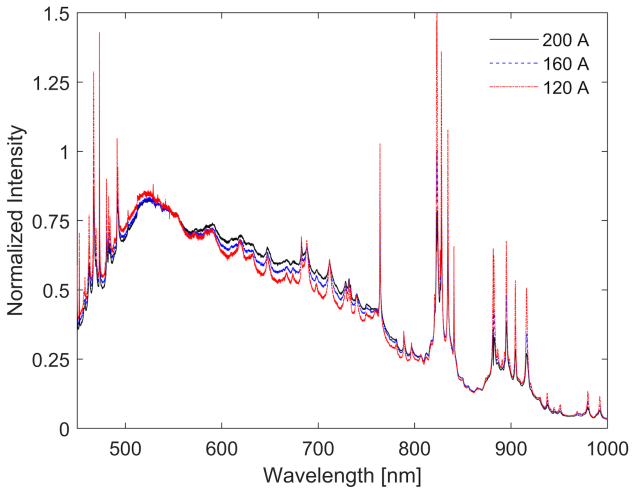

Figure 2.2: Spectral distribution output measured from the HFSS at different powers (supply currents) and normalized by area under the curves.

arc decreases from its maximum, the spectral output deviates in excess of 5% within the range of 450-800 nm, and all spectral line peaks become more pronounced; uncertainty from the imaging spectrometer contributes negligibly to measurement deviations, but temporal spectral variations in the lamp's output provide normalized spectra repetitiveness within 2%. Such spectral features are not expected to be significant in most applications but might be important to consider in testing spectrally sensitive photovoltaic or photocatalytic systems.

2.2.4 Direct heat flux mapping

The heat flux distribution from the HFSS was characterized directly using a HFG in the experimental setup shown in Fig. 2.3. Measurements were obtained at discrete points on the focal plane outside the vacuum chamber, without a quartz window, and at different operating lamp powers (supply currents). The water-cooled Gardon type gauge (Vatell Corporation, TG1000-0) is calibrated as-received and has an active gauge area with 1 mm diameter. The HFG is coated with colloidal graphite and can measure heat flux values up to approximately

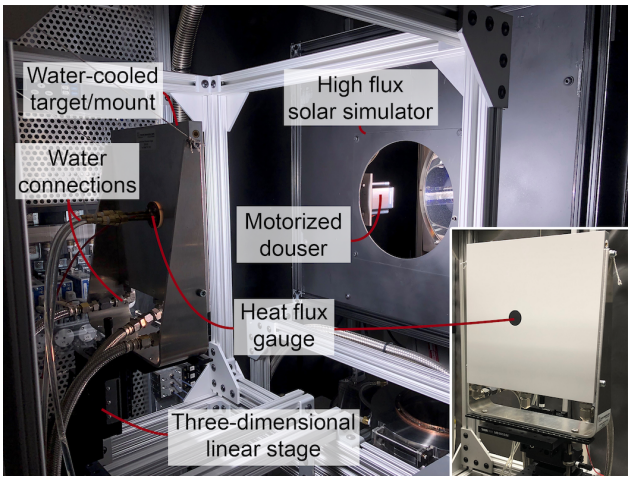

Figure 2.3: Experimental setup for characterizing the HFSS using a HFG for validation of the inverse heat flux mapping method.

5 MW/m^2 with a linear output voltage of 0-10 mV and an accuracy of $\pm 3\%$, as reported by the manufacturer. This type of HFG has been employed in several prior studies [53, 56, 57] and its measurements are used here to validate the present inverse characterization method. The HFG was mounted on and insulated from a water-cooled alumina-coated (white) aluminum target that supports the gauge and intercepts the concentrated radiation from the HFSS. The target's water-cooling and alumina coating to diffusely reflect most of the intercepted irradiation prevent heating of the target to ensure that minimal heat transfer occurs between the target and insulated housing of the HFG. The target is then mounted on a three-dimensional linear stage to obtain heat flux measurements at various discrete points.

We note that prior work has shown that the manufacturer's calibration for the type of HFG used in the present study may overestimate heat flux measurements by up to 30% due to a mismatch between the solar spectrum and that of the blackbody radiation used for calibration when the blackbody temperature is 1123 K (corresponding heat flux of 92 kW/m^2), as the spectral absorptivity of the HFG's colloidal graphite coating changes signif-

icantly with wavelength [55, 77]. In contrast, the present HFG has been factory-calibrated with incident heat flux values up to 2 MW/m^2 (corresponding maximum temperature of 2440 K), where the factory-calibrated sensor emissivity/absorptivity is reported as 0.82. By using spectral absorptance measurements of the colloidal graphite coating presented in prior work [77], the corresponding total absorptivity is estimated to be 0.66 for irradiation from a blackbody at 1123 K, 0.75 for a blackbody at 2440 K, and 0.84 for solar irradiation (blackbody at 5800 K). The preceding results indeed match well with prior conclusions indicating that a calibration temperature of 1123 K would overestimate solar irradiation (blackbody at 5800 K) by approximately 30% [55, 77]; from total absorptivity results indicated here, the overestimation is determined to be $(0.84/0.66 - 1) = 27\%$. In contrast, a calibration temperature of 2440 K leads to an overestimation of only $(0.84/0.75 - 1) = 12\%$. Based on the foregoing discussion and acknowledging possible variations in spectral emissivity among different surface conditions, the highest spectral absorptivity value of 0.88 at approximately 0.5 µm [77] instead of the estimated solar total absorptivity value of 0.84 is used to estimate an additional conservative uncertainty contribution towards measurements obtained by the HFG. Hence, the mismatch between the maximum spectral absorptivity and that of the sensor calibration induces an additional uncertainty in the heat flux measurements of $\pm 7\%$.

Prior work has shown that xenon arc lamps undergo an initial transient period before reaching a long-term temporal quasi-steady state. This transient period is 10-20 minutes for lamps of different sizes [52, 53, 74] and is characterized here in Fig. 2.4 for the initial 20 minutes. Instantaneous flux measurements were normalized by their average steady-state values 60 minutes after lamp ignition. As shown in Fig. 2.4, the HFSS requires approximately 15 minutes to reach 98% of its steady-state heat flux distribution. As such, all experimental

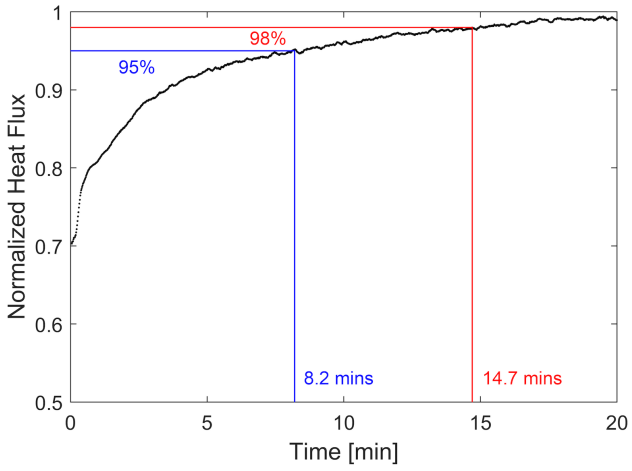

Figure 2.4: Transient nature of the heat flux output from the HFSS.

work presented in this chapter was conducted after this initial transient period. The HFG was then used to map the heat flux distribution at the focal plane in discrete radial increments of 1 mm along the main axes starting from the center and up to a total distance of 27 mm at different supplied currents to the lamp (100-200 A). For data acquisition and processing, the HFG was connected to a National Instrument PXI system (PXIe-1092) and its thermocouple module (PXIe-4353). Accounting for the manufacturer's calibration uncertainty of $\pm 3\%$, sensor absorptivity uncertainty of $\pm 7\%$, and variations in time and radially averaged measurements uncertainty of $\pm 2.5\%$, an overall uncertainty of approximately $\pm 8\%$ is estimated for the heat flux measurements. This overall uncertainty is consistent with recent work [53].

2.3 Heat Flux Methodology

The heat flux distribution from the HFSS is determined by solving an inverse problem that uses steady-state spatial temperature measurements from an IR camera. Because of symmetry in the heat flux output of a properly aligned HFSS and vacuum chamber, experimental

temperature measurements are radially averaged to provide 1D radial temperatures along the graphite radiometer; this averaging significantly reduces measurement noise. Then, parameters of a predefined heat flux function are estimated by implementing a minimization algorithm (Nelder-Mead) to a 2D numerical heat transfer model. The Nelder-Mead algorithm is a direct search method to solve unconstrained optimization problems without requiring a function gradient, where a simplex shape structure with $(n+1)$ vertices is used to minimize the objective function of n input dimensions [78]. The shape structure points are evaluated, and a selection rule is used to move these points relative to their outputs based on any of the following operations: reflection, expansion, contraction, and shrinkage [79]. Thus, the minimization algorithm is solved iteratively until convergence is achieved.

To assess the accuracy of the inverse technique in determining the heat flux inside the vacuum chamber, its results are compared to measurements obtained directly using the HFG outside the chamber and by utilizing a validated MCRT model, where both methods are completely independent from the inverse mapping method. The MCRT model is used to further verify measurements from the HFG and to draw conclusions on possible deviations between heat flux distributions inside and outside of the vacuum chamber. Importantly for validation of the inverse mapping technique, heat flux results obtained outside the vacuum chamber using the HFG were multiplied by a factor of 0.92 to compensate for the quartz window's solar transmissivity ($\tau_{\mathrm{qrt}} = 0.92 \pm 0.02$).

2.3.1 Monte Carlo ray tracing

Monte Carlo ray tracing (MCRT) is an accurate method for modeling radiative heat transfer and, more generally, optical systems [80, 81]. An experimentally validated in-house MCRT

model of a HFSS was previously developed and presented [58, 82]. Here, the 3D MCRT model is used to predict the heat flux distribution, with minor modifications reflecting differences in the HFSS configuration, to further verify the accuracy of HFG measurements. The MCRT model assumes the xenon arc lamp to be an isotropic emitting composite volume that consists of a hemisphere attached to a cylinder. Both the hemisphere and cylinder have diameters of 2 mm and emit power at a ratio of 0.23:0.77, the cylinder is 10 mm long, and the composite shape is positioned within the truncated reflector (reflectivity assumed to be 0.9) with the hemisphere's center coinciding with the reflector's theoretical focal point [82].

Although peak flux values obtained from the original model were consistent with experimentally measured heat flux values using the HFG, the general distribution was slightly changed due to differences in the HFSS configuration. To account for such differences, the electrical power conversion efficiency (η_{el}) and the surface specular error (θ_{sp}), which is a deviating zenith angle with a Gaussian distribution around zero, were treated as free parameters to allow for better fits to the experimental HFG measurements at the focal plane. These two parameters were chosen, as they do not change the inherent physics of the validated MCRT model, but rather provide fitting of parameters that could vary between different HFSSs; η_{el} depends on system connections and condition of the lamp, while θ_{sp} depends on manufacturing tolerances associated with the ellipsoidal reflector geometry and its surface condition. Upon fitting these parameters to the heat flux distribution obtained by the HFG at the focal plane, η_{el} and θ_{sp} changed from 50% and 5 mrad to 59% and 6.75 mrad.

2.3.2 Inverse method

Inverse problems are generally ill-posed and lack unique solutions, unlike forward well-posed problems [83]. They are usually subject to issues such as solution existence, uniqueness, and instability to small noises or perturbations [84] that become more severe with respect to the ratio between the number of solution unknowns and known measurements. Therefore, an effective approach in characterizing the HFSS is to adopt an inverse problem and reduce the number of solution unknowns by transforming the problem into a parameter estimation problem to yield a stable, well-conditioned problem. This approach is performed here by applying constraints on the heat flux distribution based on expected trends from the HFSS.

Expected trends from the HFSS

Due to the shape of the HFSS's ellipsoidal reflector, the heat flux distribution output at the focal plane strongly resembles a Gaussian or Lorentzian distribution [52, 85, 86]. The nature of the distribution being Lorentzian versus Gaussian depends on the optical alignment of the system, any optical distorters such as a quartz window, and potentially the lamp power. To encompass the nature of both profiles, the heat flux distribution (q''_{s}) is represented using a weighted summation of both profiles as:

$$q''_{\mathrm{s}}(r) = A_{\mathrm{s}} \left[\frac{(1-\alpha_{\mathrm{L}})}{\sigma_{\mathrm{G}}\sqrt{2\pi}} \exp\left(\frac{-r^2}{2\sigma_{\mathrm{G}}^2}\right) + \frac{\alpha_{\mathrm{L}}}{\pi}\left(\frac{\sigma_{\mathrm{L}}}{r^2+\sigma_{\mathrm{L}}^2}\right)\right] , \tag{2.1}$$

where α_{L} is the weighing parameter and ranges from 0 to 1, σ_{L} is the half width at half maximum of the Lorentzian distribution, σ_{G} is the standard deviation of the Gaussian distribution, A_{s} is the amplitude parameter adjusting both profiles, and r is the radial distance

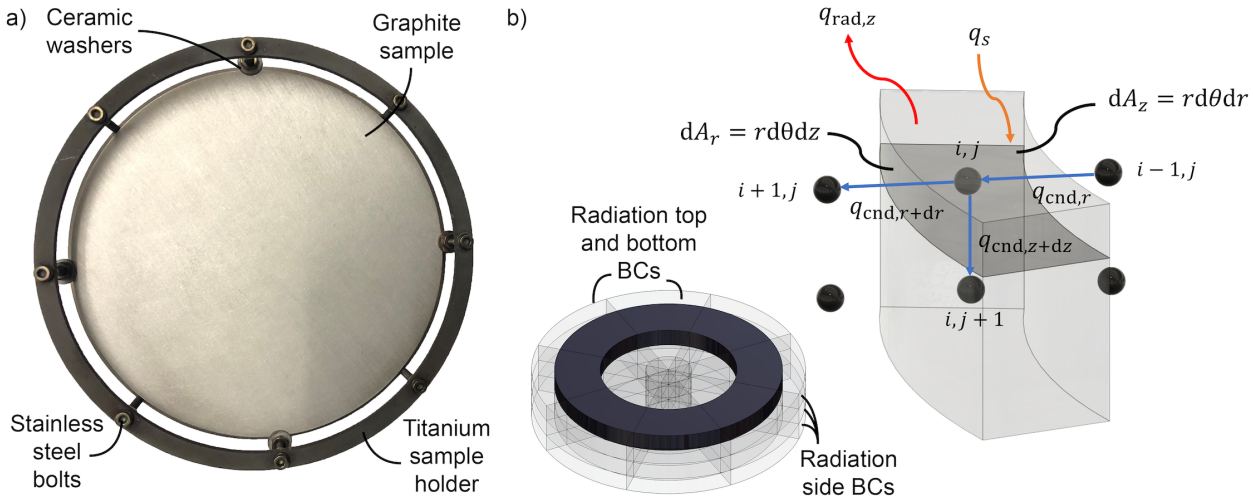

Figure 2.5: (a) Photograph of the radiometer developed and used in this study, and (b) schematic illustration of the control volume considered.

from the center. The assumed profile can be valid under different conditions, such as with a quartz window or away from the focal plane. Additionally, another trend incorporated in the inverse problem solution here is the linear relationship that exists between the heat flux distribution and HFSS current supply [52, 87].

Numerical modeling

A steady-state heat transfer model was developed to estimate the fitting parameters of the heat flux distribution (Eq. 2.1) by solving an inverse problem using the IR camera temperature measurements. Because the system and radiation source considered here are both symmetric in cylindrical coordinates, the model can be treated as 2D without loss of accuracy. A photograph of the radiometer and an illustration of the control volume considered later for the heat transfer model are shown in Fig. 2.5. Additionally, the outer edge of the graphite radiometer is assumed to be perfectly insulated from conduction heat

transfer as a result of using alumina washers with a low thermal conductivity and small contact area with the radiometer (see Fig. 2.5a). The radiometer is only tested under vacuum conditions, and hence convection heat transfer can be neglected. Therefore, the steady-state energy conservation governing equation reduces to:

$$\nabla \cdot (k\ \nabla T) = \frac{1}{r}\frac{\partial}{\partial r}\left(k\ r\ \frac{\partial T}{\partial r}\right) + \frac{\partial}{\partial z}\left(k\ \frac{\partial T}{\partial z}\right) = 0\ , \tag{2.2}$$

where T is temperature and k is a temperature-dependent thermal conductivity. The boundary condition at the center of the graphite radiometer is $\partial T/\partial r|_{r=0} = 0$ due to symmetry. The other boundary conditions encompass radiation thermal losses in addition to solar irradiation from the HFSS where applicable. For radiation thermal exchange, the surrounding surfaces are assumed to have a uniform temperature and emit like a blackbody in order to reduce the complexity of the numerical model without significantly affecting its results. Justification of the aforementioned assumptions is not discussed here for brevity, but is addressed through experimental measurements and a more detailed radiosity model in Fig. A.1 and its accompanying text. Based on the foregoing discussion, the boundary conditions at the radiometer's outer radial edge ($r = R$), back surface facing IR camera ($z = t$), and front surface facing the HFSS ($z = 0$) are:

$$-k(T)\ \frac{\partial T}{\partial r}\Big|_{r=R} \quad \text{and} \quad -k(T)\ \frac{\partial T}{\partial z}\Big|_{z=t} = \left[\varepsilon(T)\sigma T^4 - \alpha(T_{\text{sur}})\sigma T_{\text{sur}}^4\right]\ , \tag{2.3}$$

$$-k(T)\ \frac{\partial T}{\partial z}\Big|_{z=0} = \alpha_{\text{s}} q_{\text{s}}'' - \left[\varepsilon(T)\sigma T^4 - \alpha(T_{\text{sur}})\sigma T_{\text{sur}}^4\right]\ , \tag{2.4}$$

where t is the radiometer's thickness, ε is emissivity, and α is absorptivity. Due to the temperature dependence of thermal conductivity when evaluating the governing equation, the term $\partial k/\partial r$ is substituted as $(\partial k/\partial T)(\partial T/\partial r)$. A similar approach applies to the z component. Upon evaluating the governing equation for interior nodes and surface nodes based on the boundary conditions, the finite difference (central difference when applicable) approximation is used to solve the partial differential equations. Following the foregoing methodology, the discretized form of the governing equation for the inner front surface nodes (facing HFSS at $z = 0$ and $0 < r < R$, see Fig. 2.5b) is:

$$\begin{aligned} T_{i,j}\left(\frac{2k}{\Delta r^2}+\frac{2k}{\Delta z^2}\right) &= T_{i+1,j}\left(\frac{k}{\Delta r^2}+\frac{k}{2r_i\Delta r}\right)+T_{i-1,j}\left(\frac{k}{\Delta r^2}-\frac{k}{2r_i\Delta r}\right) \\ &+T_{i,j+1}\left(\frac{2k}{\Delta z^2}\right)+\frac{1}{4\Delta r^2}\left(\frac{\partial k}{\partial T}\right)\left(T_{i+1,j}-T_{i-1,j}\right)^2-T_{i,j}^4\left(\frac{2\varepsilon(T_{i,j})\sigma}{\Delta z}\right) \\ &+T_{sur}^4\left(\frac{2\varepsilon(T_{sur})\sigma}{\Delta z}\right)+\left(\frac{2\alpha_s}{\Delta z}\right)q_s''(r_i)\ . \end{aligned} \tag{2.5}$$

With a similar methodology to that of Eq. 2.5 above, eight additional discrete equations can be obtained for all remaining nodes.

Determination of thermal and optical properties

The proper evaluation of thermal (k) and optical (α, ε) properties for the steady heat transfer model used in the inverse problem is crucial for accurate heat flux characterization. Starting with the thermal conductivity and based on solid state theory, its total value can be determined via lattice and electronic contributions to thermal transport [88]. By assuming that these heat transfer modes are independent, the total thermal conductivity can be defined as: $k_{\text{tot}} = k_{\text{lat}} + k_{\text{el}}$ [89]. The electronic contribution to k_{tot} can be determined following the

Wiedemann-Franz law [90] as: $k_{\mathrm{el}} = N_L \sigma_{\mathrm{el}}(T) T = N_L T / \gamma_{\mathrm{el}}(T)$, where N_L is the Lorenz number, σ_{el} is the electrical conductivity, and γ_{el} is the electrical resistivity, which for isotropic graphite varies linearly with temperature above 1000 K [89, 91]. The graphite's electronic contribution to k_{tot} is reported to be less than 5% for temperatures up to 1000 K [89].

The lattice contribution to k_{tot} includes various scattering mechanisms, of which the significant ones are phonon-phonon and grain boundaries (phonon-electron and impurity scattering rates are many orders of magnitude smaller) [91]. Based on a grain/particle size of 10 µm for the graphite sample [92], scattering due to grain boundaries can be further ignored. Therefore, the dominant scattering in lattice thermal conductivity is the three-phonon scattering process, of which only Umklapp scattering directly impedes thermal transport [88] with a T^{-1} variation in thermal conductivity [91]. Here, the total thermal conductivity function is taken as $k_{\mathrm{tot}} = 1/(A + BT)$, where such a model describes graphite's thermal conductivity accurately from room temperature up to $\approx$ 2000 K [89]. By fitting the model for k_{tot} to the graphite manufacturer's thermal conductivity data to reduce measurement errors and uncertainty, the following parameters are obtained: $A = 5.69{\times}10^{-3}$ m K/W and $B = 9.62{\times}10^{-6}$ m/W.

For optical properties, an approximate three-level semi-gray model is constructed using literature data. The semi-gray model is based on the spectral ranges 0-2 µm, 2-7.5 µm, and >7.5 µm as these three ranges can be represented by constant values that remain within approximately $\pm\,3\%$ of reported spectral emissivity measurements. Normal spectral emissivity ($\varepsilon_{\lambda,\mathrm{n}}$) measurements of a mechanically polished isotropic graphite (similar to the one used in this study) were reported by Autio and Scala at wavelengths greater than 2 µm and at temperatures near 1450 K [93]. The reported values of $\varepsilon_{\lambda,\mathrm{n}}$ were observed to be temperature-

independent across a wide temperature range (as large as 500-1800 K), as also observed in other studies [94, 95], and averaged 0.60 $\pm$ 0.02 within the wavelength interval of 7.5-14 µm, which is the same spectral range as the IR camera used in this work. Hence, this value was used for the sample's emissivity (ε_{IR}) in IR camera temperature measurements, which agrees well with calibration measurements using a type K thermocouple taken at temperatures up to approximately 700 K. For the wavelength interval of 2-7.5 µm, normal spectral emissivity measurements [93] averaged around 0.72 $\pm$ 0.02, which was further incorporated into the semi-gray model developed here. In other studies [94, 96], an average value of approximately 0.78 $\pm$ 0.02 was reported for the normal spectral emissivity at wavelengths less than 2 µm, and this value has been adopted in the semi-gray model to represent the spectral range of 0-2 µm:

$$\varepsilon_{\mathrm{n}}(T) = (0.78)F_{0\to 2\mu\mathrm{m}}(T) + (0.72)F_{2\to 7.5\mu\mathrm{m}}(T) + (0.6)\left(1 - F_{0\to 7.5\mu\mathrm{m}}(T)\right) \ , \tag{2.6}$$

where $F_{\lambda_1\to\lambda_2}$ represents the fraction of total blackbody emission at temperature T in the wavelength interval between λ_1 and λ_2.

To determine the overall absorptivity of the graphite target (radiometer), the model presented in Eq. 2.6 is used for absorptivity based on Kirchhoff's law for opaque materials: $\varepsilon_{\lambda,\theta} = \alpha_{\lambda,\theta} = 1 - \varrho_{\lambda,\theta}$. The irradiance from the HFSS onto the sample is close to the normal direction and well represents the solar spectrum with equivalent blackbody radiation at 5800 K. Therefore, Eq. 2.6 is used to quantify α_{n}(5800 K), which is equivalent to α_{s}, and produces a value of 0.776 $\pm$ 0.02. A blackbody radiation spectrum at 5800 K is used to determine α_{s}

rather than that measured in-house, as measurements presented in Fig. 2.2 only encompass approximately 70% of the solar simulator's total output power.

As for graphite's emissivity, its normal emissivity can be correlated to hemispherical emissivity either through experimental measurements [95, 97] or by using electromagnetic wave theory [98]. Prior studies have indicated that optical properties of polished graphite behave similarly to metals [94]. As such, when electromagnetic waves impinge on the surface of a conducting medium with a complex index of refraction ($m = n - ik$) at an angle from normal, Fresnel's relations can predict the parallel and perpendicular reflectivity for polarized light [98]. Under the assumption of unpolarized light, $\varrho = 0.5(\varrho_{\parallel} + \varrho_{\perp})$ in the infrared region and by utilizing Kirchhoff's law, the ratios of hemispherical to normal spectral emissivity ($\varepsilon_{\lambda}/\varepsilon_{\lambda,\mathrm{n}}$) are derived [98] and available in terms of n and k/n. The complex indices of refraction for graphite have been measured in prior work [99, 100], where n and k/n vary from 4.0 to 8.0 and 0.75 to 1.0 for the wavelength region from 2 to 10 µm, respectively. Therefore, the variation in complex indices of refraction within the infrared region leads to $\varepsilon_{\lambda}/\varepsilon_{\lambda,\mathrm{n}}$ varying from 1.05 to 1.13. Additionally, experimental measurements have been reported for graphite's normal and hemispherical emissivity at a wavelength shorter than 2 µm [95], more specifically at 0.65 µm, where $\varepsilon_{\lambda}/\varepsilon_{\lambda,\mathrm{n}}$ varies between 1.06 and 1.10 within the temperature range from 1273 to 2173 K. Based on the foregoing discussion and results, the ratio of hemispherical to normal emissivity was estimated to be $\varepsilon/\varepsilon_{\mathrm{n}} = 1.1 \pm 0.05$. Therefore, the hemispherical emissivity of the graphite sample for the heat transfer model is obtained at different temperatures using: $\varepsilon(T) = (\varepsilon/\varepsilon_{\mathrm{n}})\varepsilon_{\mathrm{n}}(T) = 1.1\varepsilon_{\mathrm{n}}(T)$.

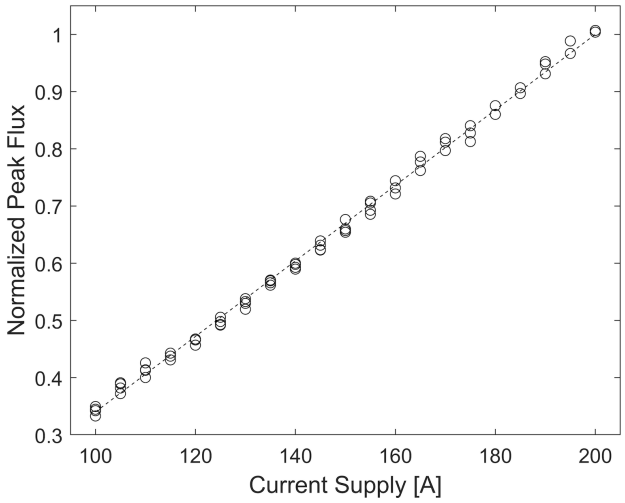

Figure 2.6: Variation of the peak heat flux values with HFSS current supply as measured by the HFG.

2.4 Results and discussion

2.4.1 Heat Flux Gauge

The heat flux distribution was directly characterized outside the vacuum chamber using the HFG at the focal plane and various powers (supply currents), as well as at different focal planes. Results from the HFG for flux distribution are presented in the following sections; here the variation of peak flux with respect to current supply is presented. Measurements were obtained from different experimental runs, and the current supply was both increased and decreased to account for any hysteresis effects (if present). Based on the results in Fig. 2.6, a linear relationship exists for the variation of peak flux and total power with current in the range of 100-200 A, giving $CF = 0.0066I - 0.32$, where CF is a correlation factor normalized by the peak value of 4.54 MW/m^2 at maximum current (200 A). This factor is used in determining the supply current dependence of HFSS output.

2.4.2 Monte Carlo ray tracing

The MCRT model with its two free parameters were fitted to heat flux distribution results obtained using the HFG at the focal plane and at different supply currents, where CF was used to correlate the model results at different supply currents. Results from the MCRT model for the heat flux distribution outside the vacuum chamber and at a supply current of 160 A are shown in Fig. 2.7a, where good agreement exists between model results and HFG measurements. The MCRT heat flux distribution at the focal plane falls within the uncertainty of all HFG measurements by additionally accounting for the uncertainty in radial position of ± 0.2 mm (not shown). Because the validated MCRT model only used system specific variables (η_{el} and θ_{sp}) in fitting the experimental results as discussed earlier, the accuracy of HFG measurements can be further assessed from results of the peak flux variation with respect to distance from the focal plane as shown in Fig. 2.7b. Both results from the HFG and MCRT follow the same declining trend, and results predicted by the MCRT simulation fall within the uncertainty of the HFG, which is estimated to be approximately $\pm 8\%$.

2.4.3 Inverse method

The inverse heat transfer problem was solved using the python scipy.optimize package that implements the Nelder-Mead algorithm to minimize residual error between the IR camera temperature measurements and those of the sample's modeled back surface. In this minimization problem, the fitting parameters that determine the heat flux distribution in the vacuum chamber are α_{L}, σ_{G}, σ_{L}, and A_{s}, as introduced in Eq. 2.1. A mesh independence study was conducted to evaluate the optimum mesh size and to verify the accuracy of the

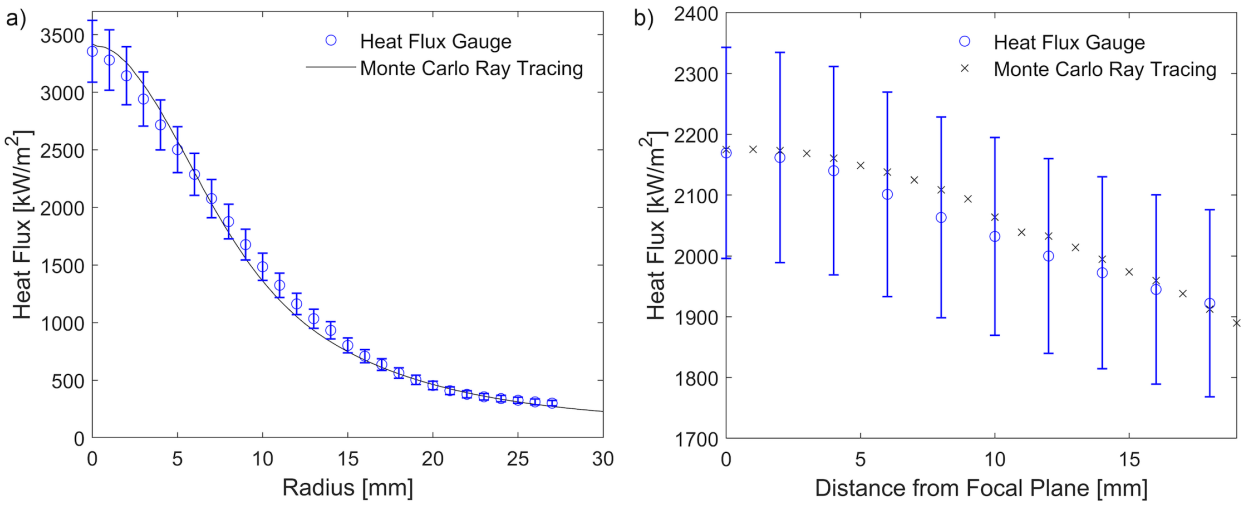

Figure 2.7: Validation of the in-house MCRT model with respect to measurements from the HFG outside the vacuum chamber showing (a) heat flux distribution at the focal plane and 160 A HFSS supply current, and (b) peak heat flux values at different focal distances and at 120 A HFSS supply current.

model, as presented in Fig. A.2. The time-averaged temperature contour of the sample's back surface as measured by the IR camera with a high resolution of 0.26 mm/pixel is shown in Fig. 2.8a. The contour distinctly exhibits the expected radially symmetric temperature distribution consistent with the heat flux input, and further supports the implementation of radial temperature averaging to reduce measurement noise and inverse model computational load. Additionally, Fig. 2.8b shows the time and radially averaged temperature profile of the graphite radiometer as measured by the IR camera compared to its front (facing HFSS) and back (facing IR camera) surfaces as predicted by the heat transfer model. The IR camera temperature radial variation in Fig. 2.8b remains within 2.5% over the entire surface of the radiometer. Three observations are paramount: (1) radially averaged IR camera temperature measurements represent a smooth distribution consistent with the heat flux profile assumption implemented here; (2) the experimental temperature profile's gradient nearly de-

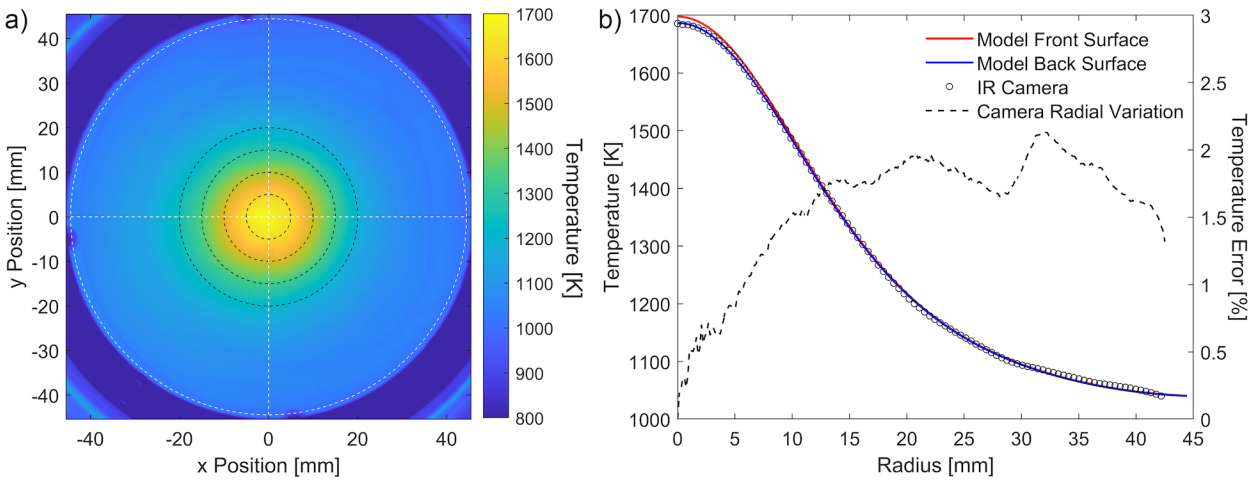

Figure 2.8: (a) Time-averaged temperature profile of the graphite sample back surface obtained using the IR camera for a test at HFSS supply current of 100 A (centered black rings with r = 5, 10, 15, and 20 mm illustrate distribution and angular uniformity). (b) IR camera radially averaged temperature distribution and predictions from the inverse heat transfer model for front and back sample surfaces.

cays to zero at the outer radius of the radiometer, consistent with the radial outer boundary condition of no conduction heat transfer; and (3) a very small difference is observed between the front and back surfaces of the graphite radiometer as a result of its thickness. The latter observation suggests that the heat transfer model can be potentially reduced further from 2D to 1D and still provide acceptable heat flux characterization. However, because computational time was not of concern here, the 2D model was employed.

The solution of the heat flux distribution inside the vacuum chamber was obtained for HFSS supply currents in the range of 100-140 A with an increment of 10 A, and five experimental tests were performed at each current value. This approach allows evaluation of parameters such as the measurement uncertainty of the inverse heat flux characterization technique in addition to a unified heat flux distribution profile that varies linearly with the

HFSS supply current, per expectation [52]. Fig. 2.9a shows the inverse heat transfer model results at a supply current of 100 A, where the individual heat flux radial profiles determined from the five repeated tests are indicated and can be readily converted into symmetric heat flux contour maps. The five profile sets were used to construct a mean heat flux distribution with an uncertainty interval (based on the standard deviation) shown in Fig. 2.9a that was then compared to the measurements obtained using the HFG outside of the vacuum chamber. Because HFG measurements were not obtained with the window in place, they are corrected in Fig. 2.9 to compensate for the quartz window's solar transmissivity ($\tau_{\mathrm{qrt}} = 0.92$).

As shown in Fig. 2.9a, the inverse heat transfer model results and uncertainties fall within the uncertainty range of HFG measurements but with a slightly broader heat flux distribution. To determine the effect of inverse model parameter uncertainties on the obtained heat flux profile, a sensitivity analysis was performed as presented in Fig. A.3 and discussed in the accompanying text. The sensitivity analysis demonstrates that the inverse model results are most sensitive to the radiometer's optical properties, particularly those pertaining to the IR camera measurements, and that the radiometer's thermal conductivity significantly affects the determined peak heat flux with no changes to the determined total power. Although the uncertainty of inverse model parameters can contribute to the slight discrepancy between the two general profiles in Fig. 2.9a, such deviation is also potentially due to refraction from the quartz window and/or annular beam truncation by the vacuum chamber. However, the effects of additional components on the heat flux distribution at the radiometer's position were determined to be minimal based on results from the MCRT model when applying Snell's law and room temperature optical properties for the quartz window (apart from a linear attenuation due to τ_{qrt}).

The results in Fig. 2.9a suggest that thermal effects due to temperature-dependent optical properties of the quartz window as a result of a non-uniform temperature profile could potentially contribute to such a difference, similar to the work presented by Gurwich and Spector [101]. Such a detailed investigation is outside the scope of this study, but the temperature gradient on the quartz window was recorded and is presented in Fig. A.4 with accompanying text that discusses the relatively large temperature gradient observed. Additionally, the discrepancy between HFG measurements and the inverse technique results can be due to misalignment of both experimental setups, where a misalignment as small as 4 mm can lead to reduction in the peak heat flux values as high as 6% with insignificant reduction in the total power [58]. Comparing total powers at 100 A from the inverse model's average flux profile and Lorentzian fit from the HFG measurements, the total powers on the radiometer (integrals of heat flux over a circular area with a diameter of 8.9 cm) were estimated to be 1.31 ± 0.07 kW and 1.23 ± 0.1 kW, respectively. Therefore, based on the foregoing discussion in addition to good agreement in heat flux and total power values, the presented inverse technique for heat flux characterization and monitoring can be considered validated.

A similar procedure was performed at different HFSS supply currents, where the entire heat flux profile sets were normalized to obtain the composite Lorentzian/Gaussian distribution parameters, which are independent of current supply, and the magnitude parameter A_s, which is assumed to depend linearly on current. The current-dependent values of the heat flux distribution presented in Eq. 2.1 are $A_\mathrm{s} = 0.740I - 20.5$ kW/m, $\sigma_\mathrm{L} = 0.0492$ m, $\sigma_\mathrm{G} = 0.00829$ m, and $\alpha_\mathrm{L} = 0.519$. These final averaged parameters were then used to plot

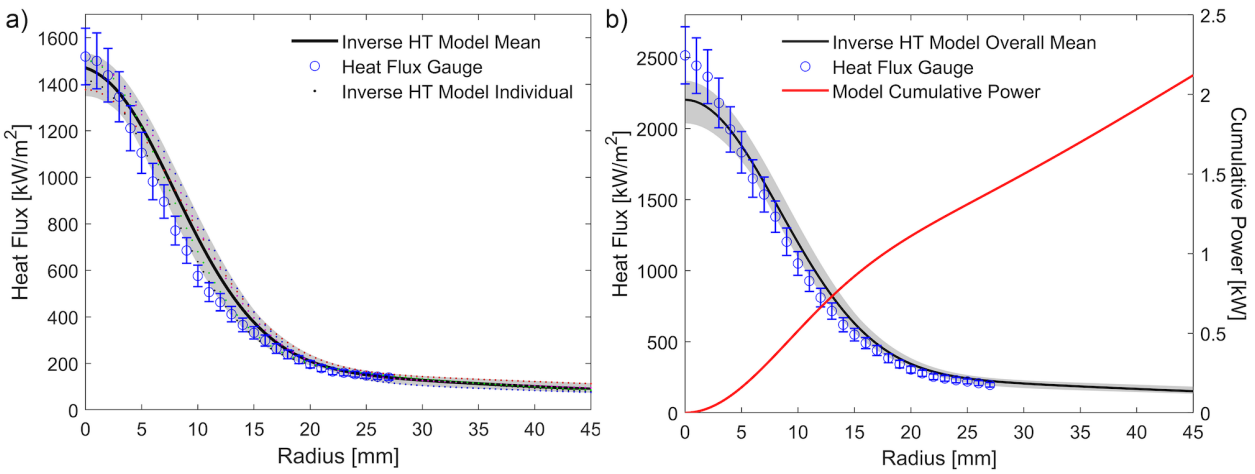

Figure 2.9: (a) Results of the inverse heat transfer (HT) model at HFSS supply current of 100 A showing heat flux distribution inside the vacuum chamber of five repeated experimental runs and their average compared to corrected measurements from HFG. (b) Final averaged results of the inverse heat transfer (HT) model at HFSS supply current of 140 A showing the heat flux distribution inside the vacuum chamber compared to corrected measurements from HFG. Gray shaded regions represent the uncertainty bounds of the inverse model heat flux results.

the final inverse heat transfer model results compared to those obtained using the HFG and corrected for a HFSS supply current of 140 A as shown in Fig. 2.9b.

Testing was not continued beyond HFSS supply currents of 140 A because the radiometer began to deteriorate at its center, which produced changes in graphite's thermal and optical properties. Therefore, we conclude that the inverse radiometer presented here is limited to peak solar irradiation up to approximately 2400 kW/m^2. Despite this limitation, the current-dependent relationship presented earlier can be used to extrapolate to higher HFSS supply currents and thus HFSS irradiation. Using the foregoing parameters of the heat flux distribution, the total powers obtained from the inverse model at supply currents of 160, 180,

and 200 A were estimated to be 2.50 ± 0.13 kW, 2.88 ± 0.14 kW, and 3.26 ± 0.16 kW. These compare well to 2.43 ± 0.19 kW, 2.86 ± 0.23 kW, and 3.29 ± 0.26 kW from the corrected HFG measurements. Therefore, despite some deviation of peak heat flux at higher HFSS power as a result of the different heat flux profiles, the cumulative power results are consistent. This outcome further validates the inverse model results and its extrapolation.

2.5 Conclusions

In this chapter, a custom-designed and built HFSS with a peak heat flux that can be controlled within the range of 1.5-4.5 MW/m^2 is introduced and thoroughly characterized. First, its transient response to reaching a steady-state operation was determined, with the conclusion that the HFSS requires 15 min to stabilize prior to conducting experiments. Additionally, the spectral distribution of its output with respect to current supply was measured. The heat flux distribution output from the HFSS was then characterized using a heat flux gauge to determine the gross solar irradiance output and to validate the presented inverse characterization technique. The latter provides a simpler, inexpensive, and accurate characterization method for determining the heat flux output using IR temperature measurements of a graphite sample (radiometer) in a vacuum chamber. Additionally, the present inverse technique provides a much faster approach to monitoring the HFSS's performance over time, instead of using a separate, dedicated system for characterization; the radiometer can be placed directly into a solar reactor to determine changes in the heat flux distribution [46]. However, this inverse technique was determined to be limited to solar irradiation up to 2400 kW/m^2, and higher peak fluxes were determined by extrapolating the parameters. For a HFSS employing multiple lamps that provide a higher combined solar irradiation, lamp

outputs can be individually characterized to provide the effective combined irradiation by superposition. Although peak flux values from the inverse technique at higher HFSS supply currents ($\gtrsim$ 140 A) start to deviate from those obtained using the HFG due to quartz window thermal effects, the total powers obtained using both methods were consistent. Finally, a MCRT model was developed and further tuned to represent the irradiation from the HFSS to further verify heat flux measurements, and to provide a powerful tool in modeling radiation heat transfer in future work, such as studying the quartz window thermal effects.

Chapter 3: Solar-thermal cold-wall chemical vapor deposition reactor design and characterization for graphene synthesis

Manufacturing processes are often highly energy-intensive, even when the energy is primarily used for direct heating processes. The required energy tends to derive from local utilities, which currently employ a blend of sources ranging from fossil fuels to renewable wind and solar photovoltaics, among others, when the end manufacturing need is thermal energy. Direct solar-thermal capture provides a compelling alternative that utilizes renewable energy to reduce greenhouse gas emissions from industrial processes, but one that has rarely been employed to date. In this chapter, a 10 kW_e custom-built high flux solar simulator (HFSS) that closely approximates the solar spectrum produces a heat flux distribution with an adjustable peak between 1.5 and 4.5 MW/m^2. The HFSS system is coupled to a cold-wall chemical vapor deposition (CVD) system that is equipped to automate graphene synthesis while providing safe operation, precise control, and real-time monitoring of process parameters. A numerical heat transfer model of a thin copper substrate is derived and validated to compute the substrate's temperature profile prior to the synthesis process. Peak substrate temperature is correlated to the HFSS supply current and vacuum pressure, as it serves as a critical design parameter during graphene synthesis. We report the synthesis of high-quality graphene films on copper substrates with an average Raman peak intensity ratio I_D/I_G of

This chapter created the paper by Abdalla Alghfeli, Mostafa Abuseada, and Timothy S. Fisher, "Solar-thermal cold-wall chemical vapor deposition reactor design and characterization for graphene synthesis", Journal of Vacuum Science & Technology B 40, 064205 (2022). DOI: 10.1116/6.0002091

0.17. Backscattered electron microscopy reveals a characteristic grain size of 120 μm, with an area ratio of 16 when compared to that of low-quality graphene on copper. The reported solar-thermal CVD system demonstrates the ability to produce a high-value product, namely graphene on copper, directly from a renewable energy resource with process control and automation that enables synthesis under a variety of conditions.

3.1 Introduction

Solar thermal energy is a clean and abundant energy resource, yet it has rarely been used to power thermal manufacturing processes. Improving the harvesting of such a renewable energy source with purpose-designed solar reactors will lead to numerous advances in material synthesis while reducing CO_2 emissions. This chapter represents a custom solar-thermal cold-wall CVD system and a related numerical thermal model that predicts substrate temperature at various power and vacuum conditions to allow precise control of graphene growth parameters.

In comparison to solar manufacturing, solar-driven thermochemical processing has attracted more attention due to its potential in providing clean fuels as alternatives to fossil fuels [46]. Concentrating technologies in capturing solar energy have been investigated for thermal-power applications and thermochemical reactions. Several studies have focused on enhancing the performance of solar reactors by analyzing flow regimes and improving solar absorption efficiencies for H_2 production from CH_4 decomposition [102, 103]. These studies have also analyzed the design of receiver cavities in H_2 and syngas production from H_2O and CO_2 splitting, respectively, by using metal oxides such as zinc oxide [102, 103] and non-stoichiometric cerium oxide [104]. Additionally, others have studied the adverse effect

of window deposition and reactor clogging on the performance of solar reactors by employing fluid flow analysis [105].

To study, characterize, and optimize solar energy technologies in a lab environment, solar simulators have been designed and fabricated, as reported in several prior studies. Custom-built solar simulators with single [38] or multiple [106] xenon arc lamps have been characterized by direct [38] and indirect [106, 107] heat flux mapping using a heat flux gauge, Lambertian target, and gray-scale camera. Furthermore, numerical heat flux characterization of a 10 kW_e xenon arc lamp in a truncated ellipsoidal reflector has been accomplished by solving an inverse problem from temperature measurements [38] and inverse Monte Carlo ray tracing [108].

Synthesis of two-dimensional materials and thin films such as graphene has attracted attention due to extraordinary properties such as high thermal and electrical conductivity [1, 2] and applicability to the semiconductor industry . The production of graphene has been achieved by many techniques such as liquid-phase [14] and shear-mixing [15] exfoliation of graphite. Graphene growth by chemical vapor deposition (CVD), yet another production approach, offers the ability to synthesize high-quality graphene layers and to accommodate roll-to-roll production [17, 18]. Different CVD mechanisms using localized heating from either plasma or thermal sources as well as the effects of factors such as temperature, flow conditions, and surface heat flux on graphene quality can be applied to solar-thermal graphene synthesis, which has not been previously reported.

Studies have been carried out using methane as the sole source to provide hydrogen [23] and the effect of decreasing plasma impingement by introducing a surface wave plasma [18], where both proved feasible in synthesizing high-quality graphene by plasma CVD. Single-

layer graphene on Cu foil was synthesized [18, 23] and showed uniform sheet resistance and optical transmittance applicable to transparent conductive electrodes [18]. Plasma synthesis of graphene at relatively low temperatures (300-600℃) was demonstrated on Cu foils [18, 109] as well as free-standing graphene layers on any substrate that can withstand 700℃ [24]. Additionally, fabrication of carbon nanotube bridges between metal tip electrodes [110] and surround-gate geometries around vertical single-walled carbon nanotubes [111] for field-effect transistors have been successfully achieved by plasma CVD. In manufacturing supercapacitors, plasma CVD has proven to be an effective method in synthesizing polygonal carbon nanofibers [9] and bioinspired micro-conduit electrode materials [8] with high areal capacitance, rate capability, and cyclic stability.

On the other hand, the effects of using oxidized foils, annealing in inert atmospheres, and enclosing the foil to decrease the impingement heat flux have been studied using cold-wall CVD with direct electric heating. These studies have also shown accelerated graphene growth with reduced nucleation density on Cu foil [33], and the ability to produce high-quality graphene layers on Cu [32, 33] and Ni [35, 36, 112] foils suitable for electronic and photonic applications. Moreover, utilizing carbon isotopes from either ^{12}C or ^{13}C methane sources was found to have an insignificant effect on electronic transport properties [35]. Synthesizing graphitic films on Ni foils by direct growth has also been studied by cold-wall CVD and found to produce high-quality films in a short growth time under low H_2 flow [36].

In the present work, we consider graphene growth by CVD with a simulated solar heat source to demonstrate the practicality of using a renewable energy resource to drive such manufacturing processes. Different CVD techniques adopted in prior studies [18, 23, 33, 35] have been investigated, where reported effects of temperatures [17, 25], flow conditions [23,

33], heat flux impingement [18], and carbon feedstock source [35] on graphene quality were considered throughout system design. The solar-thermal CVD encompasses a 10 kW_e xenon arc lamp capable of producing a controllable heat flux peak in the 1.5-4.5 MW/m^2 range and a cold-wall reactor equipped with gas supply and vacuum controls. Additionally, precise control of the substrate temperature through a related heat transfer model [39] is necessary to facilitate graphene synthesis. Graphene growth by solar heating shows high potential in providing high-quality films suitable for photonic and electronic applications.

3.2 Experimental setup

To achieve the objectives of this work, a custom-designed high flux solar simulator (HFSS) was built, and its incident flux distribution has been characterized [38] in the previous chapter. The HFSS was integrated with a custom CVD system that includes a cold-wall chamber in addition to computer controlled gas supply and vacuum systems. Fig. 3.1 provides an overview of the solar-thermal CVD and its main subsystems that are described below.

3.2.1 Solar simulator

The solar simulator consists of a 10 kW_e short xenon arc lamp (Superior Quartz, SQP-SX100003) that mimics the spectrum of the sun placed at the focal point of a truncated ellipsoidal reflector (Optiforms, E1023F). The reflector collects source radiation emitted at its first focal point to concentrate rays to produce a Gaussian-Lorentzian-like heat flux distribution around its second focal point with a focal length of 102 cm. Through the use of a controllable (30-58 V) DC power supply with 100-200 A variable current and a shutter, incident heat flux can be controlled and varied precisely. The heat flux distribution output from the solar simulator to the target substrate was characterized [38] in chapter 2 by solving

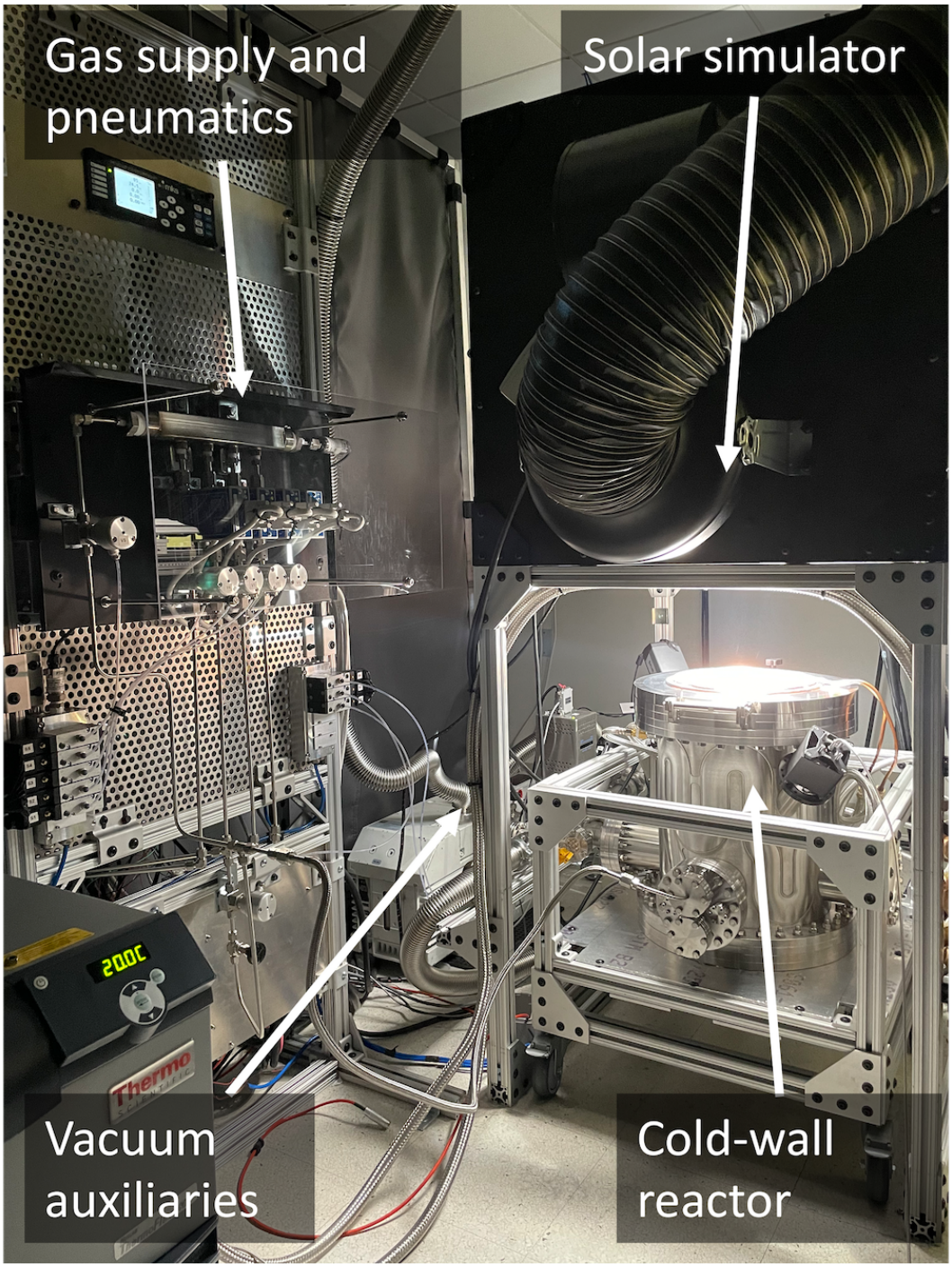

Figure 3.1: Overview of the solar-thermal CVD system that encompasses the following subsystems: solar simulator, gas supply and pneumatics, vacuum auxiliaries, and cold-wall reactor with cooling systems.

an inverse numerical heat transfer model using infrared (IR) temperature measurements on the back surface of a graphite sample placed at the solar simulator's focal plane. The heat flux distribution was fitted to a Gaussian-Lorentzian function with radial and current dependence as:

$$q''(r,I) = A(I)\left[\frac{(1-\alpha)}{\sigma_g\sqrt{2\pi}}e^{\left[-r^2/2\sigma_g^2\right]} + \frac{\alpha}{\pi}\left[\frac{\sigma_l}{r^2+\sigma_l^2}\right]\right] \tag{3.1}$$

where the heat flux q is in kW/m^2 and the fitted coefficients follow: $A(I)$ = (0.740 $\times I$ - 20.5) kW/m, σ_l = 0.0492 m, σ_g = 0.00829 m, and α = 0.519.

This heat flux correlation was validated in the solar simulator current range from 100 to 140 A and found to vary linearly with current. At 106 A HFSS current, the peak heat flux is q'' = 1540 kW/m^2, and total cumulative incident power on a 3.5 inch disk is Q = 1.48 kW.

3.2.2 Cold-wall chemical vapor deposition reactor

The solar-thermal CVD system encompasses a cold-wall reactor in which the sample is heated directly using the HFSS, and the reactor wall is cooled by chilled water. In this section, the integration of solar simulator with the CVD system is explained, as well as all instrumentation and controls. Fig. 3.2 illustrates the piping and instrumentation diagram that includes the following subsystems: solar simulator, gas supply with pneumatic, vacuum, and cold-wall reactor with its cooling system.

The gas supply system measures and controls flow rates of reactants introduced to the reactor and consists of four mass flow controllers (MKS, GM50A) calibrated for N_2, CH_4, H_2 and O_2 gases with the following flow rates 100, 100, 1000, and 10 sccm. Pneumatic solenoid valves are installed at various locations throughout the system to control flow inputs and output shutoff isolation valves and to provide safety interlocks in case of system failure.

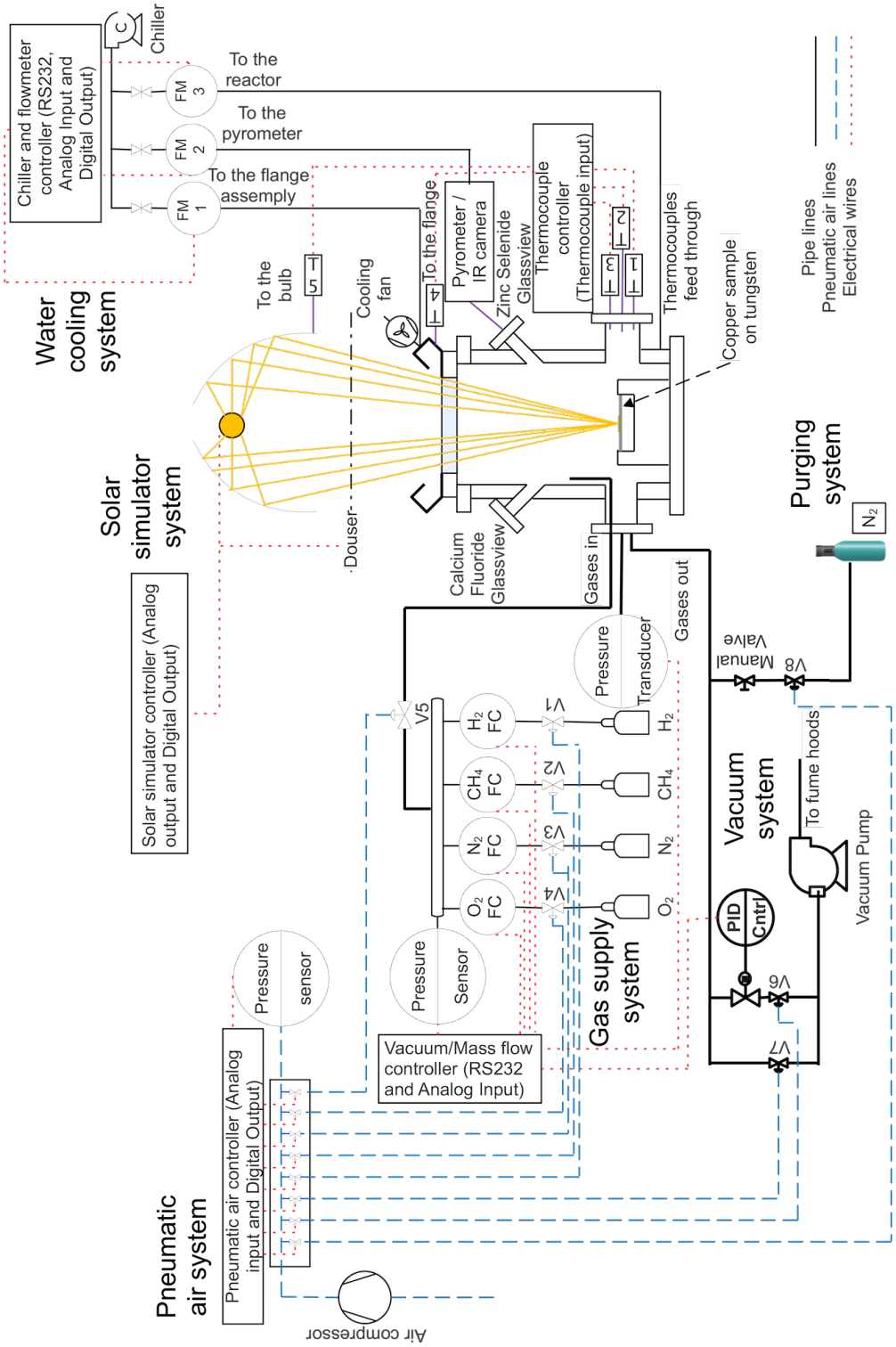

Figure 3.2: Piping and instrumentation diagram for the solar-thermal CVD system with analog, digital and RS232 communication signals for system control and monitoring.

The vacuum system maintains and controls pressure inside the reactor during the synthesis processes and is equipped with a rotary vane vacuum pump (Oerlikon-Leybold, D65BCS) and a control throttle valve (MKS, T3BI) to adjust the flow in the vacuum line. A capacitance manometer (MKS, 624F) is used to monitor process pressure with a resolution of $\pm 1\%$ up to 1000 torr and to provide a feedback signal to the PID controller that actuates the throttle valve.

The cooling system is essential to maintain equipment within safe operational ranges. It is equipped with a chiller (THERMOFLEX, TF14) with a cooling capacity of 1.4 kW to provide cooling to three subsystems, each equipped with a turbine meter for flow monitoring. A 25.4 cm (10 in.) quartz glass viewport (Technical Glass Products, Inc.) with $\tau = 0.92$ in the visible to near-IR range provides an entry for the solar simulator rays and absorbs some of the source light. Thus, chilled water flowing through a custom-fabricated copper flange placed near its sealing o-ring as well as air cooling by a blower are necessary to maintain the integrity of its vacuum seal. In addition, a custom-designed 304 stainless steel cylindrical reactor (Kert Lesker) with inner diameter and height of 30.5 and 40.6 cm (CF 16.5 inch flange) has embedded water channels in its outer wall. The pyrometer used to monitor the temperature of the copper requires a protective water cooling jacket to ensure a low operational temperature for accurate measurements.

To automate the graphene synthesis process and to ensure safe operation, a National Instrument PXI system with a controller (NI, PXIe-8821) and chassis (NI, PXIe-1092) are used. The system is equipped with modules including analog input/output, thermocouple input, digital I/O and RS232/RS485 serial communication to control and monitor the process, and safety interlocks in the LabView RT 2019 code. Such automation allows precise

control and monitoring of substrate temperature (by controlling the HFSS current), gas ratio (CH_4:H_2), vacuum pressure and residence time, which are critical parameters in graphene synthesis.

3.2.3 Sample fixture and system alignment

The sample stage is fabricated from corrosion-resistant 316 stainless steel and titanium materials. An annular 316 stainless steel disk is installed at the focal plane and holds a tungsten disk (substrate support) with alumina washers by clamping at four locations. The ceramic washers provide both mechanical support and thermal insulation with small contact area to the tungsten disk. The stage is also designed to support the sample at different heights as shown in Fig. 3.3, allowing changes in location out of the reflector's focal plane to produce a more uniform (less concentrated) heat flux distribution if needed. Once the sample fixture is inserted into the reactor, the system is aligned by acquiring an IR camera temperature profile on a 5 cm graphite disk while ensuring that its peak temperature is located at the center as shown in Fig. 3.3.

3.3 Analytical instrumentation

Analytical instruments are essential in CVD synthesis to measure process parameters during growth and to assess the quality and features of the growth product. During growth, monitoring substrate temperature provides useful information to optimize the process. Raman spectra of the synthesized graphene helps in assessing graphene quality by calculating the peak intensity ratio of defects in the lattice to in-plane C-C lattice vibrations. Backscattered electron microscopy assists in evaluating the uniformity and characteristic grain size of the products.

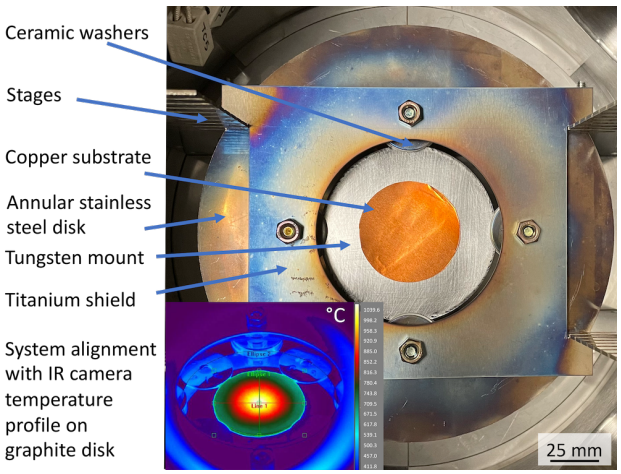

Figure 3.3: Sample stage with ceramic washers to minimize heat conduction loss from tungsten mount. Inset figure for system alignment carried out using IR temperature measurements (45° view) to ensure that the peak temperature is located at the center of the graphite disk.

3.3.1 Temperature sensors

Infrared sensors above wavelengths of 4.5 μm are most suitable to acquire temperature measurements based on emitted radiative energy that originates from the sample with negligible interference from the solar simulator reflected light. The glass envelope of the xenon arc lamp and the glass viewport of the reactor are made from fused quartz which is not transmissive to wavelengths larger than 4.5 μm.

Thus, a single wavelength 5μm pyrometer (Williamson, SP-GL-20C) calibrated in the range between 250-1375℃ is used to measure the peak temperature at the center of the copper substrate. It acquires temperature measurements through a zinc selenide viewport placed at 45 degrees with $\tau = 0.72$ in the pyrometer's spectral operating range. The melting point of copper (1085℃) was used to calibrate the 45 degree directional emissivity for accurate temperature measurements. An effective emissivity value of 0.031 was used for the annealed

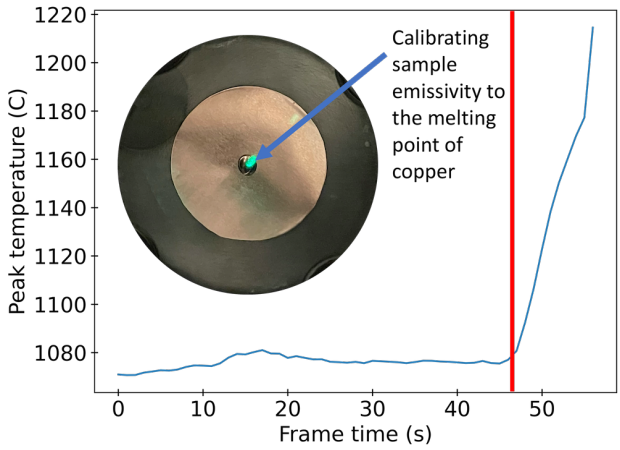

Figure 3.4: Pyrometer calibration for sample emissivity of annealed copper by the abrupt change of temperature at the onset of melting, where the green dot at the center denotes the location where the pyrometer measures temperature

copper substrate based on the abrupt change in temperature measurements as shown in Fig. 3.4 due to sudden change in its emissivity at the onset of melting. An IR camera (FLIR A655sc), an alternative infrared sensor with a working wavelength range of 7.5 to 14 μm and calibrated up to 2000℃ was used to align the system by acquiring temperature profiles from the top surface of the graphite disk.

3.3.2 Raman and Scanning Electron Microscopy

A custom Raman microscope with a 40 mW excitation laser at 532 nm and an imaging spectrometer (Horiba Ltd, iHR550) was used to assess graphene quality by calculating I_D/I_G ratios. The spectrometer utilizes a 2400 gr/mm blazed holographic grating optimized for the UV-Visible spectrum along with a visible back-illuminated Synapse-plus CCD camera sensor (Horiba Ltd, SYN-PLUS). The CCD camera sensor is thermoelectrically cooled to -95℃ with a resolution of 1024 x 256 in the wavelength range from 200 to 1100 nm. LabSpec6 software is used to acquire and analyze Raman spectra. A Zeiss Supra VP40 SEM at the Electron

Imaging Center for NanoMachines at the California NanoSystems Institute was used to assess the uniformity and characteristic grain sizes of samples using secondary electrons (SE) and backscattered electrons (BSE).

3.4 Thermal modeling of the substrate

Controlling the temperature of the copper substrate at different vacuum pressures and HFSS currents conditions enables variation of crucial input parameters for graphene growth. Thus, a steady-state numerical heat transfer model of a stationary copper substrate was developed and validated with peak temperature measurements acquired by the pyrometer.

3.4.1 Numerical heat transfer model

A numerical heat transfer model was derived for a circular copper substrate sitting atop a supporting tungsten disk with diameters of 50.8 and 88.9 mm, respectively. A steady-state assumption was adopted because graphene growth is established after the sample is heated and annealed under hydrogen gas for at least 15 min while the peak temperature asymptotes to a constant value. Because the system and HFSS are both radially symmetric and the copper and tungsten have relatively small thicknesses of 75 μm and 0.8 mm, respectively, the heat transfer model was assumed with a 1D radial temperature dependence in cylindrical coordinates without loss of accuracy. Both convection and radiation heat transfer were considered in this model. The control volume for the copper substrate interior nodes with all input and output heat transfer modes is illustrated in Fig. 3.5. The boundary condition for copper and tungsten at the center ($r = 0$) is $\mathrm{d}T/\mathrm{d}r|_{r=0} = 0$ due to symmetry. Additionally, the heat conduction loss from tungsten at $r = R_t$ is neglected due to the low thermal conductivity and contact area of the alumina washers. Thus, the boundary conditions at the

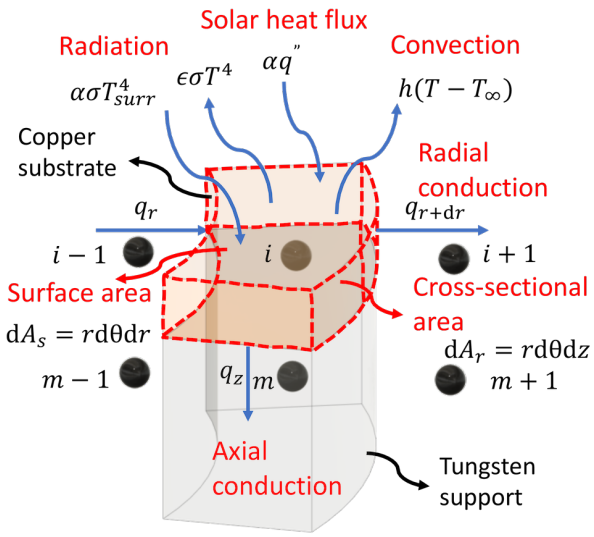

Figure 3.5: Control volume for the copper substrate interior nodes to illustrate input/output heat transfer modes.

copper substrate and tungsten disk outer radial edges are $-k\ \mathrm{d}T/\mathrm{d}r|_{r=R_c}$ and $-k\ \mathrm{d}T/\mathrm{d}r|_{r=R_t}$ $= [\varepsilon\sigma T^4 - \alpha\sigma T_{surr}^4 + h(T - T_\infty)]$.

The governing energy conservation equation for the copper substrate under steady-state conditions is defined as:

$$\frac{1}{r}\frac{\mathrm{d}}{\mathrm{d}r}\left(k\ r\ \frac{\mathrm{d}T}{\mathrm{d}r}\right) - \frac{q_z''}{\Delta z} - \frac{\varepsilon\sigma T^4}{\Delta z} + \frac{\alpha\sigma}{\Delta z}T_{surr}^4 - \frac{h}{\Delta z}(T - T_\infty) + \frac{\alpha}{\Delta z}q''(r) = 0 \tag{3.2}$$

where Δz is the substrate thickness, T is temperature, and k is temperature-dependent thermal conductivity; the term $\mathrm{d}k/\mathrm{d}r$ was evaluated as $(\mathrm{d}k/\mathrm{d}T)(\mathrm{d}T/\mathrm{d}r)$. Axial conduction (q_z'') governs the heat transfer between the two surfaces while taking into account the effect of contact resistant (R_{tc}'') as shown in Table 3.1, where the contact resistance is an engineering estimate intended to include all operative heat transfer modes. The tungsten disk follows a

Table 3.1: Thermal and optical properties of copper and tungsten. Based on data taken from Refs. [98, 113–126]

Thermal properties
$k_c(T) = 4.201 \times 10^2 - 6.509 \times 10^{-2} T$ (W/mK)
$k_t(T) = 2.693 \times 10^2 - 4.450 \times 10^{-1} T + 5.336 \times 10^{-4} T^2$ $-3.059 \times 10^{-7} T^3 + 6.702 \times 10^{-11} T^4$ (W/mK)
$T_\infty = 373$K
$T_{surr} = 373$K
$R''_{tc} = 1 \times 10^{-5}$(m^{2}K/W)
Optical properties
$\alpha_{solar,c} = \int_{0.22\mu\text{m}}^{2.5\mu\text{m}} \alpha_\lambda(\lambda) G_\lambda(\lambda) d\lambda / \int_{0.22\mu\text{m}}^{2.5\mu\text{m}} G_\lambda(\lambda) d\lambda = 0.18$
$\alpha_{solar,t} = \int_{0.23\mu\text{m}}^{2.5\mu\text{m}} \alpha_\lambda(\lambda) G_\lambda(\lambda) d\lambda / \int_{0.23\mu\text{m}}^{2.5\mu\text{m}} G_\lambda(\lambda) d\lambda = 0.40$
$\epsilon_c(T) = (\epsilon/\epsilon_n) \left[\int_{0.22\mu\text{m}}^{20\mu\text{m}} \epsilon_{\lambda n}(\lambda, T) E_{\lambda,b}(\lambda, T) d\lambda / \sigma T^4 \right]$
$\epsilon_t(T) = (\epsilon/\epsilon_n) \left[\int_{0.23\mu\text{m}}^{25\mu\text{m}} \epsilon_{\lambda n}(\lambda, T) E_{\lambda,b}(\lambda, T) d\lambda / \sigma T^4 \right]$
$\alpha_{surr,c}(T_{surr}) = 0.027$
$\alpha_{surr,t}(T_{surr}) = 0.089$

k: thermal conductivity, R''_{tc}: thermal contract resistance, ϵ: emissivity, and α: absorptivity, where subscript c: copper and t: tungsten

similar energy governing equation; however, the $q''(r)$ term disappears in the region under the copper substrate $r \leq R_c$, and q''_z disappears outside the copper substrate region $r \geq R_c$. The energy governing equation is discretized using central finite differences, and the remainder of the derivation is available in Appendix A.2.1.

3.4.2 Thermal and optical properties

Determination of the model thermal conductivity (k) and optical properties (ϵ, α) of both copper and tungsten is essential to achieve accurate temperature predictions from the numerical heat transfer model. Correlations for thermal conductivity as a function of temperature for both copper and tungsten were fitted from data by National Institute of Standards and Technology (NIST) [113] and are presented in Table 3.1.

Heat convection in this model was assumed to be due to natural convection inside the reactor because the inlet flow rate of the hydrogen is insignificant, as it is used only to fill and maintain the reactor at constant vacuum pressure. Based on a numerical study in a cylindrical enclosure with localized heating on the bottom surface which describes the creeping to laminar regime [127], the natural convection heat transfer coefficient was approximated from an average sample temperature of 1300 K at both 10 and 50 torr pressure (under hydrogen atmosphere) as 14.5 and 18.0 W/m^{2}K, respectively.

The normal spectral emissivity values from prior studies [98, 114–118, 121–126] of both copper and tungsten at elevated temperatures, which also have slight to negligible temperature dependence, were used to solve the total normal emissivity as:

$$\epsilon_n(T) = \frac{\int_0^\infty \epsilon_{\lambda,n}(\lambda,T)E_{\lambda,b}(\lambda,T)d\lambda}{E_b(T)} \tag{3.3}$$

where $E_{\lambda,b}(\lambda,T) = C_1/\lambda^5[\exp(C_2/\lambda T) - 1]$, $C_1 = 2\pi hc_o^2 = 3.742 \times 10^8$ W $\cdot$ μm^4/m^2, and $C_2 = (hc_o/k_B) = 1.439{\times}10^4 \mu$m$\cdot$K [120]. By adopting Kirchhoff's law, the spectral directional emissivity and absorptivity for opaque materials are related as: $\epsilon_{\lambda,\theta} = \alpha_{\lambda,\theta} = 1 - \rho_{\lambda,\theta}$. The normal absorptivity is computed as:

$$\alpha_n = \frac{\int_0^\infty \alpha_{\lambda,n}(\lambda)G_\lambda(\lambda)d\lambda}{\int_0^\infty G_\lambda(\lambda)d\lambda} \tag{3.4}$$

where $G_\lambda(\lambda)$ is the xenon arc lamp spectral output [119] as shown in Table 3.1. Because the solar beam irradiates the sample at a nearly normal direction, using the total normal absorptivity is a valid approximation.

However, the hemispherical, rather than normal, emissivity as a function of temperature is required to solve the numerical heat transfer model. To find the total hemispherical emissivity from the normal emissivity, electromagnetic wave and dispersion theories are involved. When electromagnetic waves impinge on the surface of a conducting medium (metals) with a complex index of refraction ($m = n - ik$) at angle θ from the normal to the surface, Fresnel's relation predicts well both parallel and perpendicular reflectivities for polarized light [98]. Thus, by using Kirchhoff's law and Fresnel's relations under the unpolarized light assumption ($\varrho = \frac{1}{2}(\varrho_{\parallel} + \varrho_{\perp})$) in the infrared region, the ratio $\epsilon_{\lambda}/\epsilon_{\lambda n}$ for metals can be approximated [98]. The complex indices of refraction n and k for copper and tungsten were experimentally measured by Ordal [128]. Additionally, studies have been carried out to investigate the ϵ/ϵ_n ratio experimentally for different polished metals [97, 129, 130].

Even though n and n/k for copper and tungsten vary with wavelength, the projected effects on ϵ/ϵ_n values were estimated with averages of 1.20 and 1.26, (corresponding also to the values near 2 μm, where the emissive power peaks at 1350 K) and an uncertainty within ± 0.05 in the dominant emission spectral range of this work. The hemispherical emissivity of both copper and tungsten are available in Table 3.1, and plots as functions of temperature are available in Appendix A.2.2. Calculated values of hemispherical emissivity of this work are close to reported values in the literature within the temperature range considered here [114, 130–132]. For radiation exchange with the surroundings, enclosure surfaces have a uniform temperature with an area ratio to the sample of at least 2-3 orders of magnitude. Thus the surrounding behaves like a blackbody.

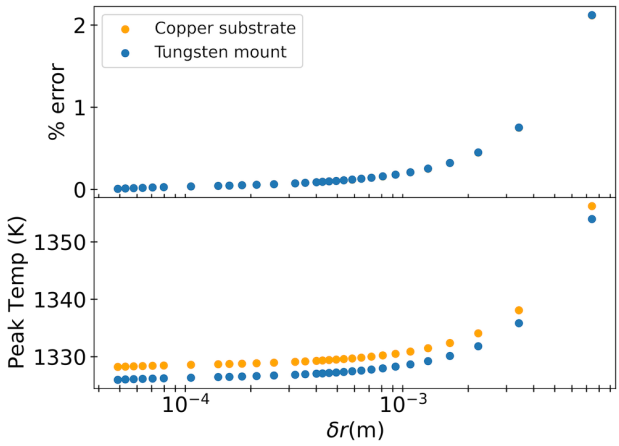

Figure 3.6: Percentage error and peak temperature from a grid independence study as a function of element size for the 1D numerical heat transfer model.

3.5 Results and discussion

3.5.1 Copper substrate temperature profile and uncertainty analysis

The 1D steady state numerical heat transfer model was used to compute the radial temperature profile of both the copper substrate and tungsten disk. First, a mesh independence study was conducted to find an optimum mesh size and to verify the accuracy of the heat transfer model. The effect of mesh size on peak temperature with respect to a very fine mesh were calculated and are shown in Fig. 3.6. Numerical stability was achieved at $\Delta r = 3\times\ 10^{-4}$ m; finer meshes increase computation time without significant improvement. The convergence criteria of the iterative numerical heat transfer model was set to a maximum relative temperature change of 1×10^{-9}.

By applying the numerical heat transfer model at a pressure and HFSS current of 10 torr of hydrogen and 106 A respectively, Fig. 3.7 illustrates the radial temperature profile of the copper substrate on a tungsten disk, where the peak copper temperature was compared

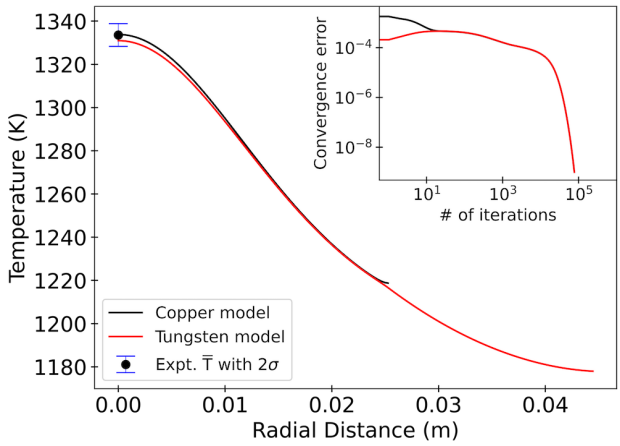

Figure 3.7: Temperature profile of copper substrate and tungsten mount from the numerical heat transfer model at HFSS current and pressure of 106 A and 10 torr respectively; the figure inset shows convergence of model temperature with iteration number

with measurements acquired by the pyrometer. The temperature profile of both copper and tungsten exhibit a Gaussian-Lorentzian radial profile due to the dominant effect of solar irradiance. The difference between the peak temperatures of copper and tungsten is due to contact resistance. The peak temperature as a function of HFSS current was further computed for a pressure of 10 torr as illustrated in Fig. 3.8a. In addition, Fig. 3.8b illustrates the peak temperature as a function of pressure while maintaining the HFSS current at 106 A. The relation between peak temperature and pressure exhibits a non-linear trend due to the combined non-linearities of Nusselt number, radiation and thermal conductivity with respect to temperature.

Results from the numerical heat transfer model were found to fall within two standard deviations of the mean value (2σ) of experimental measurements, or within 1% measurement uncertainty of a single measurement conducted at the same conditions. A maximum error of 2% is reported between the peak temperature from the numerical heat transfer model

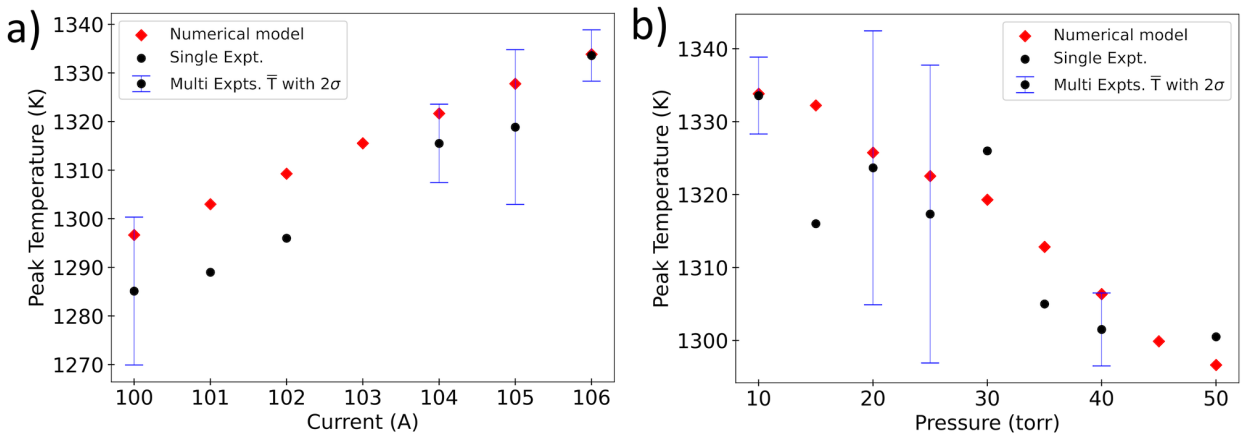

Figure 3.8: a) Peak temperature as a function of HFSS current at a pressure of 10 torr. b) Peak temperature as a function of pressure at a HFSS current of 106 A.

and temperature measurements acquired by the pyrometer. Appendix A.2.3 discusses the error of 100 tests carried out at various experimental conditions. Thus, the numerical heat transfer is considered to be validated.

A sensitivity analysis was carried out to assess the effects of uncertainties in the thermal and optical properties on the peak temperature value. The sensitivity coefficient is calculated as follows:

$$\frac{\partial T}{\partial x}\frac{x_0}{T_0} \approx \frac{T(x+\Delta x) - T(x-\Delta x)}{2\Delta x}\frac{x_0}{T_0} \tag{3.5}$$

where x is the studied parameter, Δx is its uncertainty, and T is the computed model peak temperature (x_0 and T_0 are substituted at standard conditions shown in Table 3.1). By employing $\pm 5\%$ uncertainties on the thermal and optical properties presented in Table 3.1, sensitivity coefficients were calculated as shown in Fig. 3.9. The sensitivity analysis indicates that parameters q''_{HFSS}, $\alpha_{solar,c}$, $\epsilon_t(T)$, $\alpha_{solar,t}$ and $\overline{h}$ have the highest impact on the peak

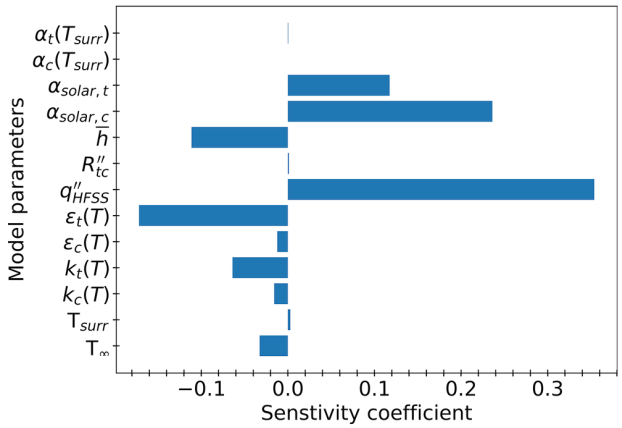

Figure 3.9: Sensitivity coefficients calculated from the effect of ±5% uncertainty in each of the model parameters on the peak temperature value. Subscripts c: copper and t: tungsten.

temperature and must be considered carefully. Positive sensitivity coefficients indicate that an increase in parameter increases the peak temperature, and vice versa.

The simplest way to understand uncertainty propagation of the thermal and optical properties to the peak temperature is via sampling. By employing sampling with Gaussian distributions, the propagation of random uncertainties up to ±5% in each of the five main parameters leads to uncertainty of ±2.5% in the peak temperature value. Furthermore, the peak temperature of the copper substrates was mapped into a contour as a function of both vacuum pressure and HFSS current as shown in Fig. 3.10 to visualize the peak value associated with relevant graphene synthesis conditions.

3.5.2 Synthesis of graphene

After building the solar thermal cold-wall CVD system and deriving a model that correlates HFSS current and vacuum pressure to the copper substrate peak temperature, graphene was synthesized on a circular copper substrate. Synthesis was carried out after heating the sample

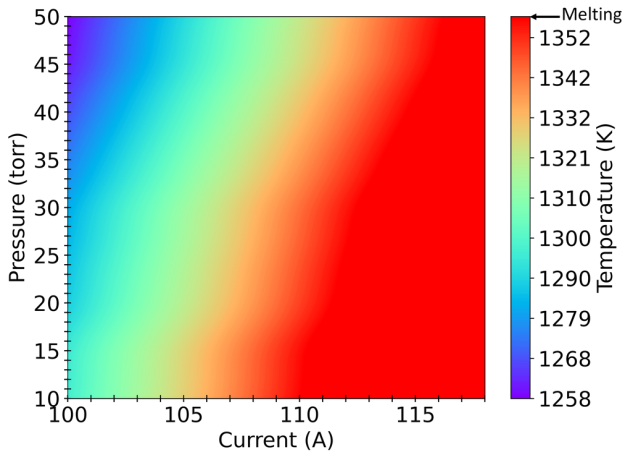

Figure 3.10: Peak temperature contour as a function of vacuum pressure (torr) and HFSS current(A).

with the HFSS under hydrogen atmosphere until its peak temperature reached a steady-state condition (about 15 min). A pyrometer was used to acquire temperature measurements from the center of the copper substrate prior to the synthesis process. Samples 1 and 2 were heated under HFSS heat fluxes with current settings of 100 and 106 A, respectively, which led to peak temperatures of 1006℃ and 1060℃ . To emphasize the importance of controlling and predicting the sample temperature, these samples were synthesized at different temperatures but with other conditions held the same. The other conditions adopted in this study follow: (1) gas ratio at 1:4 (CH_4:H_2) with H_2 flowing at 100 sccm and CH_4 at 25 sccm, (2) vacuum pressure of 10 torr, and (3) growth time of 5 min.

Using Raman microscopy, the quality of graphene on copper was further assessed from the I_D/I_G ratio. Sample 1 exhibits low graphene quality (I_D/I_G = 0.81) with D and G peak locations at 1350 and 1600 cm^{-1}, respectively. Conversely, sample 2 exhibits high graphene quality (I_D/I_G = 0.15) with D and G peak locations at 1350 and 1590 cm^{-1}, respectively. Sample 2 showed an additional 2D peak at 2700 cm^{-1} with FWHM of 44.2

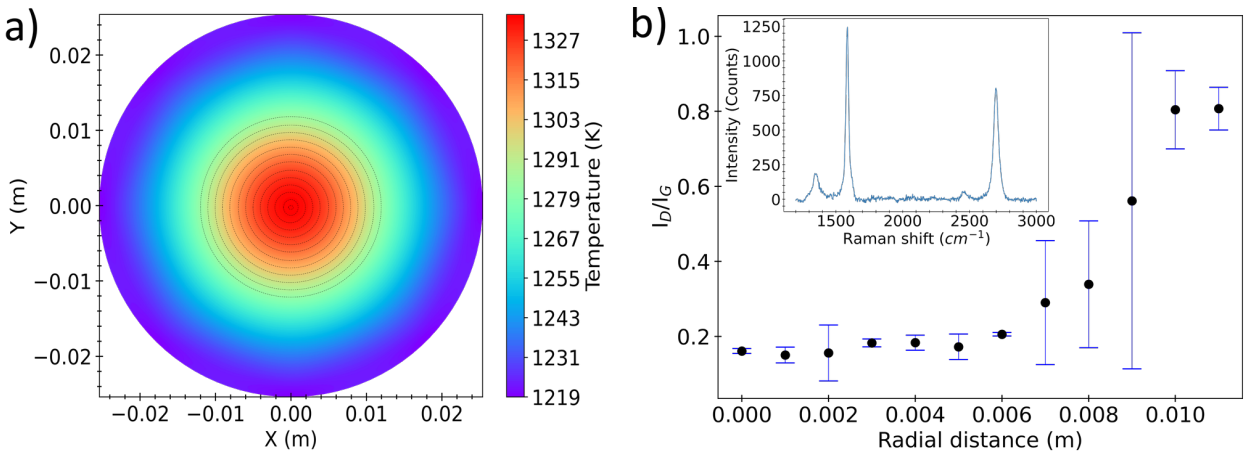

Figure 3.11: a) Sample 2 temperature profile under vacuum pressure of 10 torr, and HFSS current of 106 A. b) Processed Raman spectra for Sample 2 that demonstrates high graphene quality with an average $I_D/I_G = 0.17$ and circular spatial uniformity of 12 mm in diameter.

cm^{-1} and $I_{2D}/I_G = 0.646$, which indicates few-layer graphene. However, Raman 2D peak features of graphene on copper are mostly affected by photoluminescence with maximum intensity at 593 nm in room temperature [133] that results in background signal interference that hinders proper characterization compared to graphene on dielectric materials such as SiO_2/Si. This phenomenon arises from transitions between electrons from the conduction band below the Fermi level and holes in the d-band due to optical excitation [133]. The peak emission for copper has been found to be consistent with the optically observed energy of 2.0 eV between the upper d-band and Fermi energy [133]. Additionally, the effect of varying deposition time on graphene quality has been investigated. For deposition times of 1, 2, and 7.5 min, with other parameters the same as Sample 2 conditions, the quality of graphene tends to decrease, with I_D/I_G ratios of 0.62, 0.38, and 0.35, respectively. Figs. 3.11a and 3.11b show Sample 2 temperature profile and Raman measurements that indicate graphene uniformity within a circular area of 12 mm in diameter due to uniform temperatures around

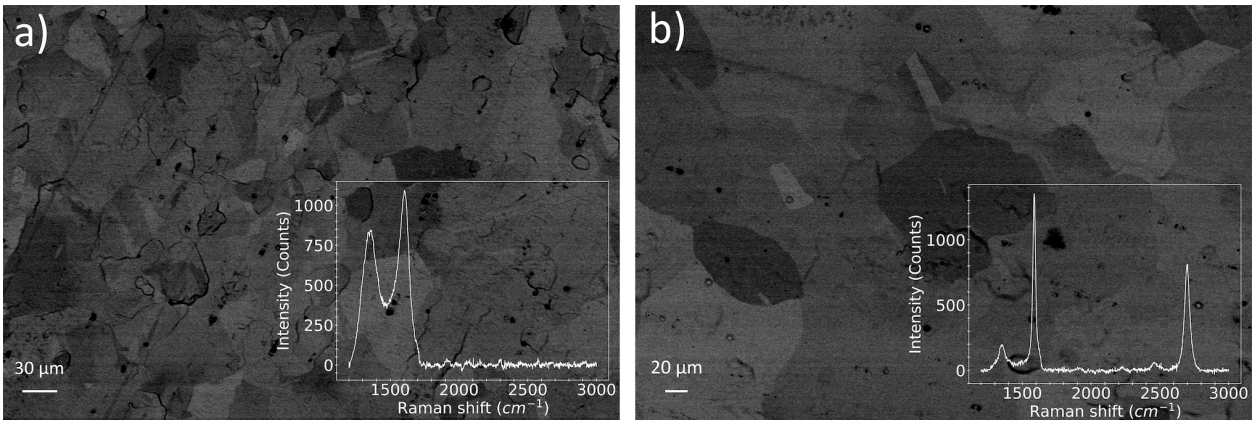

Figure 3.12: Scanning electron microscopy (BSE) images and raw Raman spectra of: a) Sample 1 showing low graphene quality from the Raman spectrum and small characteristic grain size, and b) Sample 2 showing high graphene quality from the Raman spectrum and large characteristic grain size.

1060℃ in that region. Furthermore, the two samples were analyzed by BSE microscopy as shown in Fig. 3.12. Sample 2 contains larger characteristic grain size of approximately 120 μm compared to 30 μm for Sample 1.

3.6 Conclusions

In this chapter, a custom-designed and built cold-wall solar thermal CVD system is illustrated to demonstrate the capabilities of using a renewable energy source in manufacturing processes, specifically graphene synthesis. A HFSS that includes a 10 kW_e xenon arc lamp with a controllable peak heat flux between 1.5 and 4.5 MW/m^2 was used to synthesize graphene on a copper substrate. Graphene synthesis is automated with controls and instruments to vary design parameters precisely such as substrate temperature (by varying the HFSS current), CH_4:H_2 gas ratio, vacuum pressure, and residence time. The temperature profile of the copper substrate was computed with a numerical heat transfer model, and

its peak was validated with experimental measurements acquired by a pyrometer at various operating conditions. Uncertainties in the thermal and optical properties were quantified by computing sensitivity coefficients, and their effects on peak temperature were further evaluated by employing Monte Carlo sampling. The quality of the synthesized graphene was analyzed by Raman microscopy and demonstrated high graphene quality with I_D/I_G = 0.17 for Sample 2. BSE images showed a characteristic grain size of 120 μm for high quality graphene on copper. Further work will be carried to increase the area of synthesized graphene and to optimize the objective function I_D/I_G (high graphene quality). The high-quality graphene synthesized in this work shows promising green-manufacturing capabilities suitable for photonic and electronic applications. Thus, further analysis is warranted to characterize graphene transmissivity, sheet resistance and lattice structure for various applications.

Chapter 4: Sequential Bayesian-optimized graphene synthesis by direct solar-thermal deposition

This chapter reports on the use of a high-flux solar simulator that mimics the solar spectrum and a cold-wall CVD reactor to demonstrate the feasibility of utilizing a renewable energy resource in synthesizing graphene under various conditions. A parametric study of graphene's growth parameters was carried out using a probabilistic Bayesian regression model and an information acquisition function to find optimal conditions that yield high-quality products. Backscattered electron images and Raman mapping were used to assess the effects of growth conditions on graphene characteristic sizes, film quality, and uniformity. We report the synthesis of high-quality single-layer graphene (SLG) and AB-stacked bilayer graphene films in a one-step and short time process during 5 min with I_D/I_G of 0.21 and 0.14, respectively. Electron diffraction analysis shows the plane spacing distance of graphene's lattice structure with diffraction peak intensities that resemble SLG and AB-bilayer graphene with up to 5 and 20 μm grain sizes, respectively. The optical transmissivity of SLG and AB-bilayer graphene is measured to be between 0.959-0.977 and 0.929-0.953, whereas the sheet resistance measured by a 4-point probe with 1 mm spacing was found to be 15.5$\pm$4.6 and 3.4$\pm$1.5 kΩ/sq, respectively. Direct solar capture for CVD synthesis creates a practical option in synthesizing high-quality graphene films applicable for photonic and electronic applications.

4.1 Introduction

Graphene is a two-dimensional material with carbon atoms arranged into a hexagonal lattice structure [134, 135]. Its remarkable properties make it a compelling candidate in many photonic and electronic applications [4–6, 8–10, 12, 13]. One of the most common methodologies in graphene synthesis is growth by chemical vapor deposition (CVD) using plasma or electric heating sources. CVD techniques have many advantages, and they remain the most efficient method for mass production by employing roll-to-roll processing [17, 18] and allow some control of both graphene quality and thickness through growth kinetics and thermodynamics [26–29, 136, 137].

Some have utilized CVD mechanisms to exploit the effect of temperature on the kinetics that governs nucleation, grain growth, and film thickness [26, 30]. Others have modulated vacuum pressure and catalyst substrate solubility to improve thickness uniformity and defect density [27]. Hydrogen concentration has been found to influence grain sizes and the number of layers because it serves as an etchant and activator for carbon bounds [28]. Such studies [13, 26–29] have demonstrated that graphene synthesis at high temperatures, low pressures, and high H_2 concentrations (low CH_4:H_2 ratio), generally lead to higher graphene quality, larger grain sizes, reduced nucleation density, and uniform (single or bilayer) films. Further, simulations of graphene growth have been conducted through a validated COMSOL model to study growth thermodynamics, kinetics in the gas phase, and surface reactions [136]. Additionally, kinetic models have also been derived to assess graphene growth on different transition metal catalysts such as Co, Ni, and Cu while taking into account carbon permeation effects, process thermodynamics, and carbon solubility [34].

Statistical techniques such as factorial designs [138] are less effective in finding the optimum conditions for graphene synthesis due to their complexity, especially while studying a large number of parameters. To deal with stochastic optimization of the I_D/I_G Raman peaks ratio, a Gaussian process regression model and an acquisition function that quantifies the model information [17, 40, 139–141] are employed here. Here, we demonstrate using a HFSS and a cold-wall CVD reactor to execute a parametric study on graphene growth parameters. The added novelty to graphene growth through the CVD mechanism is utilizing solar energy, a renewable energy resource, and demonstrating the practicality of using such a heat source in graphene fabrications to synthesize high-quality SLG and AB-stacked bilayer graphene films.

4.2 Experimental Setup

4.2.1 Solar-thermal CVD system

A custom-built high flux solar simulator (HFSS) characterized [38] in chapter 2 and integrated with a custom-built CVD system [39] in chapter 3 are used here. A related numerical heat transfer model has been developed and validated [39] in chapter 3 for a stationary circular copper substrate (50.8 mm in diameter and 76 μm thick). To facilitate the synthesis process, the model predicts the substrate temperature profile at various HFSS current and vacuum pressure conditions prior to graphene growth. Fig. 4.1 illustrates an overview of solar-thermal CVD setup used in graphene synthesis and a flow chart for graphene synthesis parameters.

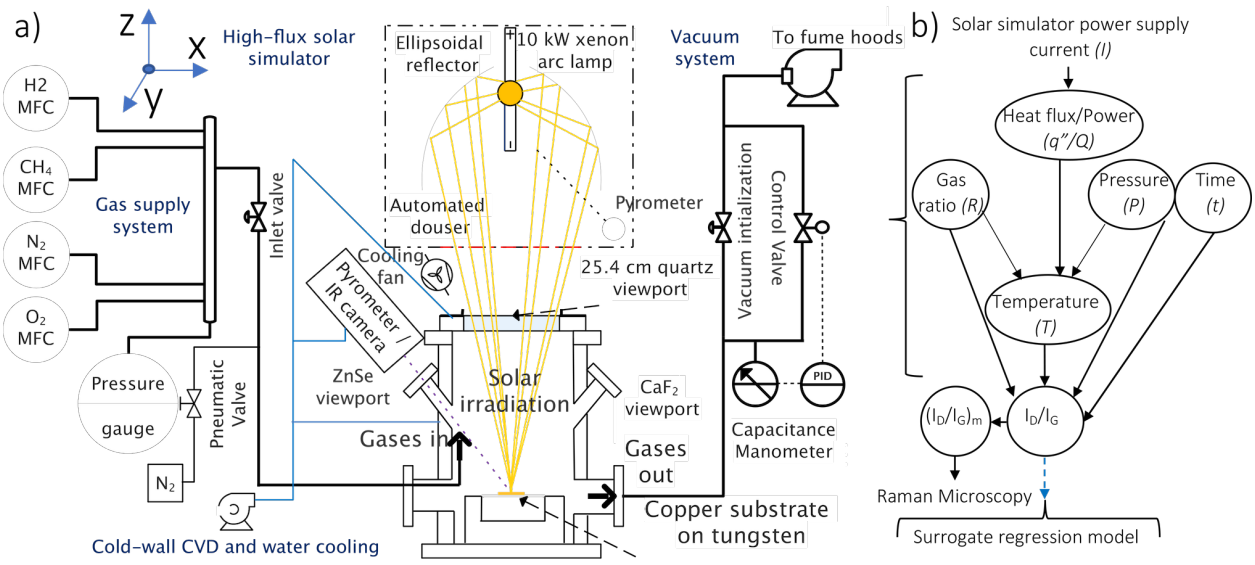

Figure 4.1: a) Overview of solar-thermal CVD setup for graphene synthesis. b) Flow chart for graphene synthesis parameters.

4.2.2 Graphene transfer process

To characterize synthesized graphene in this work, graphene films were transferred to 50.8 mm fused silica (500 μm thick) and thermal oxide (300 nm SiO_2 on 270 μm thick Si) circular wafers (University Wafer, Inc) to assess graphene transmissivity and sheet resistance, respectively. TEM mesh grids (Tedpella, inc) with ultra-thin carbon support (3 nm) on copper are used for electron diffraction. A wet transfer methodology was adopted in this study. At first, PMMA powder (Sigma-Aldrich) is used to prepare a solution with (20 mg/mL) concentration [142] as support for graphene films. PMMA solution is then spin-coated on the graphene/copper substrates at 1000 rpm for 30 s and allowed to dry in the air for 24 hours. The copper substrate is etched at room temperature with iron(III) chloride ($FeCl_3$) solution (0.5 molar concentration) for 12-24 hours [143], after which the PMMA/graphene film floats to the surface of the solution. The film is rinsed thoroughly by replacing the

solution with distilled water using a syringe. The target substrate is then placed at 30° underneath the floating film. The film is lowered onto the substrate by pulling out the water with a syringe. A needle is used to position and pin the film edge to the substrate during the transfer process. The sample is then heated at 180℃ in air for 30 min to flatten the graphene film and rinsed thoroughly in an acetone bath to remove PMMA/$FeCl_3$ residuals.

4.2.3 Characterization instruments

Raman spectra are used to assess graphene quality by calculating the intensity ratio of defects in graphene lattice to sp2 carbon structure due to C-C in-plane vibrations (I_D/I_G) [41]. A custom-built Raman microscope equipped with 40 mW excitation laser at 532 nm, 40X objective lens, and integrated with an imaging spectrometer (Horiba Ltd, iHR550) are employed for I_D/I_G measurements of graphene atop copper used in the optimization algorithm. The spectrometer contains a 2400 gr/mm blazed holographic grating and Synapse plus CCD camera (Horiba Ltd, SYN-PLUS). Graphene film transmissivity is estimated using a calibrated photodiode detector that converts 532 nm laser optical power to electrical current. A Renishaw inVia Raman microscope at the UCLA MSE department equipped with 5 mW excitation laser at 488 nm, 50x objective lens, and 1200 gr/mm grating is used for Raman mapping.

Graphene sheet resistance is measured using 4-point probes (CDE ResMap 178) with 100 μm tip radius, 1 mm spacing, and 100 g force at the Nanolab in the California NanoSystems Institute (CNSI). Graphene film uniformity and characteristic size are studied by backscattered electron (BSE) using a Zeiss Super VP40 scanning electron microscope (SEM) at the Electron Imaging Center for NanoMachines (EICN) at CNSI. Graphene hexagonal lattice

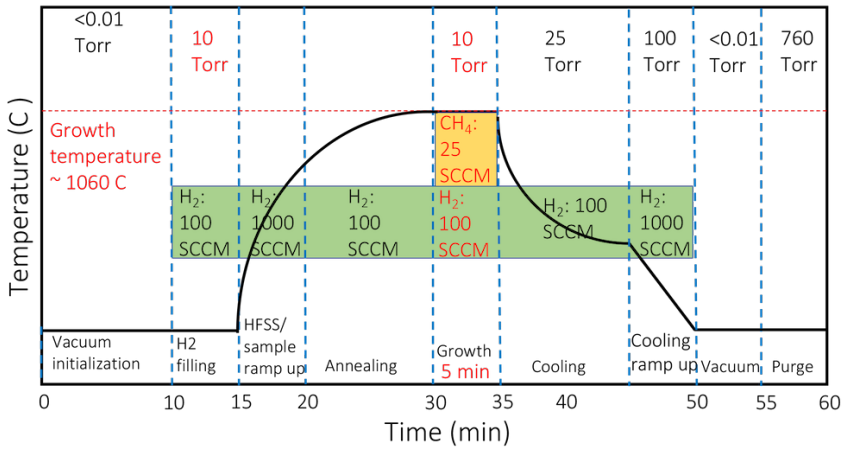

Figure 4.2: Diagram that summaries the experimental procedures, conditions and duration carried out for graphene synthesis

structure, grain sizes and boundaries, plane spacings, and the number of layers and orientation are analyzed using electron diffraction by a FEI T12 transmission electron microscope (TEM) with 80 keV at EICN.

4.3 Design of experiment and objective function optimization

4.3.1 Experimental procedures

A typical graphene synthesis growth process is illustrated in Fig. 4.2, which shows the experimental durations and conditions of each step. At first, the sample is loaded into the reactor, and vacuum initialization is established to achieve a vacuum pressure of 10^{-3} torr. Thereafter, reactor filling with hydrogen is initiated to reach the pressure required for graphene synthesis. Based on the desired sample temperature at various H_2 gas pressures, the HFSS total power with the corresponding current setpoint is predicted from the numerical thermal model [39] in chapter 3. Ramping up the solar simulator is essential to ensure that the lamp reaches its steady-state condition, which takes about 15 min [38]. Additionally, annealing

Table 4.1: Design of experiment parameters with lower and upper limits

Parameters	Lower limit	Upper limit
Temperature (℃)	1000℃	1075℃
Pressure	5 torr	50 torr
Methane (CH4)	10%	50%
Hydrogen (H2)	50%	90%
Time (min)	1 min	10 min
HFSS current (A)	100 A	115 A

the sample removes oxidation from copper and provides mechanical annealing and softening to the copper substrate. A pyrometer then acquires the temperature of the sample prior to graphene synthesis.

Graphene growth is established by introducing methane flow and setting the CH_4:H_2 gas ratio for a specific growth time. Once graphene synthesis is completed, the HFSS is switched off, and the sample is allowed to cool by increasing H_2 gas pressure gradually to 25 torr. The cooling of the sample is accelerated by increasing H_2 flow to 1000 sccm, allowing the reactor pressure to reach 100 torr. The reactor is then evacuated to remove H_2 gas residuals while ensuring the substrate temperature is below 50℃. Finally, the reactor is purged with N_2 gas to atmospheric pressure, and the sample is removed. The overall graphene synthesis process takes about 60 min, and the variable design parameters in this study are denoted in red in Fig. 4.2. The process parameters with their limits are shown in Table 4.1, and the gas composition is constrained as: $H_2(\%) + CH_4(\%) = 100\%$.

4.3.2 Probabilistic design of experiments (DoE)

A probabilistic surrogate model is adopted to find the conditions that minimize I_D/I_G and optimize graphene synthesis. This problem is a stochastic single-objective optimization,

with a Bayesian global optimization design strategy, that does not assume any form for the fitted function. The process parameters taken into consideration are the copper substrate temperature, vacuum pressure, CH_4:H_2 gas ratio, and time.

A Gaussian process (GP) is implemented by creating a multivariate Gaussian distribution of the four parameters above [40]:

$$f(\cdot) \sim \mathrm{GP}\left(m(\cdot), k(\cdot,\cdot)\right), \tag{4.1}$$

where m is the mean function of Gaussian processes and k is the covariance function. Taking $\mathbf{x}_{1:n} = \{\mathbf{x}_1, \ldots, \mathbf{x}_n\}$ as the input parameters and $\mathbf{f}$ as the output (I_D/I_G), $f(\cdot)$ is evaluated on each of the elements of $\mathbf{x}_{1:n}$. Using Bayes' rule, the posterior probability metric over the space of functions is defined as [40]:

$$p(f(\cdot)|\mathcal{D}) \propto p(\mathcal{D}|f(\cdot))p(f(\cdot)), \tag{4.2}$$

where $p(f(\cdot))$ is the prior, $p(f(\cdot)|\mathcal{D})$ is the posterior, and $p(\mathcal{D}|f(\cdot))$ is the likelihood of the data. The objective function being optimized in this algorithm is defined:

$$\mathbf{x}^* = \arg\min_{\mathbf{x}} f(\mathbf{x}). \tag{4.3}$$

The algorithm starts with an initial data set consisting of input-output observations that is used to quantify the state of knowledge about $f(\mathbf{x})$, and the Gaussian process is updated to obtain a predictive distribution as shown in Fig. 4.3. The probabilistic surrogate model in this work utilizes epistemic uncertainty (deficiencies due to limited knowledge and un-

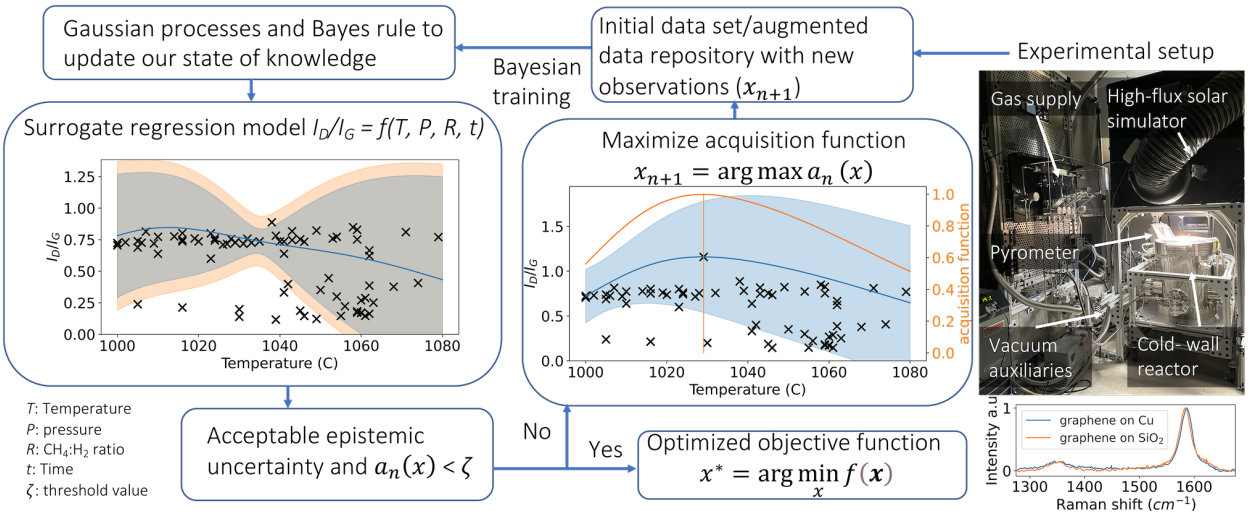

Figure 4.3: Process diagram for the design of experiment (sequential information acquisition algorithm and objective function optimization)

certainties in measurements due to manufacturing imperfections and operation) to define an information acquisition function (IAF). The expected improvement over the dominant hypervolume (EIHV), a common form of IAF, is implemented to handle measurement noise and parametric uncertainties [139]. By maximizing an acquisition function ($a_{n_0}(\mathbf{x})$) that depends on the current state of knowledge, the most important point is picked and evaluated [40] as follows:

$$\mathbf{x}_{n+1} = \arg\max a_n(\mathbf{x}). \tag{4.4}$$

The function is evaluated at $\mathbf{x}_{n+1}$, where function evaluation is executed by conducting a new experimental set. The original data set is then augmented by new observations, where Bayes' rule is used to update the state of knowledge. Thus, the IAF helps to quantify the methodology of evaluating the objective function with new parameters by solving this process iteratively until acceptable epistemic uncertainty or a threshold value is achieved.

4.4 Results and discussions

4.4.1 Surrogate regression model

The surrogate regression model minimizes the objective function I_D/I_G and finds the optimum parameters for graphene growth (temperature, vacuum pressure, CH_4:H_2 ratio, and growth time). Raman measurements from experimental sets update the state of knowledge of the regression model and are acquired directly from synthesized graphene on copper for ease of processing by averaging the results from five spots. Fig. 4.3 illustrates similar Raman spectra that compare graphene's D and G peaks acquired from atop of the copper substrate and to that transferred to fused silica. The results indicate that the acquired Raman spectra are not affected by interference from the copper substrate (99.9% C11000 alloy foil, Revere Copper Products Inc.) for graphene D and G peaks.

With the xenon arc lamp is placed at the focal point of a truncated ellipsoidal reflector and the copper substrate at the target focal plane, the heat flux on the substrate is most concentrated. The thermal model derived in chapter 3 predicts the substrate's temperature (measured later by a pyrometer) at various conditions and thus facilitates conducting experiments to optimize the objective function I_D/I_G.

The DoE starts with an initial Set 1 carried out systematically by varying one design parameter within the ranges shown in Table 4.1, where others are held constant. Sets 2-3 were carried out under various conditions by inspecting the surrogate regression model and conducting the experiment in spaces that lack observations, where each initial set consists of 20 experiments. Sets 4-6, each with around 15 experiments, were carried out based on the algorithm and suggested experiments that maximize the model's information. The

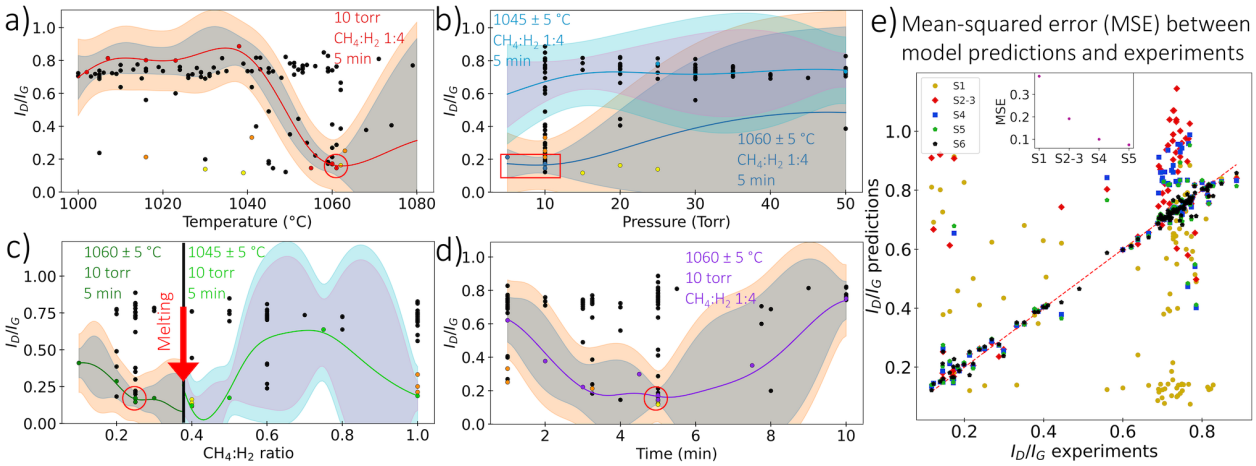

Figure 4.4: The objective function I_D/I_G from the surrogate regression model as a function of a) temperature, b) pressure, c) CH_4:H_2 ratio, and d) time by varying one parameter and the others are held constant. The red circle denotes the same optimized condition viewed from a different spatial perspective. The yellow and orange experimental points show good conditions but do not belong to these spaces. *Note: experimental observations denoted in black, yellow, and orange points do not belong to these spaces but only share the main x and y-axis, due to the projection of 5-dimensional space onto a 2-dimensional plot. e) Mean-squared error (MSE) between the I_D/I_G predicted by the model and observed from experiments, showing the MSE and improvement of the model's prediction of the 109 conditions after updating its state of knowledge with new sets.

mean-squared error (MSE) between the model predicted objective function (I_D/I_G) and experimental observations is shown in Fig. 4.4e. The MSE shows pronounced improvement in model predictions of the 109 different conditions after iteratively updating its state of knowledge with new observations.

The final results for the objective function I_D/I_G from the surrogate regression model are illustrated in Fig. 4.4 as a function of a) temperature, b) pressure, c) CH_4:H_2 ratio, and d) time, where each parameter is varied while others are held constant. Due to the projection

of a 5-dimensional space onto a 2-dimensional plot, black, yellow, and orange experimental points do not belong to these spaces; they only share the main variable parameter on the x-axis and I_D/I_G on the y-axis. The optimized conditions from the surrogate regression model are a temperature of 1060℃, gas ratio CH_4:H_2 of 1:4, and a growth time of 5 min with a vacuum pressure of 5 torr for SLG and 10 torr for AB-stacked bilayer graphene. The red circle denotes the same optimized condition viewed from a different spatial perspective.

4.4.2 Characterization of different conditions

BSE images and Raman mapping of graphene on Cu and transferred thermal oxides, respectively, were used to assess the effects of different conditions on preferential graphene growth characteristic size within certain crystallographic orientations of Cu [43], film quality, and uniformity. The DoE results indicate that high temperature leads to high graphene quality, as illustrated in Fig. 4.4a. Kim et al. [26] attribute graphene synthesis to the crystallization of a supersaturated carbon-adatom species. The nucleation density is governed by phenomena that vary with temperature, with activation energy between (1-3 eV). The decrease in nucleation density (larger grain size) with temperature is attributed to an increase in the probability of capturing supercritical carbon nuclei from the gas feed over initiating nucleation on newly available substrate sites because of increased desorption rates [26]. In addition, high temperature enhances dissociation of carbon precursor (CH_4) as well as enlarging copper grain sizes while smoothing its surface [25]. Fig. 4.5a shows BSE images and Raman mapping of graphene synthesized at 1016, 1038, 1050, and 1060℃, respectively, while other parameters are held at optimized conditions. Nanocrystalline graphene's Raman signature [41] is dominant at the lowest temperature (1000℃), with high defects and

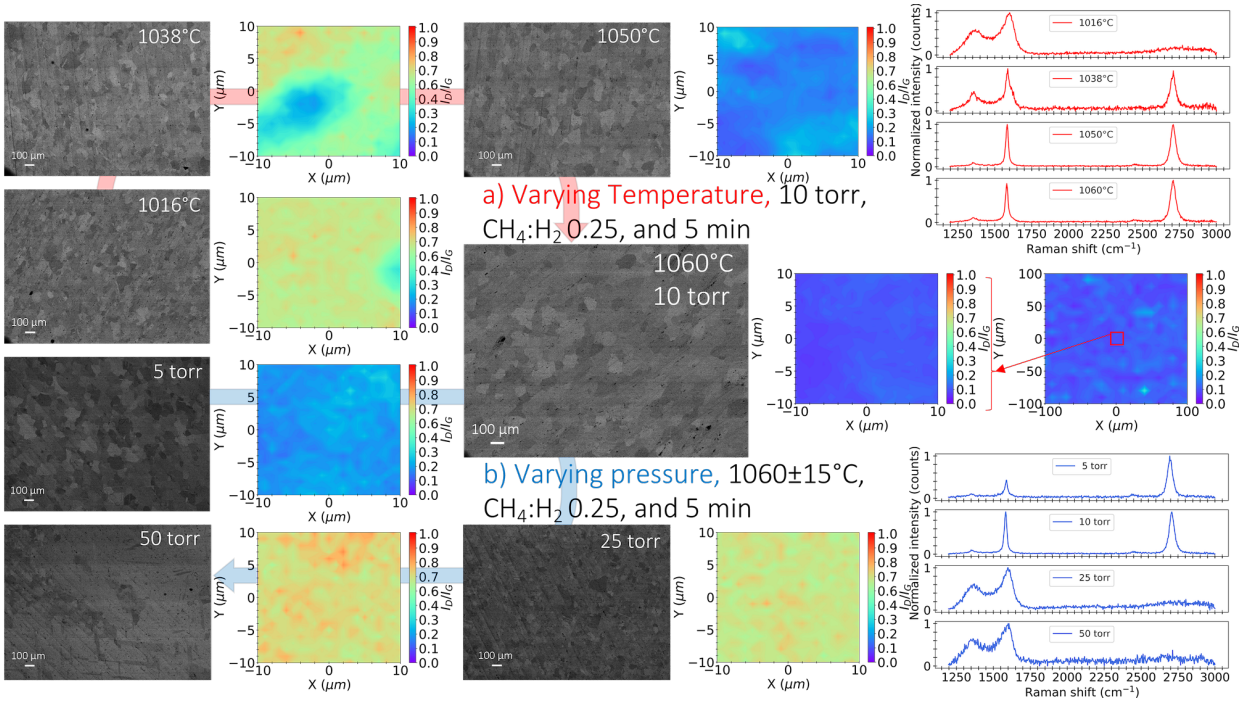

Figure 4.5: BSE images and Raman mapping that show graphene characteristic sizes and film uniformity from Raman measurements (I_D/I_G) synthesized at different a) temperatures (1016, 1038, 1050, and 1060°C) and b) pressure (5, 10, 25, and 50 torr), while other parameters are held at optimized conditions. Optimized graphene shows Raman uniformity (I_D/I_G) over a characteristic length of 20 and 200 μm.

small characteristic sizes from BSE images of graphene on Cu. In contrast, high-quality with AB-bilayer graphene growth is observed at higher temperatures (1060℃) with large characteristic sizes. At 1060℃, high-quality uniform graphene is achieved with I_D/I_G and characteristic sizes of 0.11 and 100 μm, respectively, compared to lower-quality graphene at 1016℃ with 0.62 and 20 μm.

Low pressure leads to high-quality graphene, as shown in Fig. 4.4b. In general, the cooling rate, geometry of the reactor, and pressure are important factors in graphene growth kinetics, density of defects, and thickness uniformity [27]. At low pressures, growth is limited by the surface reaction regime, which is highly sensitive to temperature uniformity. The flux of active species is reduced in the low-pressure regime, leading to fewer collisions and enhanced diffusion through the boundary layer, as explained in work by Bhaviripudi et al. [27]. By increasing pressure, diffusion through the boundary layer becomes the limiting factor, where the geometry of the reactor and gas flow affects the thickness of the boundary layer, leading to non-uniform graphene [27]. Fig. 4.5b shows BSE images and Raman mapping of graphene synthesized at 5, 10, 25, and 50 torr, respectively, with other parameters held at optimized conditions. At low pressures (5-10 torr), high-quality graphene is achieved with I_D/I_G = 0.11-0.21 and characteristic sizes up to 100 μm. Based on Raman, 5 and 10 torr favor the growth of SLG and AB-stacked graphene, respectively. Conversely, high pressure leads to deterioration of graphene quality (I_D/I_G = 0.68) with discontinuous films even at slightly reduced temperature from 1060 to 1045℃ as shown in Fig. 4.5b.

High hydrogen concentrations (low CH_4:H_2 ratios) in graphene growth produce high-quality films as presented in Fig. 4.4c. Hydrogen has a double role that facilities methane chemisorption as an activator of surface-bound carbon and an etching reagent that controls

the size and morphology of graphene grain as demonstrated in work by Vlassiouk et al [28]. Hydrogen also counteracts the negative impact of the oxidizing contaminants in copper foil or stray oxygen in the gas feed during the synthesis [28]. Additionally, the decrease in methane partial pressure (concentration) leads to lower in nucleation density [26]. Fig. 4.6a shows BSE images and Raman mapping of graphene synthesized at 0.1, 0.25, 0.5, and 1 CH_4:H_2 ratios, respectively, with other parameters held at optimized conditions. A CH_4:H_2 ratio of 0.25 is the optimized condition with $I_D/I_G = 0.11$, where smooth edges and large characteristics sizes up to 100 μm are observed. Further reduction of the gas ratio to 0.1 produces a SLG signature and worsens graphene quality ($I_D/I_G = 0.41$) with small characteristic sizes and discontinuous/nonuniform film coverage, as shown in Fig. 4.6a.

Synthesis at a higher gas ratio ($\geq$0.4) leads to the melting of copper if the synthesis is performed at high temperatures around 1060℃ (close to copper melting point), and for a long duration (>2 min) as shown in Fig. 4.4c. The increase in temperature of the sample during the growth is due to the significant reduction in hydrogen partial pressure in the chamber by introducing a higher concentration of CH_4 gas, where hydrogen's effects as a cooling agent with higher thermal conductivity is reduced. To achieve synthesis at higher CH_4:H_2 ratios, the temperature was reduced to 1045℃ prior to growth. However, the synthesis starts to follow a transient heat and flow regime in which temperature changes during graphene growth. Excessive methane supply leads to non-uniform graphene films and the growth of a large number of layers despite the observed low I_D/I_G ratio with CH_4:H_2 ratio of >0.5. The growth process for CH_4:H_2 ratios in the range 0.5-1 involves the adverse effect of increased CH_4:H_2 ratio (increased nucleation density) and the positive effect of high temperature close to the melting point. According to Xing et al. [30], the carbon consumed during

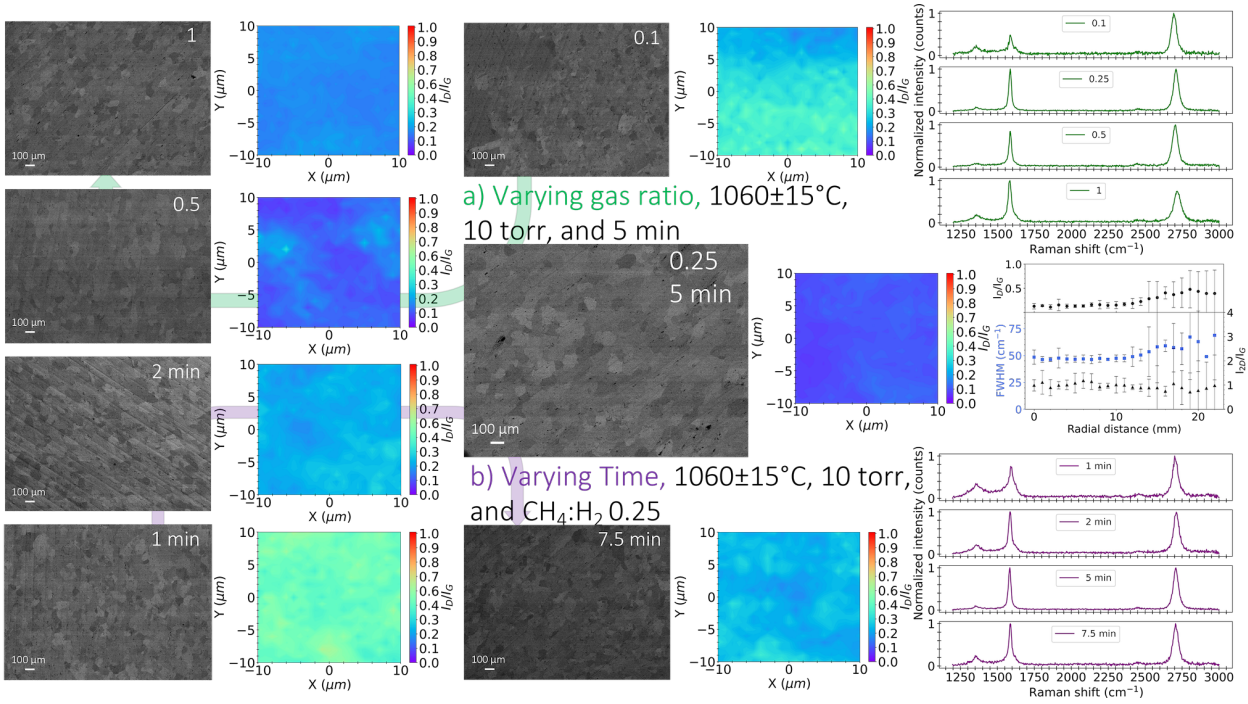

Figure 4.6: BSE images and Raman mapping that show graphene characteristic sizes and film uniformity from Raman measurements (I_D/I_G) synthesized at different a) CH_4:H_2 ratio (0.1 0.25, 0.5, and 1) and b) time (1, 2, 5, and 7.5 min), while other parameters are held at optimized conditions. Optimized graphene shows Raman uniformity (I_D/I_G, I_{2D}/I_G, and FWHM) with spatial uniformity up to 15 mm radius. Error bars show the uncertainty of radial measurements at an increment of 1 mm with four different angular positions (0°, 90°, 180°, and 270°) and an increment of 5 mm with eight different angular positions (0°, 45°, 90°, 135°, 180°, 225°, 270°, and 315°).

nucleation reduces as temperature increases, favoring the growth of single layer graphene and the increase in graphene's island size. Thus, the reason that the quality of graphene improves towards CH_4:H_2 ratio of 1 might be attributed to the abrupt increases in the sample temperature during the synthesis due to reduced hydrogen content, and the consumed C during nucleation is reduced even though the concentration of CH_4:H_2 is high, leading to high graphene quality.

Growth time is a unique feature associated with the solar-thermal CVD due to the effect of heat flux impingement on the surface and the direct rapid heating of the substrate in a short time, with the walls kept cool. Fig. 4.4d shows that between 3.5 to 5.5 min, graphene synthesis produces a similar quality and continuous films. Fig. 4.6b shows BSE images and Raman mapping of graphene synthesized at 1, 2, 5, and 7.5 min, respectively, with other parameters held at optimized conditions. At 5 min, high-quality graphene is achieved with averaged $I_D/I_G = 0.11$ and characteristic sizes up to 100 μm, whereas reduced and increased synthesis durations of 1 and 7.5 min show I_D/I_G of 0.47 and 0.26, respectively.

The yellow and orange points represents good conditions but do not belong to these spaces. The yellow points correspond to the synthesis of graphene at higher vacuum pressure between 15-25 torr and gas ratio CH_4:H_2 of 0.4 with a temperature of 1045℃ for 5 min. The results show macroscopically non-uniform but high-quality graphene films. As noted earlier, increasing pressure and gas ratio adversely affects graphene uniformity by introducing a non-uniform boundary layer and excessive supply of methane, respectively, which lead to the deposition of less uniform graphene films. The orange points correspond to the synthesis of graphene at a vacuum pressure of 10 torr and gas ratio CH_4:H_2 of 1. Synthesis was carried out either at a higher temperature of 1060℃ for a short time of 1 min or a lower temperature

of 1000℃ with a longer duration of 3 min, leading to high graphene quality with I_D/I_G <0.25. The former is attributed to the fact that the partial pressure of methane is still low within one minute of growth and mixed with higher hydrogen concentration (actual CH_4:H_2 <1), which explains the high graphene quality despite the gas ratio set point and without melting the sample. The later is attributed to the transient heat transfer and the abrupt changes in temperature during the synthesis process that counteract the adverse effect of high CH_4:H_2 as discussed earlier. Table 4.2 shows the averaged metrics I_D/I_G, I_{2D}/I_G, and FWHM from Raman mapping of the different experimental conditions.

4.4.3 Characterization of graphene with single and AB-stacked bilayer Raman signatures

After optimizing graphene synthesis with conditions that produce high-quality SLG and AB-stacked bilayer graphene, further characterization was carried out to assess lattice structure, grain size, number of layers and orientation, film transmissivity, and sheet resistance. Electron diffraction analysis of graphene on TEM grids shows different patterns that vary from a single grain to polycrystalline graphene [144]. Synthesis of graphene on polycrystalline Cu that contains different grain sizes and surface conditions affects graphene nucleation density, grain sizes, and boundary shapes [26]. Therefore, electron diffraction for a single grain of a SLG and AB-stacked bilayer graphene with 5 μm and 20 μm sizes (aperture sizes), respectively, were used to characterize synthesized graphene films as shown in Figs. 4.7a and 4.8a. The difference between graphene grain size evaluated by electron diffraction and characteristic sizes by BSE analysis of graphene on Cu can be attributed to the formation of multiple smaller graphene islands (grains) due to increased nucleation density [26] within

certain crystallographic orientation of copper [43], as well as induced wrinkles, overlap, and adlayers during the transfer process [142, 145, 146].

The lattice hexagonal patterns of graphene from electron diffraction analysis illustrate plane spacings d_{11}, and d_{10} of 0.12, and 0.21 nm, respectively, and a d_{10}/d_{11} ratio of about $\sqrt{3}$. Thus, the lattice constant ($\tilde{a}$) for graphene is approximated as 0.14 nm. Diffraction intensity ratios labeled by Bravis-Miller indices from outer peaks of equivalent planes [1-210] to inner peaks from equivalent planes[1-100] (I_{1-210}/I_{0-110} and I_{-2110}/I_{-1010}) are approximately 0.5 for monolayer graphene and 2 for AB-stacked bilayer graphene [12, 13, 147]. Figs. 4.7b and 4.8b show diffraction intensities near 0.5 for SLG and 2 for AB-Stacked bilayer graphene, respectively.

Raman mapping was conducted on graphene transferred to SiO_2/Si to characterize graphene coverage and number of layers statistically. The Raman spectrum of SLG has distinctive features, and the 2D peak is symmetric with FWMH and I_{2D}/I_G values of 34-45 cm^{-1} and 1.8-2.8, respectively [13, 25–27, 34, 36, 148]. Figs. 4.7c and 4.7d show Raman mappings of I_{2D}/I_G and FWHM, respectively, carried out on a squared area with 20 μm characteristic length. Additionally, the distribution of FWHM and I_{2D}/I_G of SLG at six different locations are illustrated in Figs. 4.7e and 4.7f. Here, we observe 2D peak features consistent with SLG, with averaged I_{2D}/I_G and FWHM of 2.39 and 39.2 cm^{-1}, respectively, and fitted with one Lorentzian as shown in the inset of Fig. 4.7f. Thus, the results reveal a uniform graphene film with about 93% SLG coverage based on these Raman features.

On the other hand, the Raman spectrum of AB-stacked bilayer graphene has distinctive features as well, where the 2D peak is asymmetric with FWMH and I_{2D}/I_G values of 40-62 cm^{-1}, and 0.75-1.46, respectively [12, 13, 147]. Additionally, studies have indicated that

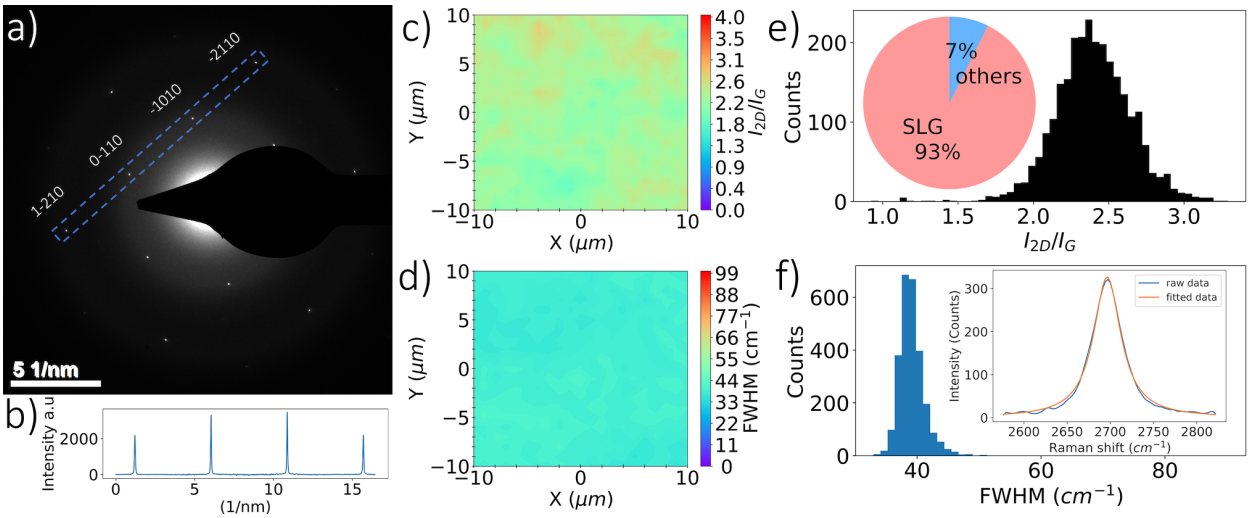

Figure 4.7: Single-layer graphene characterization: a) Electron diffraction from a single graphene grain of 5 μm (aperture size). b) Intensity profile within the blue dashed box in part (a) showing outer peaks of equivalent [2100] planes and inner peaks from equivalent [1100] planes. Raman mapping illustrates uniformity of c) I_{2D}/I_G and d) FWHM over characteristic lengths of 20 μm acquired from graphene on 300 nm SiO_2/Si. e) Statistical distribution of I_{2D}/I_G, where the inset estimates the stacking ratio of SLG when compared to other Raman spectra of few-layer graphene. f) Statistical distribution of FWHM, where the inset shows the 2D Lorentzian fit of SLG.

the AB-stacked graphene's electronic structure is uniquely captured with Raman, where a double resonant Raman process due to electronic band changes is observed, and the 2D peak is split into four components [149]. Figs. 4.8c and 4.8d show Raman mappings of I_{2D}/I_G and FWHM, respectively, carried out on a squared area with 20 μm characteristic length. Additionally, the distributions of FWHM and I_{2D}/I_G of AB-stacked bilayer graphene at five different locations are illustrated in Fig. 4.8e and 4.8f. The 2D peak features resemble the Raman signature of AB-stacked graphene with average I_{2D}/I_G and FWHM of 0.996 and 48.3, respectively, and fitted with four Lorentzian functions as shown in the inset of Fig. 4.8f. Therefore, the results reveal a uniform graphene film with about 96% AB-stacked coverage based on these Raman features.

Graphene's optical absorptivity has been reported as 2.3±0.1% per layer [3], whereas bilayer graphene's transmittance (AB-stacked) has been measured in previous work as 95.3% at a wavelength of 550 nm [147]. Synthesized graphene at optimized conditions were transferred to a fused silica wafer with $\tau_{quartz} = 0.93$. The measured transmissivity (τ) of SLG shows values between 0.959-0.977, whereas bilayer graphene's transmissivity falls in the range of 0.929-0.953. Some spots have lower values due to high contamination during the wet transfer process and $FeCl_3$/PMMA residuals. The nature of polycrystalline graphene with its grain boundary impairs its electrical and mechanical properties [26].

Studies [13, 25, 142, 147, 150] have been carried out to investigate the electronic transport properties of SLG and AB-stacked graphene, and the sheet resistance has been reported between 0.65-3.4 kΩ/sq, and can reach up to 10^5 Ω/sq [18] with reduced graphene quality. These studies indicate that sheet resistance is largely affected by increased I_D/I_G (graphene boundary defects) and measurement length, leading to increased sheet resistance [18, 25].

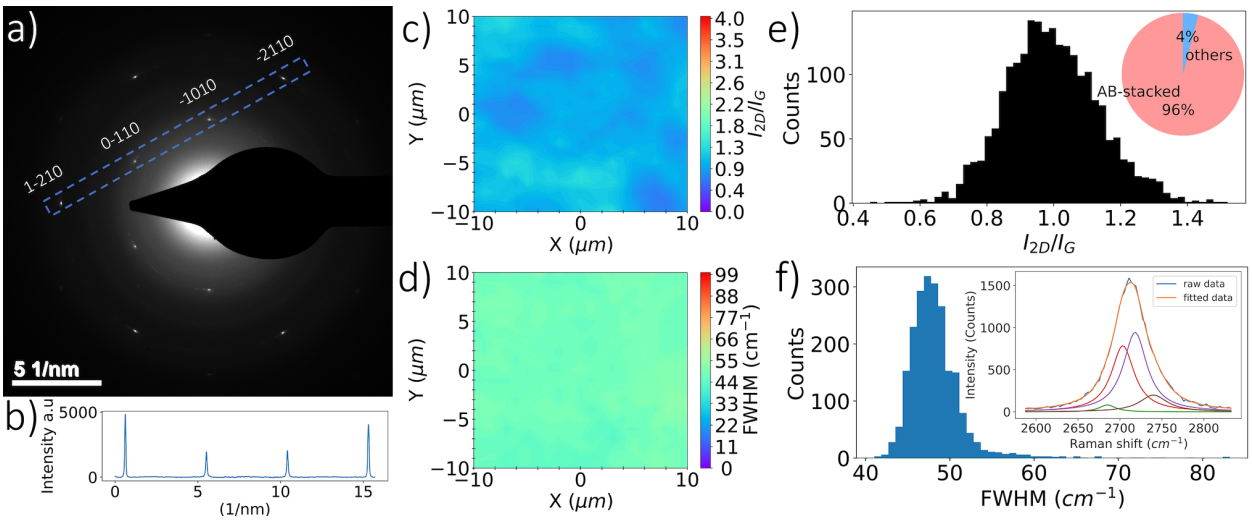

Figure 4.8: AB-stacked bilayer graphene characterization: a) Electron diffraction from a single graphene grain of 20 μm (aperture size). b) Intensity profile within the blue dashed box in part (a) showing outer peaks of equivalent [2100] planes and inner peaks from equivalent [1100] planes. Raman mapping illustrates uniformity of c) I_{2D}/I_G and d) FWHM over a characteristic length of 20 μm acquired from graphene on 300 nm SiO_2/Si. e) Statistical distribution of I_{2D}/I_G, where the inset estimates the stacking ratio of AB-stacked bilayer graphene when compared to other Raman spectra of few-layer graphene. f) Statistical distribution of FWHM, where the inset shows the 2D Lorentzian fit of AB-stacked bilayer graphene.

Table 4.2: Summary of the studied experimental conditions (temperature (T), pressure (P), CH_4:H_2 ration, and time (t)) with averaged I_D/I_G, I_{2D}/I_G, and FWHM from Raman mapping with corresponding sheet resistance measurements.

T (℃)	P (torr)	CH_4:H_2	t (min)	I_D/I_G	I_{2D}/I_G	FWHM (cm^{-1})	R_s (kΩ/sq)	Raman Signature
1016	10	0.25	5	0.62±0.10	-	-	-	-
1038	10	0.25	5	0.53±0.24	-	-	363.62±119.4	-
1050	10	0.25	5	0.19±0.08	1±0.22	47.33±6.06	7.75±3.9	AB-bilayer
1060	10	0.25	5	0.14±0.04	0.98±0.28	47.38±3.68	3.43±1.52	AB-bilayer
1060	5	0.25	5	0.21±0.05	2.3±0.34	38.4±2.2	15.49±4.64	SLG
1060	25	0.25	5	0.64±0.06	-	-	51.7±2.85	-
1060	50	0.25	5	0.68±0.08	-	-	1941.2±1364.3	-
1060	10	0.1	5	0.34±0.14	2.34±0.5	38.09±3.52	9.09±4.2	SLG
1060	10	0.5	5	0.14±0.08	1.5±0.42	48.71±5	1.42±0.18	-
1060	10	1	5	0.19±0.02	0.85±0.1	59.81±4.7	7.98±3.01	-
1060	10	0.25	1	0.47±0.08	1.14±0.26	52.6±3.58	119.22±143.89	AB-bilayer
1060	10	0.25	2	0.25±0.06	1.07±0.32	45.22±4.02	10.04±1.77	AB-bilayer
1060	10	0.25	7.5	0.26±0.06	1.11±0.24	48.35±4.18	11.23±4.73	AB-bilayer

Conversely increased number of layers reduces sheet resistance [18, 142, 150]. Therefore, the sheet resistance provides another indication of graphene quality and number of layers. Here, we report sheet resistance of optimized SLG and AB-Stacked bilayer graphene transferred to thermal oxide wafer with values of 15.49±4.64 and 3.43±1.52 kΩ/sq, respectively, as measured by a 4-point probe with 1 mm spacing. Synthesized graphene at a higher CH_4:H_2 ratio of 0.5 produces lower sheet resistance but with a complex synthesis due to the transient process and non-uniformity in Raman signature and number of layers. Table 4.2 shows the averaged I_D/I_G, I_{2D}/I_G, and FWHM from Raman measurements at different experimental conditions with corresponding sheet resistance.

4.5 Conclusions

This chapter presents a parametric study of graphene growth using a solar-thermal cold-wall CVD reactor to demonstrate the practicality of utilizing a renewable energy resource in synthesizing high-quality graphene films. The design of experiments adopted in this work uses a probabilistic Gaussian regression model and an information acquisition function to quantify the model's information and guide in finding the optimum conditions that minimize the objective function (I_D/I_G). Such synthesis was conducted in a one-step process with a relatively short growth times of 1-10 min. Graphene characterization shows a signature of high-quality SLG and AB-stacked bilayer graphene films through analysis conducted by electron diffraction and Raman mapping with I_D/I_G of 0.21 and 0.14, respectively. Backscattered electron and electron diffraction analysis of SLG and AB-stacked bilayer graphene reveals grain sizes up to 5 and 20 μm, respectively. The transmissivity of SLG and AB-stacked bilayer graphene is measured between 0.959-0.977 and 0.929-0.953, where the sheet resistance

is found to be sensitive to boundary defects with values in the ranges of 15.49±4.64 and 3.43±1.52 kΩ/sq, respectively. The synthesized graphene of this work shows high-quality products and promising capabilities suitable for photonic and electronic applications. Such synthesis of high-quality graphene products can be further scaled up using a roll-to-roll for mass production.

Chapter 5: Scalable graphene production by flattening the heat flux profile: High-quality AB bilayer graphene films by direct solar-thermal chemical vapor deposition

Mass production of graphene by plasma or thermal chemical vapor deposition consumes much energy with potentially adverse effects on the environment. This chapter reports the use of a high-flux solar simulator that approximates the sun's spectrum and a cold-wall chemical vapor deposition reactor to demonstrate a renewable energy process for large-area graphene growth. Synthesis of high-quality ($I_D/I_G = 0.13$) AB-stacked bilayer graphene with greater than 90% coverage is achieved on commercial polycrystalline copper in a one-step process and short time of 5 min. The graphene exhibits large grain sizes up to 20 μm with spatial uniformity over a large area up to 20 mm in radius. The transmissivity and sheet resistance of the graphene films fall in the ranges of 92.8-95.3% and 2-4 kΩ/sq. Thus, direct solar capture provides a compelling option for graphene synthesis that can potentially decrease fabrication costs and environmental pollution.

5.1 Introduction

The dependence of bilayer stacking orientation for graphene, either in AB-stacked or turbostratic form, on the growth regime is even more complicated. Prior studies have reported AB-bilayer graphene growth on polycrystalline copper through a two-step process [12] by synthesizing a top AB layer on a previously grown single layer, where at least 30 min growth

This chapter created the paper by Abdalla Alghfeli and Timothy S. Fisher, "High-quality AB bilayer graphene films by direct solar-thermal chemical vapor deposition", ACS Sustainable Chemistry & Engineering, Under review

time is required to achieve 30-67% AB coverage. Others have adopted low-pressure nucleation and high-pressure growth steps to achieve coverage up to 90% in 3 hours [13]. Single-crystal Cu(111) [29] and Cu/Ni(111) alloy foils [147] enable the synthesis of high AB coverage near 95% in a relatively short time between 2 to 20 min. However, this approach comes at the expense of using costly high-quality single-crystal copper or intricate sample preparation such as polishing and annealing over a 3-7 hour period. Studies [13, 29, 151, 152] have shown that Volmer-Weber growth mode occurs, where presumably the second layer forms beneath the first as carbon radicals intercalate between the substrate and the first graphene layer to produce highly oriented AB-stacking. On the other hand, turbostratic bi-later graphene usually grows atop the first layer at high CH_4:H_2 ratios and generally higher process pressures [29].

According to prior studies [12, 13, 25–30], high temperature, low pressure, and low CH_4:H_2 ratio yield high-quality and uniform graphene films. Additionally, graphene growth at relatively low methane-to-hydrogen ratios and vacuum pressures favors AB-stacked bilayer graphene synthesis [13, 29]. In this chapter, graphene is synthesized at 1060℃, 10 torr, and 1:4 CH_4:H_2 ratio, over a growth time of 5 min based on the findings in chapter 4 that yield a high-quality AB-stacked graphene growth. Here, we demonstrate the use of direct solar capture and flattening the heat flux profile over a large area to synthesize high-quality graphene films with spatial uniformity up to 20 mm in radius and 91% AB-stacked coverage in a fast and a one-step process.

5.2 Experimental Setup

A custom-designed high flux solar simulator (HFSS) that mimics the sun's spectrum and a cold-wall CVD reactor described in chapters 2 and 3 are used here to achieve and demonstrate the feasibility of AB graphene film synthesis by direct solar heating.

By placing a commercial polycrystalline Cu substrate (Revere Copper Products Inc., 76 μm thick C11000 alloy foil), 50.8 mm in diameter, at the optical focal plane, its surface is irradiated by a solar flux with a peak of 1.54 MW/m^2. The substrate is heated and annealed under a hydrogen atmosphere prior to graphene growth, and a single-wavelength (5 μm) pyrometer (Williamson, SP-GL-20C) calibrated to the melting point of copper is used to measure its temperature (an average value within a circular diameter of 3.8 mm). The copper substrate reaches a constant temperature of 1060℃ within a circular area of a 6 mm radius in 15 min. Enlargement of the peak heating area can be achieved by displacing the lamp 4.8 mm towards the target (Z-axis shown in Fig. 5.1), out of its focal plane, where the heat flux on the sample is flattened to produce a more uniform profile. Consequently, a larger area on the copper substrate with a circular area of a 20 mm radius achieves a more spatially uniform temperature of 1060℃ $\pm$ 10℃, by increasing the total power emitted by the HFSS.

5.3 Results and discussion

Graphene synthesized with the on-focal-point bulb position was characterized initially according to grain size, lattice structure, and number of layers/orientations. First, backscattered electron (BSE) images acquired from graphene grown on Cu indicate large preferential graphene growth characteristic size within certain crystallographic orientations of Cu [43] of

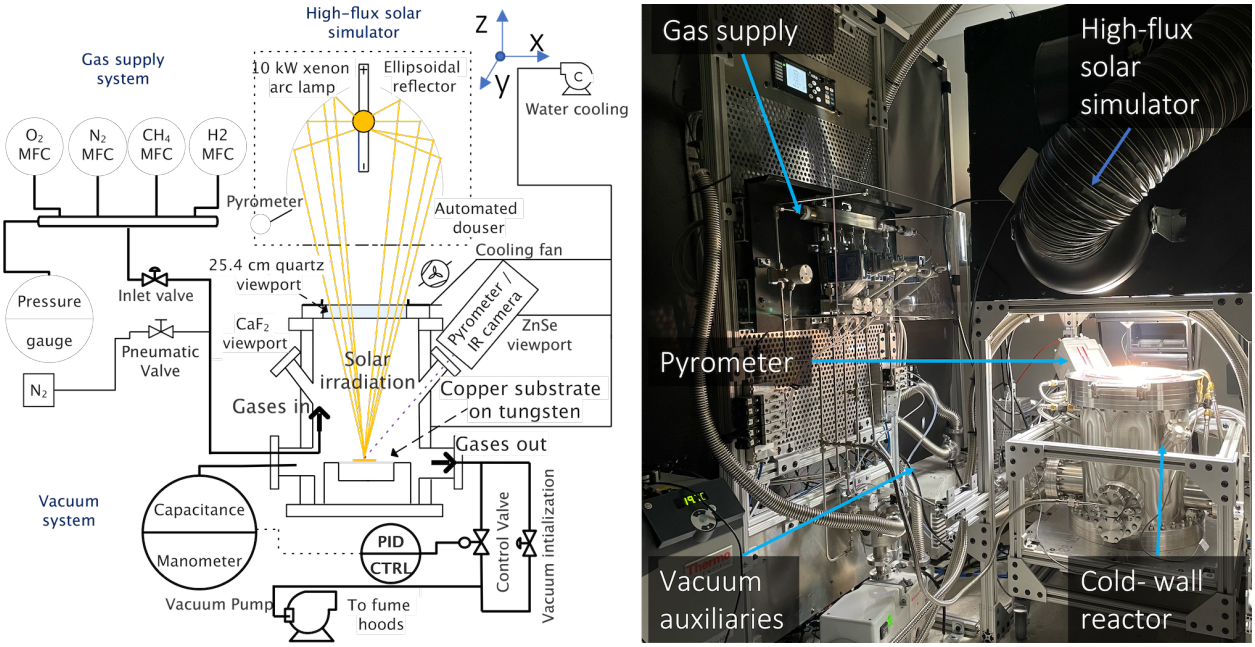

Figure 5.1: Overview of the solar-thermal CVD setup for graphene synthesis.

at least 20 μm with merged and smooth boundaries as shown in Fig. 5.2a and 5.2b under high and low magnifications, respectively. Graphene was then transferred to a transmission electron microscope (TEM) grid to assess the lattice structure by electron diffraction. Electron diffraction reveals different patterns from single-grain to polycrystalline graphene due to various grain sizes [144]. Prior studies have indicated that synthesis on polycrystalline Cu, which exhibits irregular surface roughness and grain boundaries, affects the density and shape of graphene nuclei, and thus grain size and boundary structure [26].

A single grain domain was used to study the features of synthesized graphene thoroughly, as illustrated in Fig. 5.2c. The hexagonal lattice pattern of graphene from electron diffraction shows plane spacings d_{11} and d_{10} of 0.12, and 0.21 nm, respectively, with $d_{10}/d_{11} = \sqrt{3}$. Therefore, the lattice constant for graphene is estimated as $\tilde{a} = 0.14$ nm. A dark-field image from scattered electrons was used to identify grain size by electron diffraction, estimated

as 20 μm as shown in Fig. 5.2d. Additionally, diffraction intensities from outer peaks of equivalent planes [2100] over inner peaks from equivalent planes [1100] labeled by Bravis-Miller indices (I_{1-210}/I_{0-110} and I_{-2110}/I_{-1010}) as shown in Fig. 5.2c and 5.2d are close to 0.5 for monolayer graphene and 2 for AB-stacked bilayer graphene [12, 13, 147]. Here, we report diffraction intensity ratios near 2 after baseline subtraction as shown in Fig. 5.2c and 5.2d, indicating the formation of AB-stacked bilayer graphene.

As discussed above, the graphene growth area was increased by displacing the lamp bulb to flatten the heat flux profile, achieving a uniform temperature near 1060℃ on a larger area and leading to an increased growth area of an order of magnitude with the same growth time. In general, this modification demonstrates that temperature magnitude and uniformity are paramount in the overall efficacy of the process. The resulting graphene films were transferred to fused silica and Si/SiO_2 wafers as illustrated in Fig. 5.2e and 5.2f. The morphology of graphene on fused silica was studied using optical and scanning electron microscopy (SEM) as shown in Fig. 5.2e and 5.2g, respectively, to illustrate film uniformity without apparent contrast, which would otherwise exist due to variations in absorption associated with different numbers of layers.

Raman mapping was conducted for graphene on SiO_2/Si to quantify the coverage of AB-stacked graphene statistically. Figs. 5.3a, 5.3b, and 5.3c show Raman maps of I_D/I_G, I_{2D}/I_G, and FWHM, respectively, carried out on a square area with 200 and 20 μm characteristic lengths. Raman analysis indicates a high percentage of AB-stacked bilayer spectra with minor SLG and few-layer signatures, as illustrated in the inset of Fig. 5.3d. The Raman spectrum of AB-stacked bilayer graphene displays distinctive features; the 2D peak is asymmetric, with FWMH and I_{2D}/I_G values in the ranges of 40-62 cm^{-1} and 0.75-1.46, re-

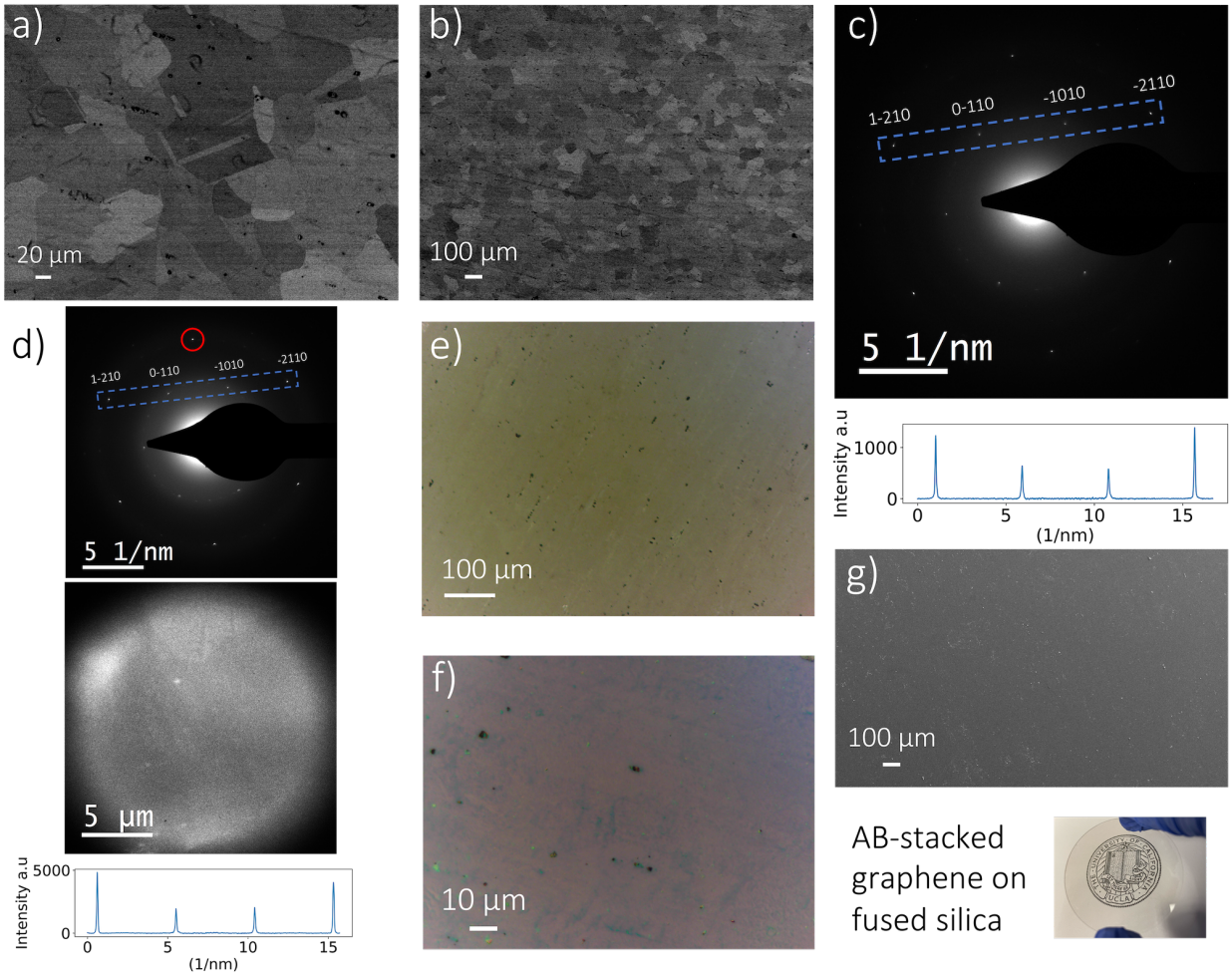

Figure 5.2: BSE image of graphene grown on copper with the source bulb on the focal point, indicating characteristic sizes of at least 20 μm with a) high and b) low magnification. c) Electron diffraction from a single grain of graphene with intensity profiles within the blue dashed box that show outer peaks of equivalent [2100] planes and inner peaks from equivalent [1100] planes. d) Dark-field image to identify grain sizes by electron diffraction up to 20 μm (aperture size). Optical micrograph of graphene grown with a displaced bulb setting on e) fused silica and f) Si/SiO_2. g) SEM image of graphene film transferred to fused silica that shows film uniformity without an apparent contrast.

spectively [12, 13, 147]. Additionally, AB-stacked graphene's electronic structure is uniquely captured by the Raman results. A double-resonant Raman process due to changes in electronic band structure occurs, and the 2D peak splits into four components with known peak locations for different excitation energies [149, 153].

Here, we observe 2D peak features consistent with AB-stacked graphene, with I_{2D}/I_G and FWHM of 1.0 and 50 cm^{-1}, respectively, fitted with four Lorentzian peaks centered at 2682, 2700, 2715, and 2734 cm^{-1} as shown in Fig. 5.3e. The distributions of I_D/I_G, FWHM, and I_{2D}/I_G from Raman mapping at five different locations illustrated in Fig. 5.3d, 5.3e, and 5.3f, respectively, reveal a nearly uniform graphene film with 91% AB-stacked bilayer coverage and an average I_D/I_G of 0.11. Additionally, Raman measurements indicate spatial consistency up to 20 mm in radius from measurements averaged radially as shown in Fig. 5.4a and 5.4b, with average I_D/I_G and I_{2D}/I_G ratios of 0.13 and 0.94, respectively.

Graphene's opacity has been previously reported as 2.3±0.1% per layer [3], and the optical transmittance through AB bilayer graphene has been found to be 95.3% at 550 nm [147]. In this work, the measured transmissivity (τ) of the large-area graphene film transferred to a fused silica wafer ($\tau_{fused\ silica} = 0.93$) falls between 0.928 and 0.953, as shown in Fig. 5.4a, indicative of bilayer graphene with minor contamination. However, some spots exhibit lower transmissivity, which is mainly attributed to contamination during the wet transfer process, polymer and etchant residuals, and the effect of fused silica transmissivity. Even though graphene quality is reduced at the edge of the uniform area, its transmissivity has higher values (0.960-0.97.7), which might be attributed to a prevalence of monolayer graphene.

Polycrystalline graphene's grain boundaries induce defects that can impair its electrical and mechanical properties [26]. Prior studies [13, 147] have been conducted on electronic

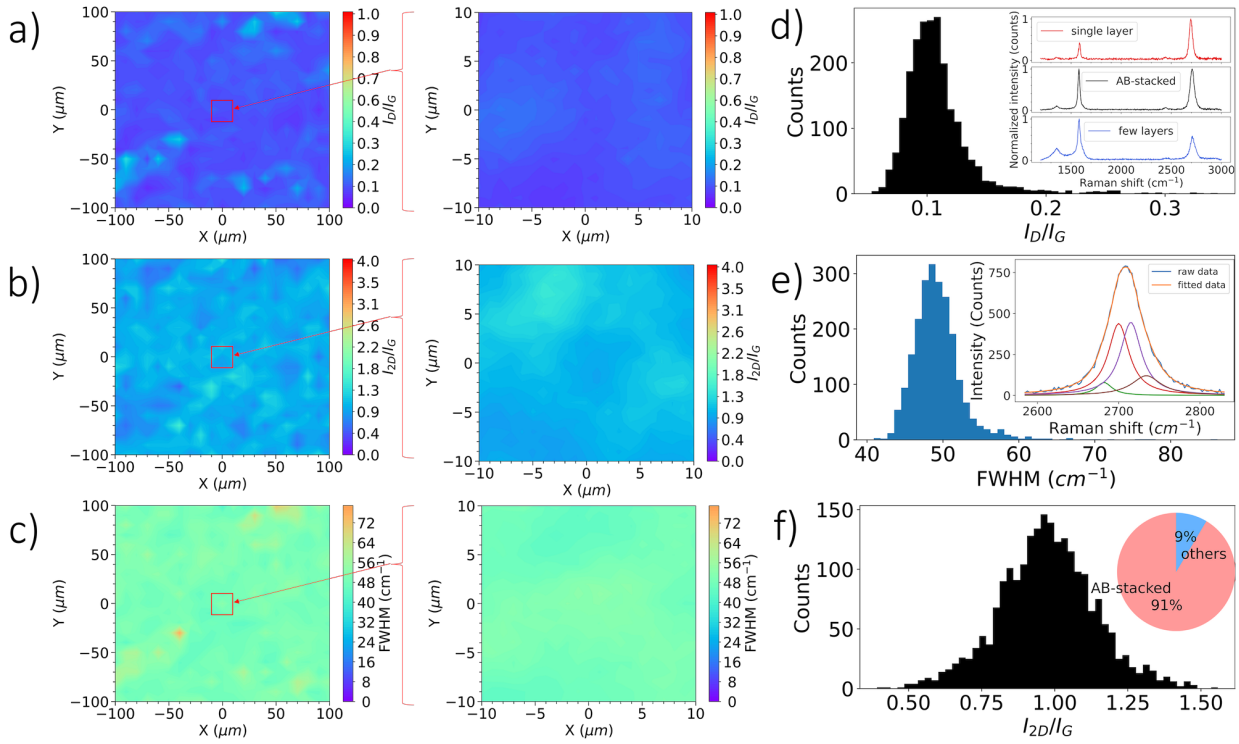

Figure 5.3: Raman mapping of graphene grown with the source bulb displaced from the focal point (to flatten the light intensity distribution) on 300 nm SiO_2/Si shows uniformity of a) I_D/I_G, b) I_{2D}/I_G, and c) FWHM over characteristic lengths of 200 (left) and 20 μm (right). d) Raman spectra acquired for graphene with AB-stacked, SLG, and few-layer signatures. e) Statistical distribution of FWHM, where the inset shows the 2D Lorentzian fit of AB-stacked bilayer graphene. f) Statistical distribution of I_{2D}/I_G, where the inset estimates the stacking ratio of AB-bilayer when compared to other Raman spectra of SLG or few-layer graphene.

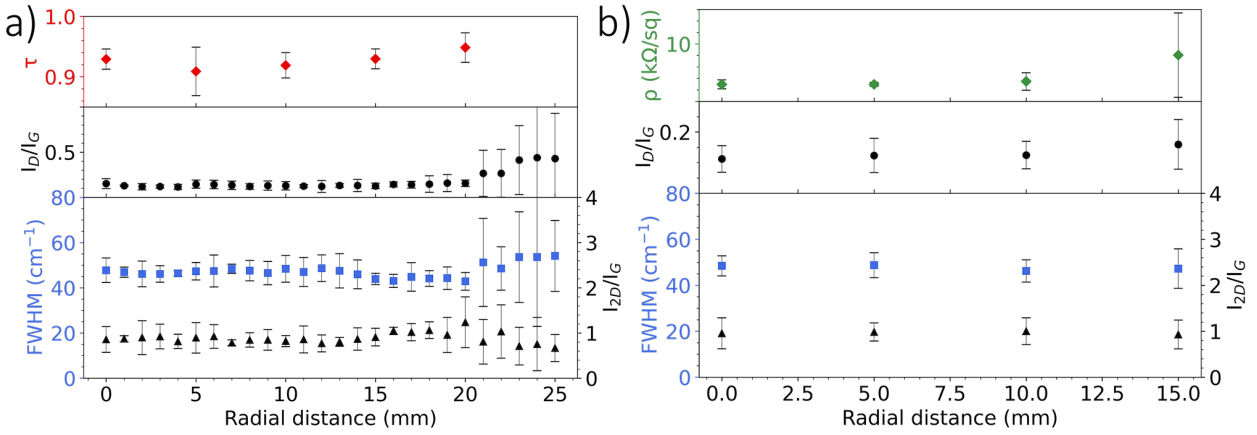

Figure 5.4: a) Transmissivity of synthesized graphene transferred to fused silica with co-located Raman measurements (I_D/I_G, I_{2D}/I_G, and FWHM) as a function of radial position, where error bars show the uncertainty of radial measurements at different angular positions (0°, 90°, 180°, and 270°). b) Sheet resistance of synthesized graphene transferred to thermal oxides with co-located Raman measurements (I_D/I_G, I_{2D}/I_G, and FWHM) as a function of radial position, where error bars show the uncertainties of radial measurements at eight different angular positions (0°, 45°, 90°, 135°, 180°, 225°, 270°, and 315°).

transport properties of AB-stacked graphene by fabricating field effect transistor devices. At zero gate voltage, such measurements give sheet resistance in the range of 2.2-3.4 kΩ in a square channel [13, 147]. Others have also reported sheet resistance values as high as 9 kΩ/sq [12] with lower AB-stacked coverage. The sheet resistance of graphene transferred to SiO_2/Si here generally falls between 2 and 4 kΩ/sq, as illustrated in Fig. 5.4b. Other factors can also impact the sheet resistance measurements, such as contamination from the etching process ($FeCl_3$), copper/polymer residuals, and the effects of thermal oxide.

Progress in sustainable manufacturing and chemistry benefits from intentional assessment of sustainability metrics and adverse effects on the environment [154, 155]. Methane decomposition into graphene follows the chemical reaction: $CH_4 \rightarrow C + 2H_2$ with an en-

thalpy of dissociation of $\Delta H^o = 74.6$ kJ/mol$_{CH4}$. Here, the molar deposition rate of bilayer graphene on a circular area of 40 mm diameter during 5 minutes is $\dot{n_C} = 2\rho_{2D}A_s/M_C t$, where A_s is the surface deposition area, $M_C = 12.011$ g/mol is carbon molar weight, and t is time. The surface density of graphene is $\rho_{2D} = 2m_{carbon}/A = 76.26 \times 10^{-8}$ kg/m^2 as two carbon atoms occupy a hexagonal area (graphene unit cell) with C-C length of $l = 0.142$ nm. Thus, the efficiency of the reaction is $\varepsilon = \dot{n_C}\Delta H^o/\dot{Q_{in}} \approx 1{\times}10^{-6}\%$, with a solar simulator power input ($\dot{Q_{in}}$) in the 1.5-2.5 kW range, depending on the location of the lamp with respect to the reflector focal point. Additionally, the atomic efficiency (AE), the ratio of molecular weight of products (M_P) to total molecular weight of reactants (M_R), is AE = M_P/M_R x 100 = 74.9%. The reaction mass efficiency (RME), which is the ratio of the mass of isolated product ($m_{graphene}$) to total mass of reactants (m_R), is RME = $m_{graphene}/m_R$ x 100, where $m_{graphene} = 2\rho_{2D}A_s$ and $m_R = \dot{V}\rho_{CH_4}t$ ($\dot{V} = 25$ sccm). Therefore, the RME is approx. $2{\times}10^{-5}\%$, and the overall efficiency (OE) is OE = RME/AE x 100 $\approx 3{\times}10^{-5}\%$. We recognize that the sustainability metrics for this initial report of a new process are quite low. On the other hand, the use of direct solar input in this process obviates the need for electric grid power other than for ancillary gas flow and process control equipment. We also recognize that substantial improvements would be possible by: (a) recycling process gases instead of exhausting them, (b) increasing process throughput, and (c) adding thermal loss containment measures such as radiation shielding and insulation.

5.4 Conclusions

In conclusion, a custom solar-thermal cold-wall CVD process demonstrates the feasibility of utilizing a renewable energy resource in synthesizing high-quality graphene films. Graphene

synthesis was conducted in a one-step process over a relatively short growth time of 5 min. The graphene exhibits clear signatures of high-quality, polycrystalline, and AB-stacked bilayer graphene films through electron diffraction and Raman mapping analysis. Backscattered electron and electron diffraction images indicate large grain sizes up to 20 μm, and Raman measurements demonstrate spatial uniformity up to 20 mm in radius with $I_D/I_G = 0.13$. The measured film's transmissivity and sheet resistance are 0.928-0.953 and 2-4 kΩ/sq, respectively. The high-quality graphene films in this work show promising capabilities suitable for transparent conducting electrodes. Additional studies on applications such as a field-effect transistor device are expected to characterize the functionality of the synthesized AB-bilayer graphene from this work.

Chapter 6: Scalable graphene production by roll-to-roll solar-thermal chemical vapor deposition

Mass production of graphene is necessary to maximize the impact of graphene's remarkable properties. This chapter reports the use of a roll-to-roll mechanism with solar-thermal chemical vapor deposition to scale-up graphene growth and enable green manufacturing. A study of graphene's growth parameters has been carried out, leading to the synthesis of moderate-quality (I_D/I_G of 0.7) graphene films at a speed of 200 mm/min with at least 72% single-layer coverage suitable for transparent conductive electrodes. Additionally, the graphene synthesized in this work can be applied as an oxidation barrier for metals. The foil's upstream temperature is maintained close to the reported limits of graphene nucleation in thermal deposition techniques, and surface polishing removes low-quality graphene prior to the deposition zone. Even though attempts show domains of high-quality graphene, uniformity has yet to be achieved; hence, design modification to eliminate carbon deposition before the reaction zone is warranted.

6.1 Introduction

To exploit graphene's extraordinary properties, a need exists to develop scalable methodologies that enable various large-scale applications from photonic and electronic devices [4, 5, 7, 12, 13, 32, 33, 35, 36, 112] to supercapacitors [8–10] and batteries [10, 11]. Graphene production and scale-up processes usually involve complex and costly operations. These processes include the synthesis of graphene by graphite exfoliation or growth by chemical

vapor deposition, as well as transferring graphene to arbitrary substrates. Many have studied large-scale graphene production through graphite exfoliation [14, 15]. Monolayer graphene is produced by dispersion and exfoliation of graphite in N-methl-pyrrolidone (NMP), an organic solvent, with concentrations up to 0.01 mg/ml [14]. The energy required to exfoliate graphene by overcoming the van der Waals bond derives from the chemical interreaction between the solvent and graphene. Others have utilized high-shear mixing in a stabilizing liquid (NMP, sodium cholate, and NaC) to achieve dispersions of graphene nanosheets up to hundreds of liters [15] under local shear rate above 10^4 s^{-1}.

Mass graphene production by roll-to-roll CVD is a promising mechanism to meet industrial needs. Studies have been carried out on plasma [17, 18, 156, 157] and thermal [158, 159] heating sources. Yamada et al. demonstrated graphene synthesis by surface wave plasma (SWP) CVD at low temperature and pressure, around 300℃ and 30-300Pa, respectively, on Cu foils [18]. Synthesized graphene on Cu foil with 297 mm width showed uniformity in optical transparency and sheet resistance of 95% and 7×10^5 Ω/sq [18, 157], respectively, making it applicable as a transparent conductive electrode. The ability to synthesize graphene on aluminum, a noncatalytic material to carbon decomposition, was further demonstrated [18, 157]. Additionally, Yamada et al. studied the effect of controlling the process pressure and $CH_4/(CH_4+H_2)$ on graphene synthesis, where low pressure 30 Pa and 50% concentration yield lower D-peak intensity and uniform Raman measurements across the A4 page size width [156]. Graphene coating by a roll-to-roll SWP CVD mechanism has also been investigated to provide oxidization-resistant films at low temperatures around 450℃ [42]. Process optimization of graphene growth by plasma roll-to-roll CVD has been carried out by Alrefae et al. [17], where the optimized design parameters show $I_D/I_G = 0.7$ with scalable pro-

duction at 1 m/min web speed. In-process monitoring has also been implemented in some studies, where radical emission lines were correlated to graphene quality [17].

Others have utilized electric heating to investigate the mass production of graphene by roll-to-roll CVD. Few-layer graphene has been synthesized at atmospheric pressure with roll-to-roll hot tube furnace CVD, where characterization tools show continuous graphene, enabling low-cost fabrication [158]. However, most graphene synthesis is favored at low pressure to eliminate the effects of boundary layers on the growth of nonuniform films [27]. Kobayashi et al. [159] demonstrated graphene synthesis on Cu at low pressures with roll-to-roll Joule heating CVD and a direct transfer process using photocurable epoxy resin. As a result, graphene synthesis of 100 m length was confirmed with high-quality Raman and SEM signatures and low sheet resistance of 150 Ω/sq, applicable as transparent conductive films [159]. Concentric tube (CT) CVD synthesis of graphene on a helically wrapped flexible substrate around the inner tube has been achieved, where carbon-containing feedstock is introduced from the outer tube at the reaction zone, thereby, separating the reactor into annealing and growth zones [160]. The effects of temperature (1000-1045℃) and web speed (25-500 mm/min) variations while keeping pressure and C_2H_4/H_2 ratio at 4 torr and 10/315 sccm, respectively, was investigated. The method enables the synthesis of high-quality monolayer graphene at 25 mm/min [160]. Kidambi et al. [43] extended the work on roll-to-roll CT-CVD to synthesize large-area graphene combined with casting of a porous polymer, where the effect of CH_4/H_2 ratio, web speed, and carbon precursor in the annealing zone on graphene quality were studied. The results show high-quality monolayer graphene with $I_D/I_G \leq 0.065$ at speeds above 5 cm/min. Also, the size-selective molecular transport sep-

aration demonstrates applicability of graphene as nanoporous atomically thin membranes [43].

Numerical and analytical heat transfer studies of a continuously moving surface are of growing interest, especially in scaled-up manufacturing applications such as casting, extrusions, and hot rolling, as well as crystal growth [161]. Karwe et al. studied the thermal transport of a continuously heated body by coupling the heat transfer in the moving material and fluid transport. Most studies use similarity transformations [161, 162] and finite difference methods [161], and results are obtained as a function of Peclet number (Pe) and the properties of the fluid and the material [161]. Others have adopted a cubic spline numerical method [163] and integral momentum equations [164] to solve for conjugate heat transfer in the laminar boundary layer of a moving flat surface [162–164], where some extended the work to turbulent flow [162, 164]. In solving these heat transfer problems, conductive effects in the upstream location from the flat surface emergence are significant [165]. Additionally, analysis of vertically moving surfaces has been investigated, where thermal buoyancy was found to substantially affect the thermal distribution compared to the horizontal orientation [165, 166]. Heat transfer modeling of moving surfaces in material deposition and thermal processing using either plasma [167, 168] or Joule heating [169] has been carried out and validated with experimental results.

In this work, the solar-thermal CVD system developed earlier has been further modified to accommodate higher production of graphene through a roll-to-roll mechanism. Synthesis of graphene at various conditions has been carried out, where high temperatures and low pressures have been reported to yield higher graphene quality [43, 159, 160]. The growth of low-quality graphene upstream of the focal point and at low temperatures [18, 43, 156,

157] has been found to hinder achieving high-quality films. As such, CH_4/H_2 and web speed parameters significantly impact roll-to-roll graphene quality [43]. Here, we try to optimize the CH_4/H_2 ratio and web speed for graphene synthesis. Additionally, design modifications have been implemented to lower the temperature of the upstream foil below graphene nucleation limits [44] by increasing conduction heat transfer, as well as polishing the foil to remove deposited low-quality graphene prior to the growth zone.

6.2 Experimental Setup

6.2.1 Roll-to-toll solar-thermal CVD system

The solar-thermal CVD system described in chapter 3 was further modified to accommodate roll-to-roll graphene synthesis for mass production. Two stepper motors with 870 in-oz holding torques (Lin Engineering, Inc., 8718M series), stepper drives (Geckodrive, Inc., G210X), solid shaft ferromagnetic fluid rotary feedthrough (KJLC Co., KLFDCF), roller bearings, shaft couplings, right angle gearboxes, and solid and flexible shafts are utilized. The roll-to-roll assembly is a custom-designed fixture fabricated by water jet from 316 stainless steel sheets, threaded rods, and fasteners. Fig. 6.1 shows an overview of the roll-to-roll solar-thermal CVD setup alongside the system's main components.

6.2.2 Characterization instruments

Raman and SEM characterization tools explained in chapter 4 are used here. Using emission spectroscopy [170], the copper foil temperature was measured from the bottom surface as shown in Fig. 6.1. An imaging spectrometer described in chapter 3 is employed to acquire the emission spectrum of a heated copper foil, where a 1200 gr/mm blazed holographic grating is used to cover the spectral range from 400 to 1200 nm. Since radiation intensity as a function

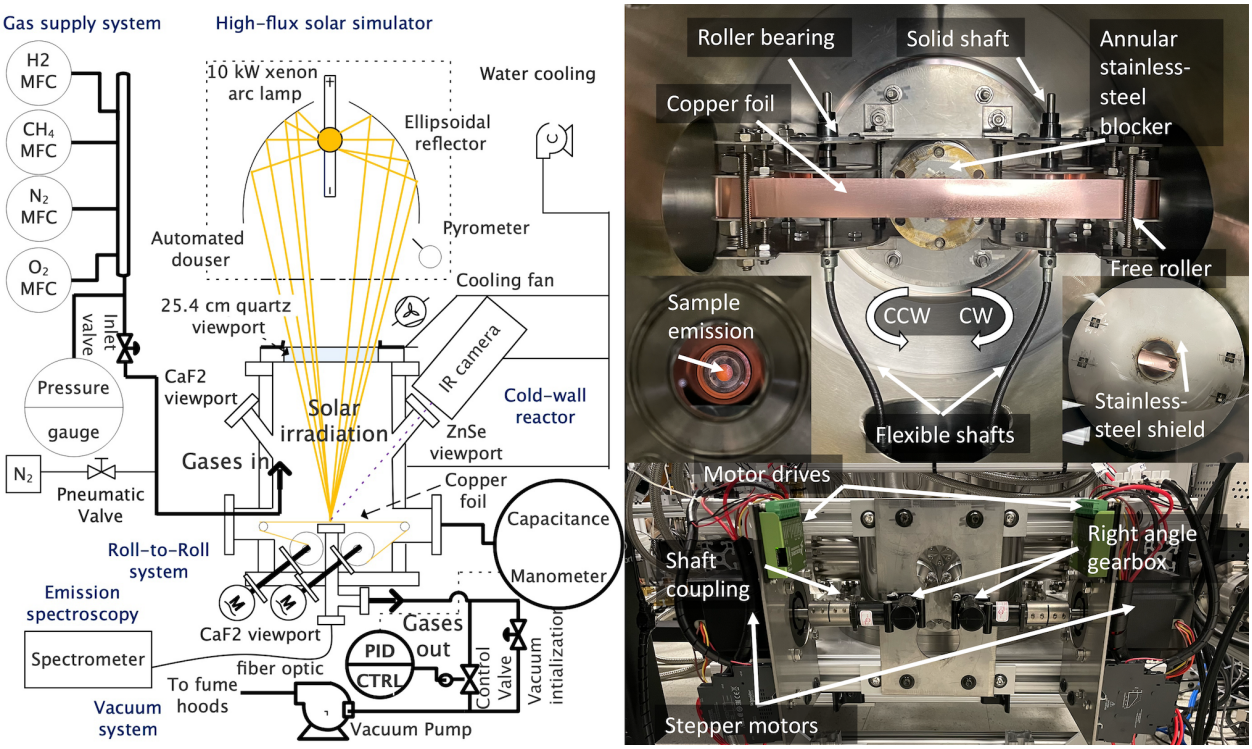

Figure 6.1: Overview of the roll-to-roll solar-thermal CVD system used in graphene synthesis.

wavelength is crucial in accurate temperature measurements, the spectrometer and grating have been calibrated using a single wavelength, 532 nm, laser. Radiative emission from the copper foil is collected and collimated by focusing lenses and directed into the spectrometer entrance slit by a fiber optic cable. Thus, the emission intensity from the copper foil (I) illustrated in Fig. 6.2 can be fitted to Planck's distribution [120] as a function of wavelength (λ) and temperature (T) within the spectral range of 700-800 nm:

$$E_{\lambda,b}(\lambda,T) = \frac{C_1}{\lambda^5[\exp\left(C_2/\lambda T\right)-1]} \tag{6.1}$$

$$I(\lambda,T) = A\epsilon(\lambda)E_{\lambda,b}(\lambda,T) \tag{6.2}$$

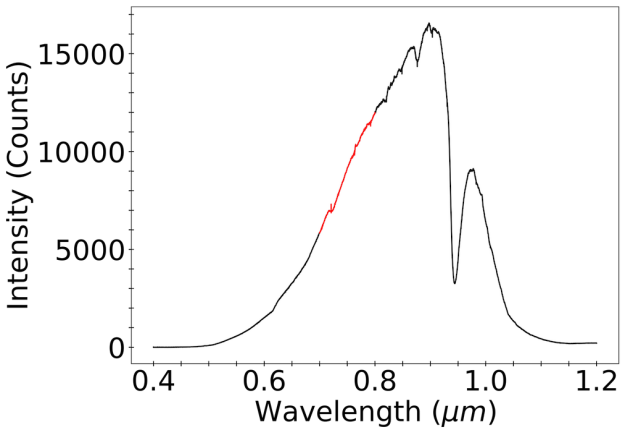

Figure 6.2: The emission spectrum of a heated copper foil onset of melting used for measurement calibration.

where $C_1 = 2\pi hc_o^2 = 3.742 \times 10^8$ W $\cdot\, \mu$m^4/m^2 and $C_2 = (hc_o/k_B) = 1.439 \times 10^4 \mu$m $\cdot$ K. A is calibrated based on the emission spectrum of the copper foil's onset of melting (T $\approx$ 1080℃) and emissivty [125, 171, 172] at a wavelength of 750 nm. The IR camera (FLIR A655sc) described in chapter 3 is also used here for temperature measurements.

6.2.3 Experimental procedure

Using solar-thermal chemical vapor deposition, roll-to-roll graphene synthesis was carried out on a polycrystalline copper foil (United States Brass & Copper Co.) with 99.9% purity. First, a long copper foil (2.54 cm in width and 75 μm thick) was cleaned with acetone. The copper foil was then loaded into the roll-to-roll fixture and inserted into the reactor, where it was leveled to the target focal plane. Vacuum was then initiated for 10 min to achieve a low pressure of approx. 10^{-3} torr. Based on the process pressure, the reactor was filled for 5 min with H_2 gas at a flow rate of 1000 sccm. The HFSS was powered on; ramping up to achieve a steady optical output in 15 min [38] is necessary before any synthesis. During ramp-up, copper foil movement was initiated for 15 min by rotating the motors clockwise (CW) at

a web speed of 5 mm/min under H_2 flow of 1000 sccm. Afterward, the copper foil was annealed for 15 min with counterclockwise (CCW) movement at 5 mm/min under H_2 flow of 100 sccm. After annealing the 75 mm strip, the copper foil was allowed to continue rolling and annealing in the same direction with a fast pace corresponding to the experimental web speed and HFSS settings.

Allowing the studied strip to go far away from the focal point (distances vary from 400 to 1600 mm with speed) is essential to ensure the reactor conditions reach equilibrium before any synthesis. Graphene synthesis was established by flipping the rolling direction to CW and introducing methane at a CH_4:H_2 gas flow ratio based on the design parameter with hydrogen flowing at 100 sccm. The emission spectrum of the copper foil was acquired by a spectrometer during the fast annealing and synthesis processes.

Once graphene growth was accomplished, the HFSS was powered off, and the roll movement was stopped. The sample was allowed to cool under a hydrogen atmosphere before removal from the reactor with the following setpoint: a) 25 torr with a flow rate of 100 sccm for 15 min, followed by b) 100 torr with a flow rate of 1000 sccm for 15 min. The process design parameters with their limits are illustrated in Table 6.1, where constraints on gas composition are: $H_2(\%) + CH_4(\%) = 100\%$.

6.3 Results and discussion

6.3.1 Characterization of different conditions

A probabilistic surrogate model described in chapter 4 is adopted here to fit I_D/I_G and I_{2D}/I_G as functions of the process parameters and to predict other conditions based on information available within the data. Raman measurements used in this model were acquired

Table 6.1: Process design parameters with their limits for roll-to-roll graphene synthesis.

Parameters	Lower limit	Upper limit
Temperature (℃)	900	1075
Pressure (Torr)	2	15
Methane (CH_4)	10%	50%
Hydrogen (H_2)	50%	90%
web speed (mm/min)	5	400
HFSS current (A)	98	124

directly from graphene on copper for ease of time by averaging the results from five points. The objective function I_D/I_G and I_{2D}/I_G from the surrogate regression model are shown in Fig. 6.3 as a function of a) temperature, b) pressure, c) CH_4:H_2 ratio, and d) web speed, where one parameter is varied while others are held constant. BSE images and Raman spectra of graphene on Cu were used to assess the effects of different conditions on graphene quality, uniformity, and preferential graphene growth characteristic size within certain crystallographic orientations of Cu [43]. Graphene roll-to-roll synthesis was carried out with the xenon arc lamp placed at the focal point of a truncated ellipsoidal reflector, and the copper foil leveled to the target focal plane, where the heat flux is most concentrated. Roll-to-roll graphene synthesis on a thermally conductive substrate such as copper enables low-quality film growth upstream to the focal point at lower temperatures. Thus, the effect of different conditions, specifically, CH_4:H_2 and web speed are crucial to graphene quality [43, 160], and both I_D/I_G ratio and 2D peak characteristics are investigated here.

Generally, high temperatures improve graphene quality, favor the growth of single layer [26, 30], and promote the appearance of a 2D peak in the Raman spectrum as illustrated in Fig. 6.3a and 6.4a. As discussed in chapter 4, graphene nucleation density is a temperature-dependent phenomenon with activation energy between 1 and 3 eV [26, 30]. During the

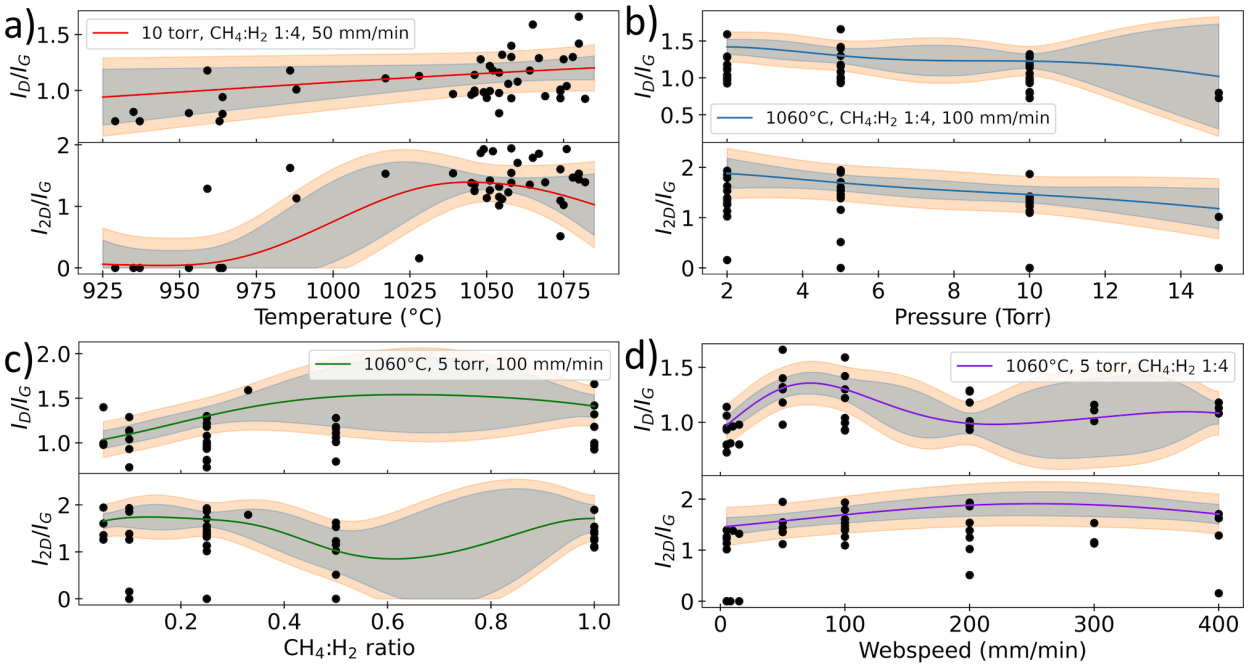

Figure 6.3: The objective function I_D/I_G and I_{2D}/I_G from the surrogate regression model as a function of a) temperature (℃), b) pressure (torr), c) CH_4:H_2 ratio, and d) web speed (mm/min), where one parameter is varied while others are held constant. *Note: Not all experimental points belong to these spaces but only share the main x and y-axis due to the projection of 5-dimensional space onto a 2-dimensional plot.

decomposition of methane facilitated by higher temperature [25], supersaturated active carbon species near the copper surface reach a concentration that enables graphene nucleation [30]. When graphene nucleation occurs, the concentration drops to the growth level, where consumed carbon atoms during graphene growth create a difference in carbon concentration (ΔC). The difference in concentration is higher at low temperatures, enabling the growth of few-layer graphene [26, 30]. High temperatures also favor captured supercritical carbon to enlarge the grain size over establishing new nucleation on newly available sites due to increased desorption [26]. Fig. 6.4a shows BSE images and Raman spectra of graphene synthesized at 964 and 1069℃, respectively, while other parameters are held at 10 torr, CH_4:H_2 1:4, and 50 mm/min. Raman analysis shows a dominant nanocrystalline graphene signature [41] at low temperature (964℃), with probably few layers, an average I_D/I_G of 0.95 with likely small grain sizes due to increased nucleation density [26], and various characteristic sizes from the BSE image of graphene on Cu. Conversely, graphene growth at higher temperatures (1069℃) shows a 2D peak with similar characteristic sizes. At 1069℃, the defects are quantified with an average I_D/I_G of 0.95, and the 2D peak is prominent with an average I_{2D}/I_G of 1.40.

Low pressure [43, 160] favors the growth of a single graphene layer, as shown in Fig. 6.3b, where the $I_{2D}/I_G \approx 2$. Factors such as geometry, reactor flow, and pressure play essential roles in graphene thickness and uniformity [27]. The boundary layer effect is negligible at low pressures, and growth is governed by the surface reaction regime, which is highly sensitive to temperature. Accordingly, fewer collisions and reduced active species flux occur at low pressure, enhancing the diffusion through the boundary layer [27]. By increasing the pressure in graphene synthesis, diffusion through the boundary layer becomes the limiting

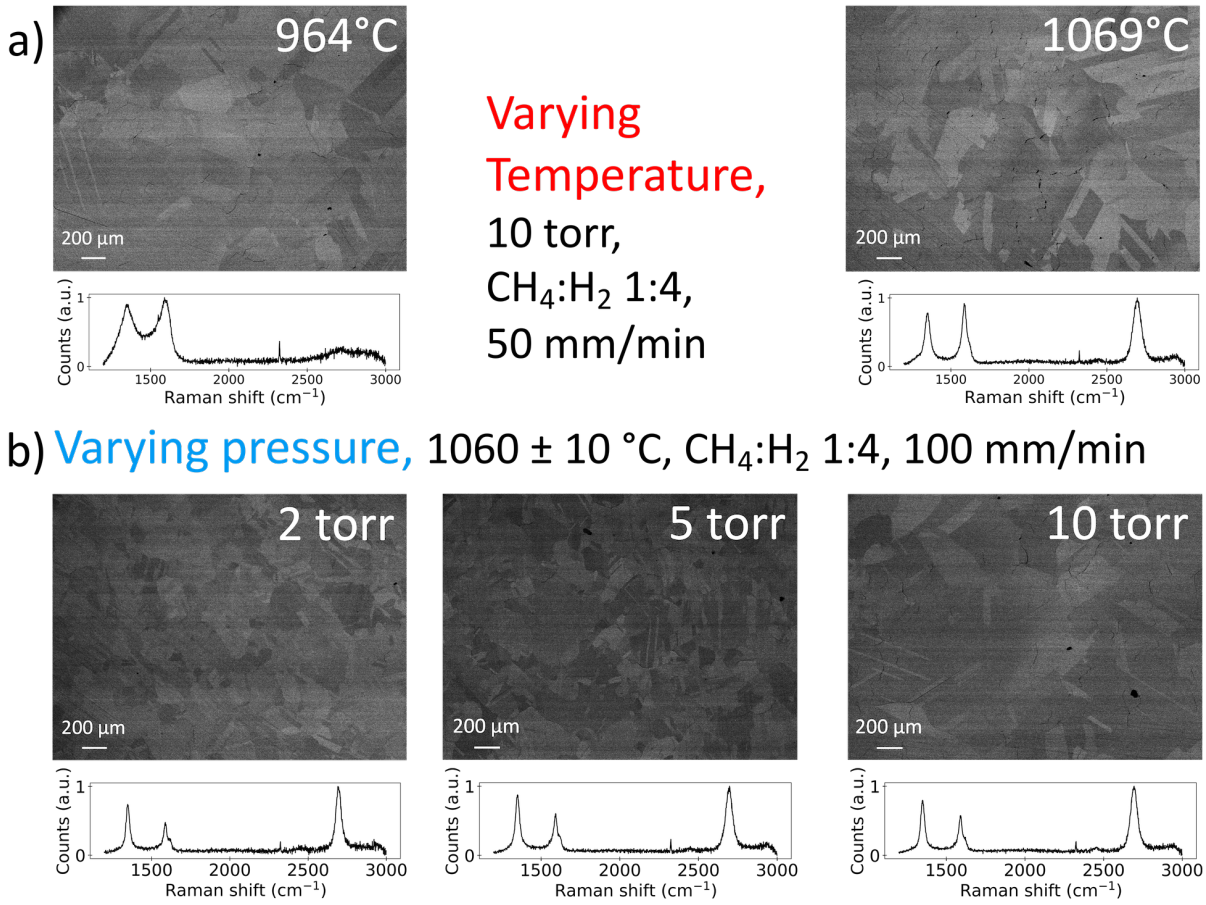

Figure 6.4: BSE images and Raman spectra that show characteristic sizes and graphene quality from Raman measurements (I_D/I_G) synthesized at different a) temperatures of 964 and 1069°C, while other parameters are held at 10 torr, CH_4:H_2 1:4, and 50 mm/min, and b) pressures of 2, 5, and 10 torr, while other parameters are held at 1060°C, CH_4:H_2 1:4, and 100 mm/min.

factor, leading to a non-uniform BL and, therefore, film thicknesses [27]. Fig. 6.4b shows BSE images and Raman spectra of graphene synthesized at relatively low pressures of 2, 5, 10 torr, respectively, while other parameters are held at 1060℃, CH_4:H_2 1:4, and 100 mm/min. At 2, 5, and 10 torr, graphene shows slight improvements in quality and an increase in thickness with pressure indicated by the decrease in I_{2D}/I_G as shown in Fig. 6.3b with average I_D/I_G of 1.59, 1.30, and 1.22, and I_{2D}/I_G of 1.79, 1.47, and 1.42, respectively. Additionally, BSE images show that characteristic sizes are improved with increased pressure in the 2-10 torr range, as shown in Fig. 6.4b.

Hydrogen has a double role as a facilitator for methane chemisorption by activating surface-bound carbon and an etching reagent that controls the size and morphology of graphene grains [28]. Hydrogen also counteracts the negative impact of stray oxidizing contaminants in the gas feed and the copper foil during the synthesis [28]. Additionally, the decrease in methane partial pressure (concentration) leads to a lower nucleation density [26]. Fig. 6.5a illustrates BSE images and Raman spectra of graphene synthesized at 0.1, 0.25, and 1, respectively, while other parameters are held at 1060℃, 5 torr, and 100 mm/min. Results show improvement of graphene quality with increased CH_4:H_2 with an average I_D/I_G of 1.42, 1.30, and 0.99, and I_{2D}/I_G of 1.53, 1.47, and 1.60, respectively. Additionally, BSE images illustrate improving characteristic sizes with increased gas ratio, as shown in Fig. 6.5a. The improvement of graphene quality with CH_4:H_2 ratio could likely be attributed to a high containing-carbon atmosphere, forming continuous islands and thicker films at a fast web speed compared to lower gas ratios [43].

Varying the web speed significantly affects roll-to-roll graphene synthesis by solar thermal CVD. Since the solar simulator heat flux is localized, axial heat conduction through the

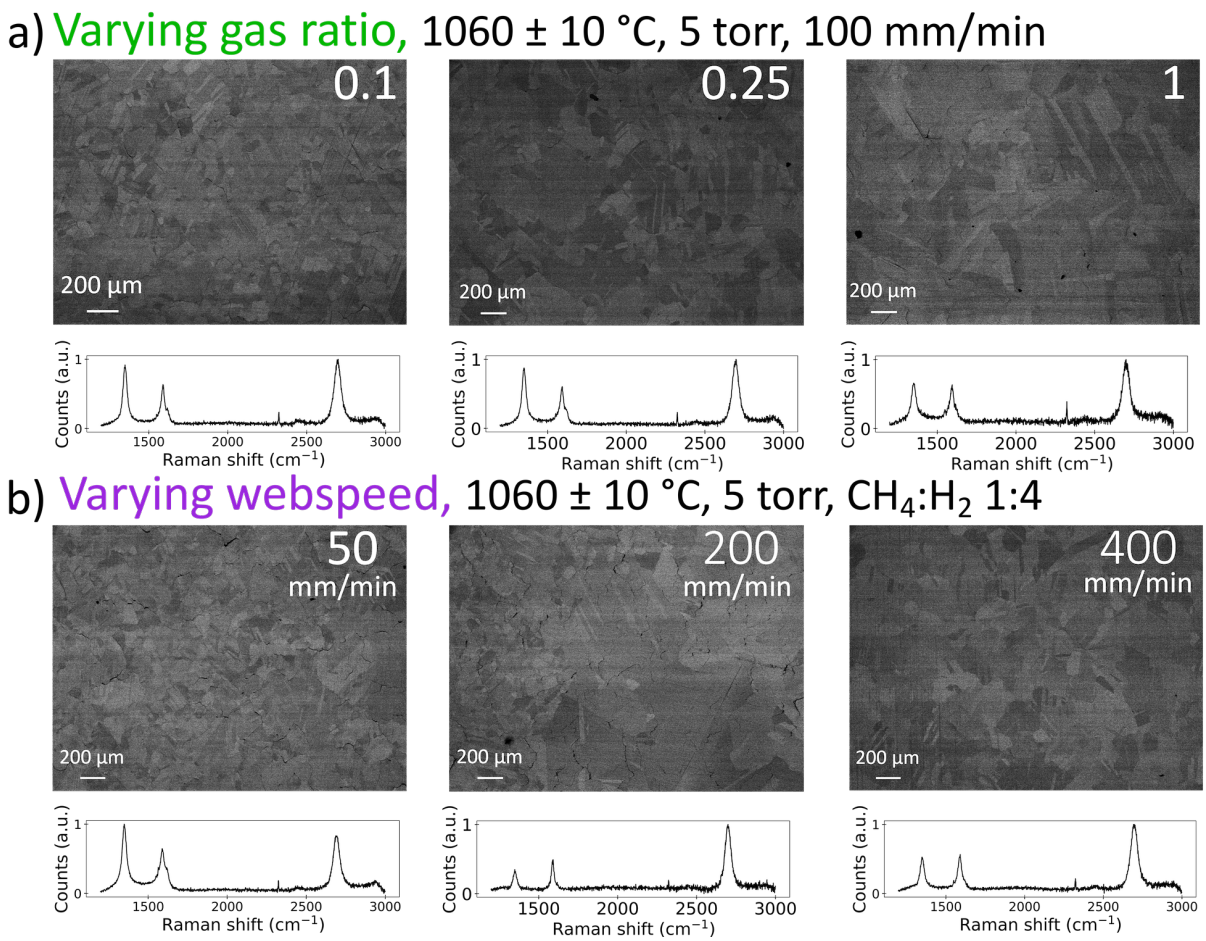

Figure 6.5: BSE images and Raman spectra that show characteristic sizes and graphene quality from Raman measurements (I_D/I_G) synthesized at different a) CH_4:H_2 of 0.1, 0.25, and 1, while other parameters are held at 1060℃, 5 torr, and 100 mm/min, and b) web speed of 50, 200, and 400 mm/min, while other parameters are held at 1060℃, 5 torr, and CH_4:H_2 1:4.

material is the most prominent source for increasing the upstream copper temperature. At higher speeds, the residence time for a particular copper section at the focal point and heated at an elevated temperature is low, and advection heat transfer is increased. Thus, higher speeds likely reduce the residence time of lower-quality graphene depositions prior to the focal point. Additionally, synthesizing thinner films, such as single-layer graphene, is feasible at faster speeds. Fig. 6.5b shows BSE images and Raman spectrum of graphene synthesized at 50, 200, and 400 mm/min, respectively, while other parameters are held at 1060℃, 5 torr, and CH_4:H_2 1:4. Results show improvements in quality and a decrease in thickness with speeds with average I_D/I_G of 1.33, 0.69, and 1.08, and I_{2D}/I_G of 1.58, 1.93, and 1.71, respectively, and single layer graphene characteristics are observed. Results show that at 200 mm/min, the best graphene quality is achieved. However, increasing the speed further leads to deterioration of quality, likely due to the formation of non-continuous islands.

6.3.2 Graphene spatial uniformity by roll-to-roll CVD

Graphene spatial uniformity has been studied by Raman spectroscopy across the Cu foil's width (25 mm) and length. The studied strip (75 mm in length) from roll-to-roll graphene synthesis, which was slowly annealed at 5 mm/min speed for 15 min before every synthesis, was further investigated. Raman measurements were acquired at the center in 1 mm increments across the foil's width as shown in Fig. 6.6a. Results show higher graphene uniformity within the region -10 to 10 mm from the centerline. Average values for I_D/I_G, I_{2D}/I_G, and FWHM of 1.16, 2.64 and 41.98 cm^{-1}, respectively, are reported here. Additionally, Raman measurements were acquired at +25 mm from the center (in the foil axial direction) and compared to the backside. Fig. 6.6a illustrates similar Raman spectra at different locations.

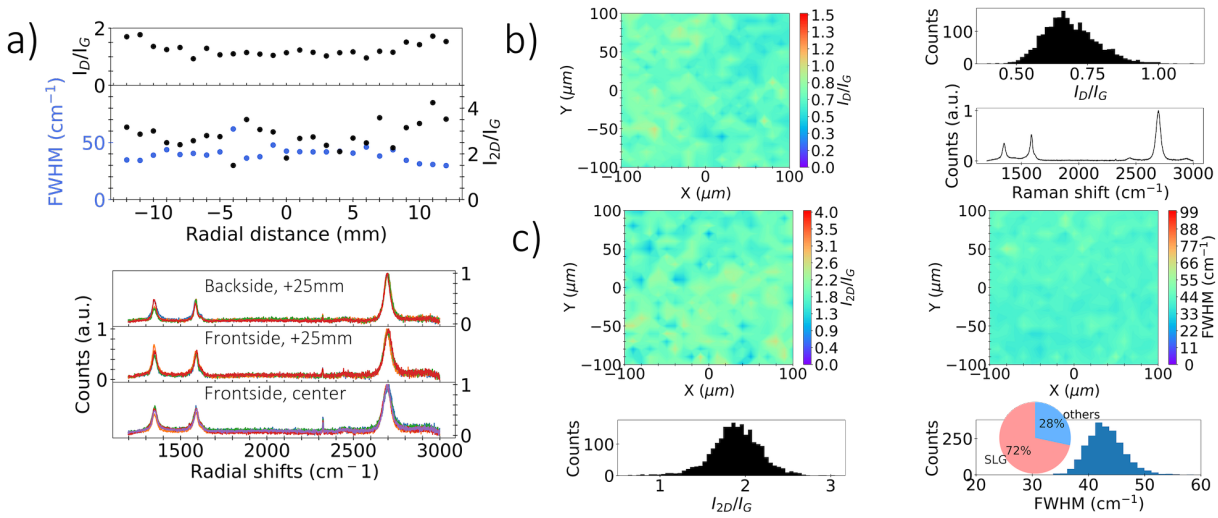

Figure 6.6: Single-layer graphene characterization: a) Raman measurements of graphene across the copper foil width and length to check film uniformity from I_D/I_G, I_{2D}/I_G, and FWHM. Raman mapping acquired from graphene on 300 nm SiO_2/Si graphene over characteristic lengths of 200 μm for b) I_D/I_G to study graphene uniformity with a histogram showing the distribution over five different spots. c) I_{2D}/I_G and FWHM to estimate SLG coverage when compared to other Raman spectra.

To further characterize synthesized graphene in this work, graphene films were transferred to thermal oxides following the procedures described in chapter 4.

In roll-to-roll synthesis, graphene is likely to grow on both surfaces, as shown in Fig. 6.6a. Thus, scotch tape was used to remove graphene from the backside, enabling etching copper by $FeCl_3$ during the transfer process. Raman mapping of graphene transferred to thermal oxides was conducted to assess graphene films quality, uniformity, coverage, and signature. Raman mapping was carried out at five different spots, where the I_D/I_G map and distribution histogram are illustrated in Figs. 6.6b, showing an average I_D/I_G of 0.69. Additionally, the Raman spectra in Figs. 6.6b show features similar to single-layer graphene (SLG) characteristics. Prior studies have reported SLG with distinctive Raman features, where the 2D

peak is symmetric with I_{2D}/I_G and FWMH in the range 1.8-2.8 and 34-45 cm^{-1}, respectively [13, 25–27, 34, 36, 148]. Fig. 6.6c illustrates Raman mappings of I_{2D}/I_G and FWHM, respectively, carried out on a characteristic length of 200 μm. The distribution of I_{2D}/I_G and FWHM of SLG at five different spots are illustrated in Fig. 6.6c. In this work, we observe SLG features, with average I_{2D}/I_G and FWHM of 1.90 and 43.0 cm^{-1}, respectively. Thus, the results reveal a graphene film with around 72% SLG coverage based on these Raman characteristics. Some factors can also impact the Raman measurements, such as contamination from the etching process (PMMA and $FeCl_3$ residuals) and the reference of thermal oxide.

6.3.3 Roll-to-roll design improvement for higher graphene quality

Despite roll-to-roll graphene synthesis at various conditions, the quality of graphene was not largely improved due to the deposition of low-quality graphene upstream of focal point. Prior studies [43, 160] have been carried out designing a concentric tube (CT) CVD, where the reactor was been separated into annealing and growth zones. Carbon-containing feedstock is injected only at the reaction zone, enabling the synthesis of high-quality graphene.

In the present work, attempts to improve graphene quality by controlling the upstream temperature and polishing the surface prior to the focal point have been carried out. Adding a tungsten slit puts the copper foil in contact with a large temperature reservoir from both sides. During processes, the slit temperature measured by a thermocouple is around 650℃. Studies have not reported any graphene growth below 500℃ [44] in thermal CVD; therefore, the approach mentioned above likely reduces the temperature of the upstream foil, limiting the synthesis of low-quality graphene prior to the focal point. Additionally, the slit applies

friction on the surface, pealing low-quality synthesized graphene before reaching the focal point. Fig. 6.7a shows the roll-to-roll setup with slit modification and the use of steel and tungsten wool to change the surface polishing finish.

Experiments were carried out at different conditions as shown in Fig. 6.7b. The effects of pressure, CH_4/H_2 ratio, and speed on graphene growth using the slit has been investigated at high temperatures around 1060℃. Other factors, such as the effect of surface finish and removal rate of low-quality graphene, can impact the conclusions drawn here, which have not been investigated thoroughly. Synthesis at low pressures of 5 and 10 torr, while other conditions held at 1060℃, CH_4/H_2 0.25, and 50 mm/min showed more high-quality Raman spectra compared to other conditions. Fig. 6.7c and 6.7d show Raman maps of both conditions, where synthesis at 5 torr exhibits a greater tendency toward high-quality graphene based on the low I_D/I_G ratios. As explained earlier, hydrogen and web speed play crucial roles in graphene quality.

Nevertheless, the effect of growth conditions cannot be solely used to draw conclusions because one cannot determine if graphene was synthesized on a polished surface or pre-existing low-quality graphene. However, graphene synthesis at 5 torr, CH_4/H_2 of 0.25, and 50 mm/min appears to provide the highest-quality graphene Raman signature.

Additionally, varying surface polish finish using oil-free extra fine grade steel (Briwax Internationl, Inc., #0000) and medium grade tungsten (MTS, 40312) wools to increase friction at the slit has been investigated. Fig. 6.7e and 6.7f show Raman maps of both conditions. The tungsten wool shows higher-graphene quality compared to the steel wool from the lower I_D/I_G ratios, where other factors such as the purity of the material, interaction with graphene, and surface roughness effects can be investigated. Studies have indicated

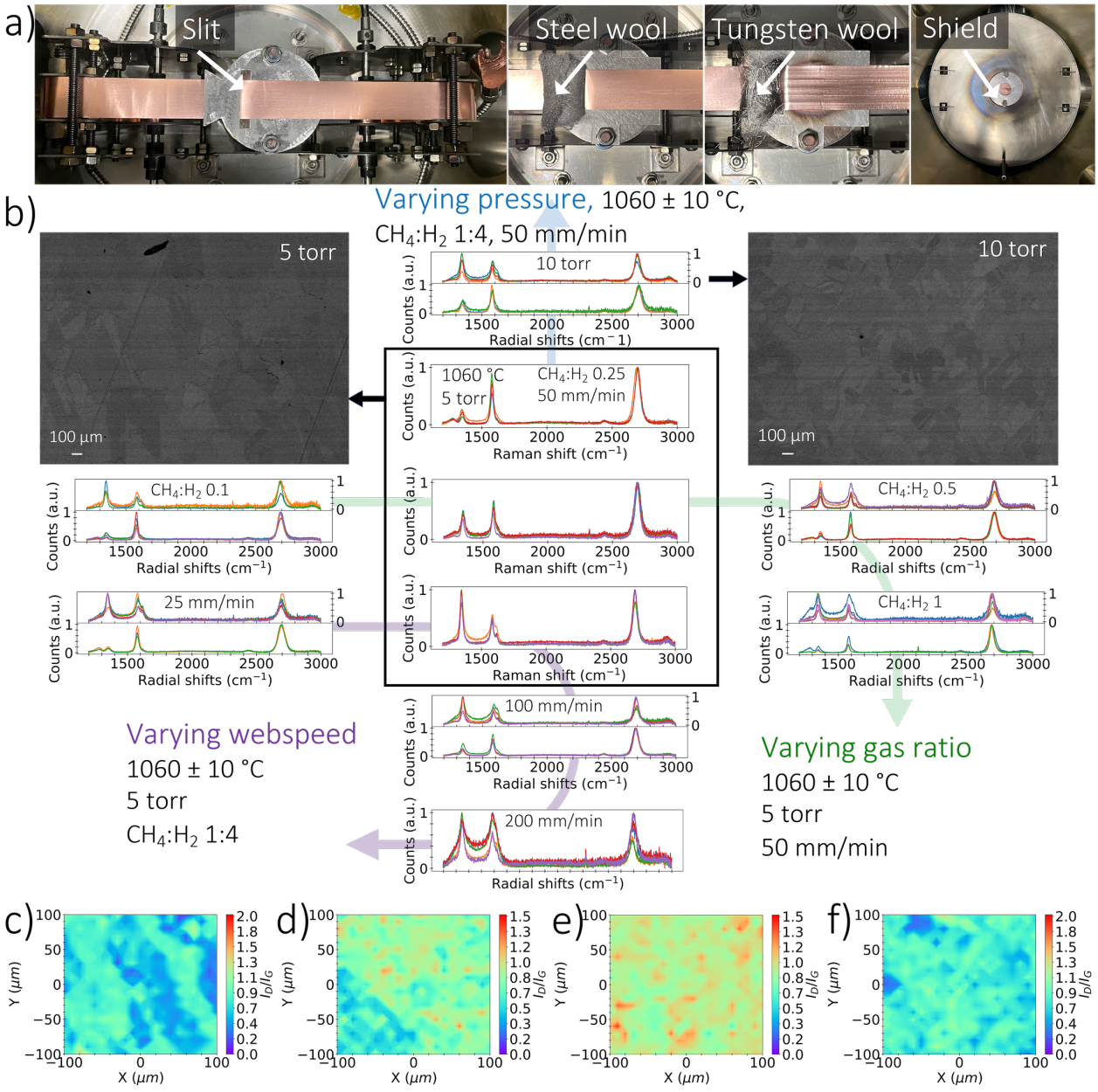

Figure 6.7: a) Roll design modification for the Roll-to-roll fixture to accommodate slit addition with steel and tungsten wools. b) The effect of varying growth conditions of pressure, CH_4:H_2, and web speed at 1060℃ accompanied with Raman spectra analysis and BSE images. Raman mapping of roll-roll graphene synthesized at c) 5 torr and d) 10 torr, while other parameters are held at 1060℃, CH_4:H_2 of 0.25, and 50 mm/min. Raman mapping of roll-to-roll graphene synthesized at the same conditions of c) using e) steel and f) tungsten wools.

that irregularities in surface roughness and grain boundaries of substrates affect the density and shape of graphene during nucleation and, therefore, graphene grain size and quality [26].

6.4 Conclusions

In this chapter, scaled production of graphene using roll-to-roll solar-thermal CVD has been demonstrated. Graphene synthesis at various conditions has been carried out to find the conditions that yield the optimum quality products. After studying the effect of different parameters, high temperatures and low pressures were generally found to improve graphene quality and the deposition of thinner films from 2D peak features in Raman spectra. The growth of low-quality graphene upstream of the focal point and at low temperatures hinders achieving high-quality films. Therefore, CH_4/H_2 and web speed were found to significantly impact roll-to-roll graphene quality after the predominant temperature effect. Graphene synthesis at 1060℃, 5 torr, CH_4/H_2 of 0.25, and 200 mm/min produces continuous films with at least 72% SLG coverage and moderate-quality graphene I_D/I_G of 0.7 suitable as transparent conductive electrodes [157]. Lower-quality graphene synthesized in this work can be applicable as oxidation barriers for metals [17, 42].

Studies have reported separating the annealing and growth zones through a custom design reactor to eliminate carbon-containing atmospheres at low temperatures, thus, achieving high-quality graphene synthesis. Design modification attempts have been carried out to lower the temperature of upstream foil to below limits that enable graphene nucleation by increasing conduction heat loss, as well as to remove low-quality graphene by surface polishing prior to graphene growth. This approach show domains of high-quality graphene,

but uniformity has yet to be achieved; hence, future studies can be carried out to modify the designs and eliminate carbon deposition before the focal point.

Closure

This thesis represents a detailed methodology for utilizing direct-solar capture in graphene synthesis alongside system design, heat transfer modeling, process optimization, and scaling-up for mass production. A custom-designed solar-thermal CVD system is illustrated to demonstrate the feasibility of using a renewable energy resource in driving graphene synthesis. It encompasses a HFSS with a 10 kW_e xenon arc lamp that mimics the solar spectrum, controllable with a peak flux in the 1.5-4.5 MW/m^2 range. The radiative heat flux from the HFSS has been characterized through an inverse numerical heat transfer model and infrared temperature imaging of an easily obtainable graphite sample. Automation and controls of the CVD system's instrument facilitate graphene synthesis under various conditions. A related numerical heat transfer model of the copper substrate was derived and validated to predict substrate temperature, a crucial parameter in graphene growth, enabling high-quality graphene growth. Other design parameters in graphene synthesis are CH_4:H_2 gas ratio, vacuum pressure, and residence time.

A parametric study using a probabilistic Gaussian regression model and an information acquisition function has been employed to guide us in finding the optimum conditions (low I_D/I_G). Characteristics tools, Raman mapping and electron diffraction, show high-quality single-layer graphene (SLG) and AB-stacked bilayer graphene features with an average I_D/I_G of 0.21 and 0.14, and grain sizes up to 5 and 20 μm, respectively. Such synthesis was conducted in a one-step process on a commercial copper substrate and at a relatively short growth time of 5 min with minimal preparation. The measured transmissivity of SLG and

AB-stacked bilayer graphene is in the 0.959-0.977 and 0.929-0.953 range, respectively. Using a 4-point probe with 1 mm spacings, the sheet measurement shows values in the 15.49±4.64 and 3.43±1.52 kΩ/sq range, respectively.

Scaling up the synthesized area can be achieved by displacing the lamp 4 mm out of its focal point to flatten the heat flux profile, thus achieving a more uniform temperature on a larger area. Raman I_D/I_G ratio, transmissivity, and sheet resistance measurements demonstrate spatial uniformity up to 20 mm in radius with values in the 0.13, 0.928-0.953, and 2-4 kΩ/sq range, respectively. Synthesized graphene shows high-quality products with promising capabilities applicable to photonic and electronic devices. Mass production using roll-to-roll remains the most efficient methodology for scaling graphene synthesis in solar-thermal CVD. Graphene synthesis at various conditions has been carried out to find the conditions that yield the best quality products. By studying the effect of different parameters (temperature, pressure, CH_4/H_2, and web speed), graphene was found to have the best quality at 1060℃, 5 torr, CH_4/H_2 of 0.25, and 200 mm/min. Results from Raman mapping show graphene synthesis with at least 72% SLG coverage and moderate quality (I_D/I_G of 0.7), suitable as transparent conductive electrodes. Lower-quality graphene from other conditions can still be applied as a barrier for metal oxidation.

Enhancing solar cavity design can be carried out by understanding the effect of temperature dependent optical properties of the quartz window on the heat flux profile deviations, similar to the work presented by Gurwich and Spector [101]. Irradiation with energetic particles such as ions, electrons, and photons can affect the mechanical, electronic, and magnetic properties of nanostructured carbon materials [173]. Photocatalytic effects in improving thermochemical reactions can be investigated in graphene synthesis. Prior studies have re-

ported photo-thermal excitation of polycyclic aromatic hydrocarbons [174]. Researchers have also reported photon irradiation effects on enhancing graphene growth [175] to the interaction of photon energy with the carbon structure, leading to the excitation and relaxation of electrons and a stable carbon sp2 hybridization during the synthesis process. Further studies are warranted to isolate such effects in the present direct solar process.

Graphene quality can be further improved using high-quality substrates [12, 13, 25], where some employed intricate sample preparation such as polishing and annealing over long hours. Others have reported using single-crystal Cu(111) [29] and Cu/Ni(111) alloy foils [147] to enable high-quality graphene synthesis with large grains and single-crystal domains. In roll-to-roll CVD, low-quality graphene growth at low temperatures upstream of the focal point hinder achieving high-quality products. Design modification to further lower the temperature of upstream foil below graphene nucleation limits can be enhanced through a cooling mechanism. An efficient surface polishing mechanisms can also be employed to peel low-quality graphene before reaching the focal point. However, reactor design can be improved as reported by some studies [43, 160], where the annealing and growth zones are separated through a concentric tube roll-to-roll CVD design, eliminating carbon feedstock outside the focal point.

Appendix A: Numerical modeling details

A.1 Indirect inverse flux mapping of a concentrated solar source using infrared imaging

A.1.1 Treatment of surrounding surfaces

As noted in the methodology section, the surrounding surfaces are assumed to have a uniform temperature of T_{sur}. Values for T_{sur} have been estimated based on IR camera temperature measurements of the vacuum chamber's inner walls from recorded regions outside of the radiometer's area in addition to the quartz window's external surface. Both temperature measurements were of similar magnitude and were further consistent with measurements recorded using a temperature transducer located on the outer surface of the cylindrical vacuum chamber after accounting for the expected temperature drop due to conduction across the stainless steel wall. Estimated values for T_{sur} averaged around 550 K. Additionally, the sensitivity of the numerical model towards T_{sur} is presented below, where results indicate a very weak sensitivity to the value of T_{sur}. Therefore, this insensitivity justifies the treatment of the surrounding temperature as uniform.

To investigate the effects of different surfaces within the vacuum chamber on radiation thermal exchange of the numerical model, a radiosity model is constructed and evaluated as shown in Fig. A.1. The radiosity model divides the vacuum chamber into two enclosures, where each enclosure is comprised of three surfaces; two surfaces represent the graphite radiometer, two surfaces represent the stainless steel cylindrical chamber, one surface rep-

resents the quartz window, and the last surface represents an imaginary blackbody surface. All surfaces within the model are assumed to be gray and at uniform temperatures. For the graphite radiometer, the surface is assumed to be at the average temperature of 1400 K with its corresponding hemispherical emissivity determined based on Eq. 2.6 at 1400 K. The assumption of a gray surface with the prescribed emissivity is justifiable by the minor contribution of thermal radiation from surrounding surfaces compared to that of the graphite. Additionally, the difference between $\varepsilon(T)$ and $\varepsilon(T_{\text{sur}})$ is too small to induce a non-negligible difference. As for the imaginary surface (surface 6 - see Fig. A.1), it is treated as a blackbody as a result of the adjacent larger cavity and is assumed to have a uniform temperature of 350 K; the rear portion of the vacuum chamber is at a significantly lower temperature than surfaces closer to the graphite radiometer.

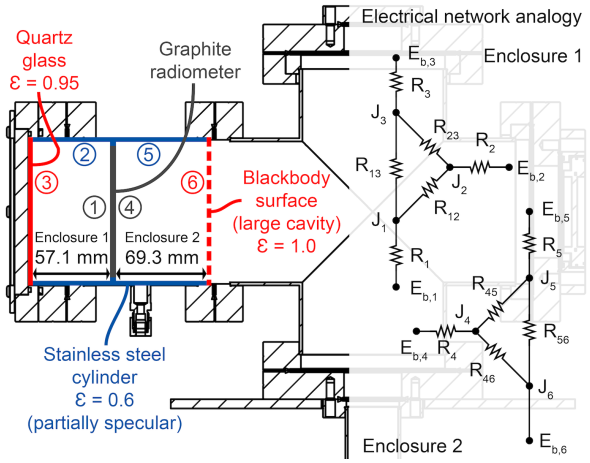

Figure A.1: Illustration of the radiosity model considered for the numerical heat transfer model, showing the vacuum chamber with different surfaces treated (left) and the constructed electrical network analogy (right).

Regarding the stainless steel cylindrical chamber, its two surfaces are assumed to have uniform temperatures of 550 K with gray emissivity of 0.6 [75, 98]. As all clean metals

are known to demonstrate strong specular reflection especially for thermal radiation [98], the stainless steel surface needs to be treated as a partially specular surface. Therefore, the radiosity model considers the surface to reflect 25% as a diffuse surface and 75% as specular, which is consistent with prior observations [176, 177]. This treatment provides diffuse (ϱ^d) and specular (ϱ^s) components of the stainless steel reflectance equivalent to 0.1 and 0.3. Finally for the quartz window, its surface is assumed to be opaque with an emissivity of 0.95 and a uniform temperature of 550 K. The assumption of an opaque surface is appropriate based on the scope of the radiosity model [98] and the relatively constant values for the combined emissivity and transmissivity of quartz [178, 179]. As transmitted radiation through the quartz window to the room does not affect the radiosity model's results of interest, and transmitted radiation has a negligible fraction of being redirected back into the vacuum chamber, such an assumption is valid.

The model consists of a system of equations that are solved simultaneously to determine the radiosity (J_i) and heat transfer rate (q_i) of each surface i. The results of interest here are the heat transfer rates of the graphite radiometer's two surfaces (i.e., q_1 and q_4). The combined transfer rate is then compared to that assuming black, uniform temperature surrounding surfaces to determine the associated error of such an assumption. To develop the radiosity model, equations for the heat transfer rate are constructed using [98]:

$$q_i = \frac{E_{b,i} - J_i/(1-\varrho_i^s)}{\varrho_i^d/\left[(1-\varrho_i^s)\varepsilon_i A_i\right]} = \sum_{j=1}^{N}\left[\frac{J_i}{1-\varrho_i^s} - \frac{J_j}{1-\varrho_j^s}\right](1-\varrho_i^s)(1-\varrho_j^s)A_i F_{ij}^s \ , \tag{A.1}$$

where $E_{b,i}$ is blackbody emissive power (σT_i^4), A_i is surface area, and F_{ij}^s is the specular view factor from surface i to surface j (i.e., fraction of thermal radiation leaving surface i that

intercepts surface j via direct diffuse emission or specular reflection). All diffuse view factors are obtained based on tabulated relations [98] for the view factor from a disk to another parallel coaxial disk of unequal radius, in addition to the view factor's summation and reciprocity relations. The specular view factors are then determined based on the crossed-strings method, and the corresponding summation relation is modified to be consistent with the new treatment of partially specular surfaces [98] to yield $\sum_{j=1}^{N}(1-\varrho_j^s)F_{ij}^s = 1$.

Based on the foregoing methodology and discussion, the radiosity model was solved to yield a combined heat transfer rate out of the graphite radiometer (q_1 and q_4) of 2085 W. In contrast, assuming a uniform black surrounding with a temperature T_{sur} of 550 K would yield a heat transfer rate out of $2\varepsilon\sigma A_1(T_1^4 - T_{\text{sur}}^4)$, which corresponds to 2112 W. This provides a relative percentage error of 1.28%, which is insignificant compared to other uncertainty estimates within the inverse model. Therefore, the assumption of the surrounding surfaces emitting like a blackbody can be implemented to reduce the complexity of the inverse model with no significant effect on the accuracy of its results. Finally, the estimated relative error is negligibly sensitive to the assumed radiometer's surface temperature ($T_1 = T_4 = 1400$ K), which further justifies the applicability of the comparison performed here to that of the actual temperature gradient observed.

A.1.2 Mesh independence study

A mesh independence study was conducted to evaluate the optimum mesh size to use and to verify the accuracy of the model, where numerical convergence was achieved around $\Delta r \sim 10^{-3}$ m. The value of Δz had an insignificant effect due to the thin graphite disk, and its value was set to 1×10^{-3} m. Results of the mesh independence study are shown in Fig. A.2

for the relative peak temperature error (at the center) of the front and back surfaces with respect to a very fine mesh. Additionally, the convergence criteria for the iterative numerical heat transfer model presented here was set to a maximum temperature error of 1×10^{-9}.

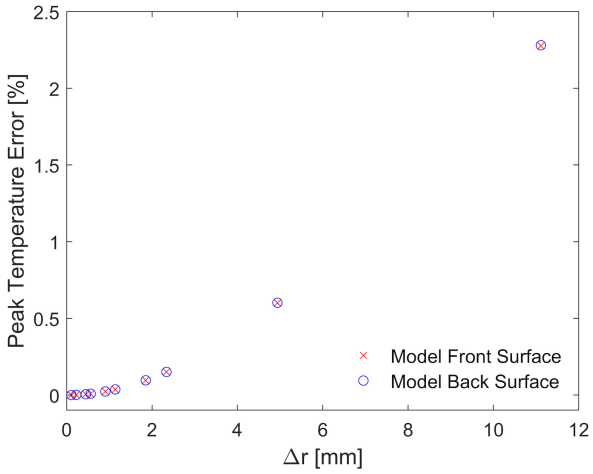

Figure A.2: Mesh independence study for the heat transfer numerical model.

A.1.3 Sensitivity analysis

A sensitivity analysis was conducted to determine the effect of different model parameters on the inverse heat flux distribution, as quantified by sensitivity coefficients, S_i, for the different parameters, i, involved in the inverse model. The sensitivity coefficients for peak heat flux ($S_{q'',i}$) and total power ($S_{Q,i}$) were determined through 5% perturbation above and below the nominal parameter values and by employing a central difference scheme using:

$$S_{q'',i} = \frac{\partial q''}{\partial \beta}\frac{\beta_0}{q''_0} = \frac{q''(\beta_0+\Delta\beta) - q''(\beta_0-\Delta\beta)}{2\Delta\beta}\frac{\beta_0}{q''_0}\ , \tag{A.2}$$

where β is the investigated parameter, $\Delta\beta$ is the parameter's associated uncertainty/perturbation, and the subscript '0' denotes values at nominal conditions (no perturbation). A similar equation is formulated for evaluating $S_{Q,i}$. Results of the sensitivity analysis are

shown in Fig. A.3, where the absolute values of the sensitivity coefficients are plotted and labeled as being positive or negative. A positive value indicates that a perturbation in the parameter value reflects a change in the determined quantity in the same direction (i.e., an increase in parameter value leads to an increase in the determined quantity).

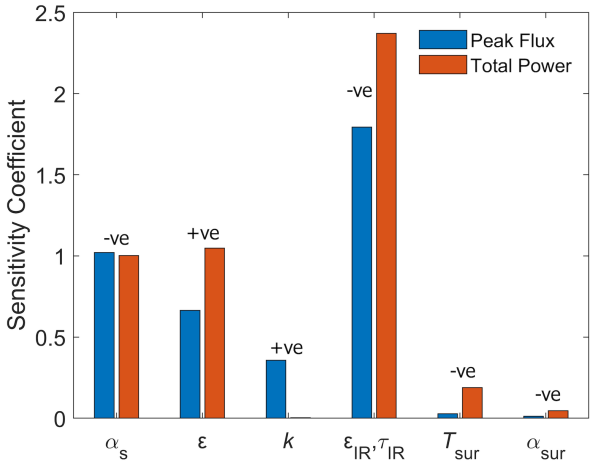

Figure A.3: Sensitivity analysis of model parameters for the inverse heat transfer mapping technique.

Based on results in Fig. A.3, both the peak flux and total power are most sensitive to the optical properties used by the IR camera to quantify temperatures of the radiometer, consisting of the calibrated graphite emissivity (ε_{IR}) and transmissivity of the ZnSe viewport (τ_{IR}). Therefore, care must be taken in evaluating these two parameters from spectral measurements either performed in-house or found in literature, and the parameters were further confirmed to be appropriate against temperature transducers. Therefore, the uncertainties in these two parameters are relatively low, especially given that graphite's emissivity in the far IR region is significantly less sensitive to surface conditions [93, 94]. The next two parameters with relatively high sensitivity coefficients are α_s and ε. The uncertainties in these two parameters, especially that of ε, are more sensitive to surface conditions and are expected

to contribute noticeably to the overall uncertainty in the determined heat flux distribution. However, as measurements were performed and averaged over five different trials for each operating condition, errors due to slight variations of surface condition are expected to be significantly reduced.

The radiometer's thermal conductivity follows next, but only the peak flux is sensitive to k. As shown in Fig. A.3, the total power determined by the inverse model is almost entirely unaffected by errors in thermal conductivity. With regards to the two final parameters that involve heat transfer to/from the surrounding (i.e., T_{sur} and α_{sur}), Fig. A.3 shows a very weak sensitivity towards these two parameters, making the assumption pertaining to a uniform and constant surrounding temperature justifiable.

A.1.4 Quartz thermal effects

The temperature of the quartz window was recorded using the IR camera positioned at the front side of the vacuum chamber and aligned off-axis at an approximate angle of 45°. The temperature contour of one of the measurements at a HFSS supply current of 140 A is shown in Fig. A.4, where the quartz window's assumed IR camera emissivity is 0.90. The assumed value is consistent with spectral emissivity measurements provided by the manufacturer (Technical Glass Products) within the IR camera's spectral range. As shown in Fig. A.4, the quartz window reaches relatively elevated temperatures and, more importantly, a large temperature gradient is observed on the window with temperatures varying from approximately 450 K to 700 K primarily as a result of variation in heat flux from the HFSS on the window (see Eq. 2.1). Such a temperature gradient can potentially cause a difference between the heat flux distribution measured using the HFG and that determined

from the inverse mapping technique (i.e., heat flux distribution inside and outside the vacuum chamber), as shown in Fig. 2.9 and demonstrated in other work [101]. Since the MCRT model does not consider temperature-dependent quartz optical properties or account for the effect of a large temperature gradient, the aforementioned difference was not captured by MCRT simulation results.

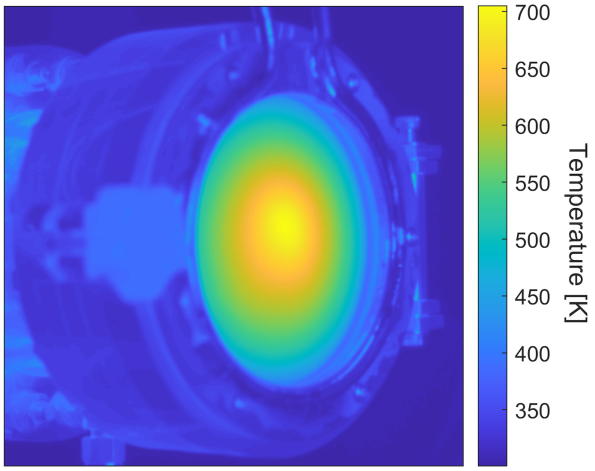

Figure A.4: Vacuum chamber's quartz window temperature distribution for a test at HFSS supply current of 140 A.

A detailed investigation regarding effects of the quartz window on the heat flux distribution inside the vacuum chamber is outside the scope of this work. However, a brief discussion is presented on the methodology of accounting for the window's optical properties variation with temperature. Such a variation in properties can be implemented into the MCRT simulation either by simply mapping the IR camera temperature measurements onto a corresponding plane that represents the quartz window in the ray tracing model, or by fitting a heat transfer numerical model that includes the quartz window, HFSS, cylindrical walls of chamber, and the radiometer. In the former approach, the MCRT model and the radiometer's inverse heat transfer model are completely independent. IR camera temperature

measurements are used to estimate temperature-dependent spatial optical properties of the quartz window within the MCRT simulation, which include varying window transmissivity and index of refraction. In contrast, for the latter approach, the heat transfer model of the quartz window is coupled to that of the radiometer and MCRT, where thermal properties of relevance can be additionally tuned to fit the IR camera measurements. Once the temperature distribution along the quartz window has been modeled, the distribution becomes an input to the MCRT simulation. The foregoing discussion provides the basis for a detailed investigation on the quartz window effects for high-flux systems in possible future work.

A.2 1D numerical heat transfer model for the copper substrate on tungsten mount

A.2.1 Numerical heat transfer model

The numerical heat transfer model for the copper substrate is divided into three control volumes (CVs) defined as follows: (1) interior nodes, (2) boundary condition (BC) at $r = 0$ and (3) BC at $r = R_c$. Additionally, the tungsten mount is divided into three regions with five control volumes defined as follows: (a) sample region which includes: (1) interior nodes and (2) BC at $r = 0$, (b) intermediate region and (c) outside of sample region which includes: (1) interior nodes and (2) BC at $r = R_t$ as illustrated in Fig. A.5.

By discretizing the governing equation (Eq. 3.2) using central finite difference, the energy balance for the copper substrate interior nodes produces:

$$T_i \left[\frac{2k_i}{\Delta r^2} + \frac{1}{\Delta z_c R_t''} + \frac{h}{\Delta z_c} \right] = T_{i+1} \left[\frac{k_i}{\Delta r^2} + \frac{k_i}{2r_i \Delta r} \right]$$
$$+ T_{i-1} \left[\frac{k_i}{\Delta r^2} - \frac{k_i}{2r_i \Delta r} \right] + \frac{\partial k_i / \partial T}{4\Delta r^2} \left[T_{i+1} - T_{i-1} \right]^2 + T_m \left[\frac{1}{\Delta z_c R_t''} \right]$$

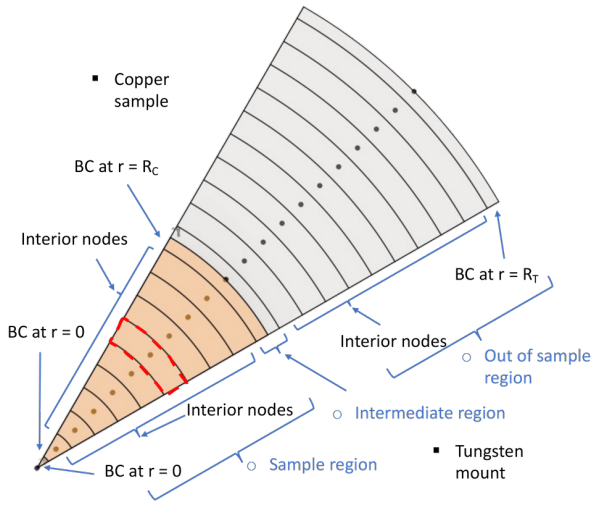

Figure A.5: Control volumes of the heat transfer model for the copper substrate and tungsten mount for different regions and boundary conditions.

$$-\frac{\varepsilon_i \sigma}{\Delta z_c} T_i^4 + \frac{\alpha_{surr} \sigma}{\Delta z_c} T_{surr}^4 + T_\infty \left[\frac{h}{\Delta z_c}\right] + \frac{\alpha_{solar}}{\Delta z_c} q''(r_i) \tag{A.3}$$

$$R_t'' = \left[\frac{\Delta z_c}{2k_i} + R_{tc}'' + \frac{\Delta z_t}{2k_m}\right] \tag{A.4}$$

where R_{tc}'' is thermal contact resistance as illustrated in Fig. A.6. A similar methodology is adopted for the remaining seven control volumes.

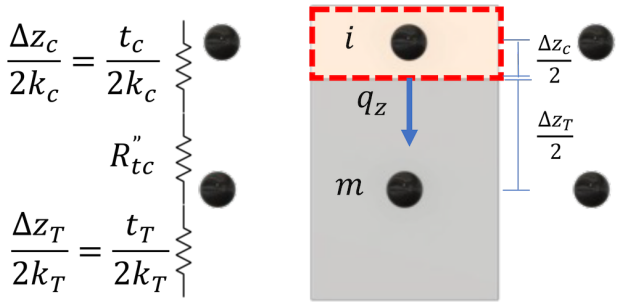

Figure A.6: Cross-sectional view of the control volume for the copper substrate/tungsten mount to illustrate the thermal contact resistance.

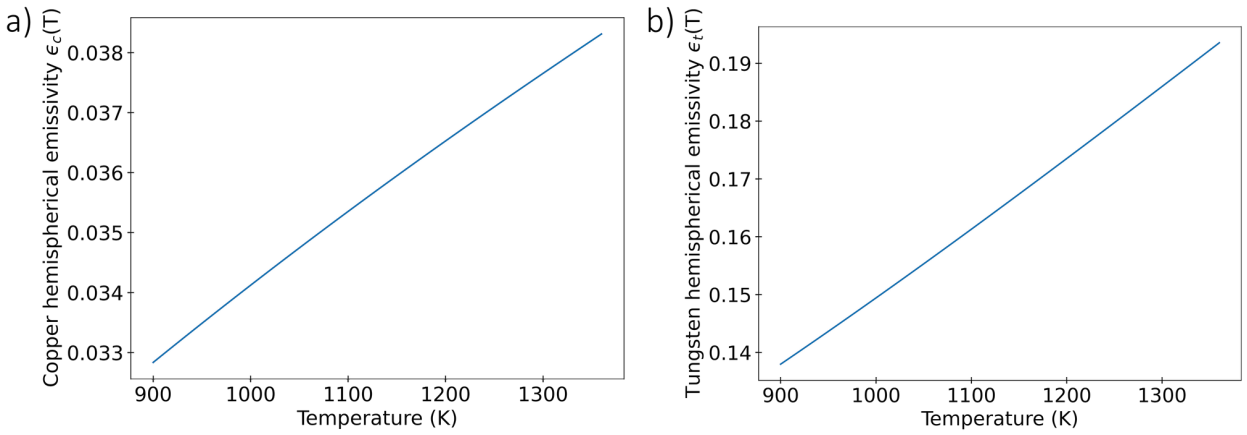

Figure A.7: Hemispherical emissivity of a) copper and b) tungsten as a function of temperature.

A.2.2 The hemispherical emissivity of copper and tungsten

The hemispherical emissivity of both copper and tungsten were calculated from normal spectral emissivity values carried out by prior studies[98, 114–119, 121–126] and the estimated ϵ/ϵ_n ratio from electromagnetic wave theory[98] that is correlated to the indices of refraction n and k of these metals[128]. The hemispherical emissivities of a) copper and b) tungsten as a function of temperature are shown in Fig. A.7

A.2.3 Validation of numerical model with temperature measurements

To validate the numerical heat transfer, the percentage error between the model and pyrometer measurements for 100 tests carried out at various experimental conditions are shown Fig. A.8

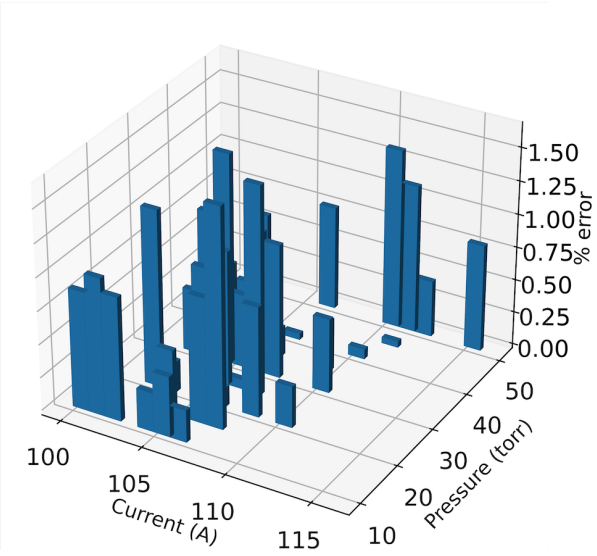

Figure A.8: Percentage error between the peak temperature from the numerical heat transfer model and pyrometer temperature measurements at different experimental conditions

References

1. Geim, A. K. & Novoselov, K. S. The rise of graphene. *Nature materials* **6,** 183–191 (2007).

2. Geim, A. K. Graphene: Status and Prospects. *Science* **324,** 1530–1534 (2009).

3. Nair, R. R. *et al.* Fine structure constant defines visual transparency of graphene. *Science* **320,** 1308. ISSN: 00368075 (2008).

4. Ho, P. H. *et al.* Sunlight-activated graphene-heterostructure transparent cathodes: Enabling high-performance n-graphene/p-Si Schottky junction photovoltaics. *Energy and Environmental Science* **8,** 2085–2092. ISSN: 17545706 (2015).

5. Yoon, J. *et al.* Superflexible, high-efficiency perovskite solar cells utilizing graphene electrodes: Towards future foldable power sources. *Energy and Environmental Science* **10,** 337–345. ISSN: 17545706 (2017).

6. Lee, C., Wei, X., Kysar, J. W. & Hone, J. Measurement of the elastic properties and intrinsic strength of monolayer graphene. *Science* **321,** 385–388. ISSN: 00368075 (2008).

7. Bera, R. *et al.* Graphene–Porphyrin Nanorod Composites for Solar Light Harvesting. *ACS Sustainable Chemistry & Engineering* **4,** 1562–1568 (2016).

8. Xiong, G. *et al.* Bioinspired leaves-on-branchlet hybrid carbon nanostructure for supercapacitors. *Nature Communications* **9,** 790. ISSN: 2041-1723 (Dec. 2018).

9. He, P. *et al.* Large-scale synthesis and activation of polygonal carbon nanofibers with thin ribbon-like structures for supercapacitor electrodes. *RSC Advances* **5,** 31837–31844. ISSN: 2046-2069 (2015).

10. Sun, Y., Wu, Q. & Shi, G. Graphene based new energy materials. *Energy Environ. Sci.* **4,** 1113–1132 (4 2011).

11. Zhao, Y. *et al.* Highly Reduced Graphene Assembly Film as Current Collector for Lithium Ion Batteries. *ACS Sustainable Chemistry & Engineering* **9,** 8635–8641 (2021).

12. Yan, K., Peng, H., Zhou, Y., Li, H. & Liu, Z. Formation of bilayer bernal graphene: Layer-by-layer epitaxy via chemical vapor deposition. *Nano Letters* **11,** 1106–1110. ISSN: 15306984 (2011).

13. Liu, L. *et al.* High-yield chemical vapor deposition growth of high-quality large-area AB-stacked bilayer graphene. *ACS Nano* **6,** 8241–8249. ISSN: 19360851 (2012).

14. Hernandez, Y. *et al.* High-yield production of graphene by liquid-phase exfoliation of graphite. *Nature Nanotechnology* **3.** ISSN: 1748-3387 (Sept. 2008).

15. Paton, K. R. *et al.* Scalable production of large quantities of defect-free few-layer graphene by shear exfoliation in liquids. *Nature Materials* **13.** ISSN: 1476-1122 (June 2014).

16. Zhao, S. *et al.* Green and High-Efficiency Production of Graphene by Tannic Acid-Assisted Exfoliation of Graphite in Water. *ACS Sustainable Chemistry & Engineering* **6,** 7652–7661 (2018).

17. Alrefae, M. A. *et al.* Process optimization of graphene growth in a roll-to-roll plasma CVD system. *AIP Advances* **7,** 115102. ISSN: 2158-3226 (Nov. 2017).

18. Yamada, T., Kim, J., Ishihara, M. & Hasegawa, M. Low-temperature graphene synthesis using microwave plasma CVD. *Journal of Physics D: Applied Physics* **46,** 063001. ISSN: 0022-3727 (Feb. 2013).

19. Gopalakrishnan, B., Mardikar, Y. & Korakakis, D. Energy analysis in semiconductor manufacturing. *Energy Engineering: Journal of the Association of Energy Engineering* **107,** 6–40. ISSN: 15460118 (2010).

20. Chen, Steve; Gautam, A. W. F. Bringing energy efficiency to the fab. *McKinsey on Semiconductors,* 52–55 (2013).

21. EIA. *U.S. Energy Information Administration, How much carbon dioxide is produced per kilowatthour of U.S. electricity generation?* 2020. `https://www.eia.gov/tools/faqs/faq.php?id=74&t=11`.

22. Pedersen, H., Barry, S. T. & Sundqvist, J. Green CVD—Toward a sustainable philosophy for thin film deposition by chemical vapor deposition. *Journal of Vacuum Science & Technology A* **39,** 051001 (2021).

23. Kim, Y. S. *et al.* Methane as an effective hydrogen source for single-layer graphene synthesis on Cu foil by plasma enhanced chemical vapor deposition. *Nanoscale* **5,** 1221. ISSN: 2040-3364 (2013).

24. Malesevic, A. *et al.* Synthesis of few-layer graphene via microwave plasma-enhanced chemical vapour deposition. *Nanotechnology* **19,** 305604. ISSN: 0957-4484 (July 2008).

25. Alnuaimi, A., Almansouri, I., Saadat, I. & Nayfeh, A. Toward fast growth of large area high quality graphene using a cold-wall CVD reactor. *RSC Advances* **7,** 51951–51957. ISSN: 20462069 (2017).

26. Kim, H. *et al.* Activation energy paths for graphene nucleation and growth on Cu. *ACS Nano* **6,** 3614–3623. ISSN: 19360851 (2012).

27. Bhaviripudi, S., Jia, X., Dresselhaus, M. S. & Kong, J. Role of kinetic factors in chemical vapor deposition synthesis of uniform large area graphene using copper catalyst. *Nano Letters* **10,** 4128–4133. ISSN: 15306984 (2010).

28. Vlassiouk, I. *et al. Role of hydrogen in chemical vapor deposition growth of large single-crystal graphene* in *ACS Nano* **5** (2011).

29. Ta, H. Q. *et al.* Stranski-Krastanov and Volmer-Weber CVD Growth Regimes to Control the Stacking Order in Bilayer Graphene. *Nano Letters* **16,** 6403–6410. ISSN: 15306992 (2016).

30. Xing, S., Wu, W., Wang, Y., Bao, J. & Pei, S. S. Kinetic study of graphene growth: Temperature perspective on growth rate and film thickness by chemical vapor deposition. *Chemical Physics Letters* **580,** 62–66. ISSN: 00092614 (2013).

31. Yoon, H., Shin, D. S., Kim, T. G., Kim, D. & Park, J. Facile Synthesis of Graphene on Cu Nanowires via Low-Temperature Thermal CVD for the Transparent Conductive Electrode. *ACS Sustainable Chemistry & Engineering* **6,** 13888–13896 (2018).

32. Bointon, T. H., Barnes, M. D., Russo, S. & Craciun, M. F. High Quality Monolayer Graphene Synthesized by Resistive Heating Cold Wall Chemical Vapor Deposition. *Advanced Materials* **27,** 4200–4206. ISSN: 09359648 (July 2015).

33. Miseikis, V. *et al.* Rapid CVD growth of millimetre-sized single crystal graphene using a cold-wall reactor. *2D Materials* **2,** 014006. ISSN: 2053-1583 (Jan. 2015).

34. Cabrero-Vilatela, A., Weatherup, R. S., Braeuninger-Weimer, P., Caneva, S. & Hofmann, S. Towards a general growth model for graphene CVD on transition metal catalysts. *Nanoscale* **8,** 2149–2158. ISSN: 20403372 (2016).

35. Cai, W. *et al.* Synthesis of isotopically-labeled graphite films by cold-wall chemical vapor deposition and electronic properties of graphene obtained from such films. *Nano Research* **2,** 851–856. ISSN: 1998-0124 (Nov. 2009).

36. Huang, L. *et al.* Synthesis of high-quality graphene films on nickel foils by rapid thermal chemical vapor deposition. *Carbon* **50,** 551–556. ISSN: 00086223 (Feb. 2012).

37. Ekman, B. M., Brooks, G. & Rhamdhani, M. A. in *Energy Technology 2015* 149–159 (Springer International Publishing, Cham, 2015). ISBN: 9783319482200.

38. Abuseada, M., Alghfeli, A. & Fisher, T. S. Indirect inverse flux mapping of a concentrated solar source using infrared imaging. *Review of Scientific Instruments* **93,** 073101. ISSN: 0034-6748 (2022).

39. Alghfeli, A., Abuseada, M. & Fisher, T. S. Solar-thermal cold-wall chemical vapor deposition reactor design and characterization for graphene synthesis. *Journal of Vacuum Science & Technology B* **40,** 064205 (2022).

40. Bilionis, I. *Introduction to Uncertainty* 2018. `https://github.com/PredictiveScienceLab/uq-course`.

41. Ferrari, A. C. & Basko, D. M. Raman spectroscopy as a versatile tool for studying the properties of graphene. *Nature nanotechnology* **8,** 235–246 (2013).

42. Kalita, G. *et al.* Low temperature deposited graphene by surface wave plasma CVD as effective oxidation resistive barrier. *Corrosion Science* **78,** 183–187. ISSN: 0010-938X (2014).

43. Kidambi, P. R. *et al.* A Scalable Route to Nanoporous Large-Area Atomically Thin Graphene Membranes by Roll-to-Roll Chemical Vapor Deposition and Polymer Support Casting. *ACS Applied Materials & Interfaces* **10.** PMID: 29553242, 10369–10378 (2018).

44. Binti Anuar, N. A. *et al.* Low-temperature growth of graphene nanoplatelets by hot-wire chemical vapour deposition. *Surface and Coatings Technology* **411,** 126995. ISSN: 0257-8972 (2021).

45. Tembhurne, S., Nandjou, F. & Haussener, S. A thermally synergistic photo-electrochemical hydrogen generator operating under concentrated solar irradiation. *Nature Energy* **4,** 399–407. ISSN: 2058-7546 (2019).

46. Abuseada, M., Wei, C., Spearrin, R. M. & Fisher, T. S. Solar–thermal production of graphitic carbon and hydrogen via methane decomposition. *Energy & Fuels* **36,** 3920–3928. ISSN: 0887-0624 (Apr. 2022).

47. Hu, B., Li, B., Zhao, R. & Yang, T. Reflection-type single long-pulse solar simulator for high-efficiency crystalline silicon photovoltaic modules. *Review of Scientific Instruments* **82,** 065104. ISSN: 0034-6748 (2011).

48. Jin, J. *et al.* Ultrahigh temperature processing by concentrated solar energy with accurate temperature measurement. *Applied Thermal Engineering* **150,** 1337–1344. ISSN: 13594311 (2019).

49. Hu, Y., Abuseada, M., Alghfeli, A., Holdheim, S. & Fisher, T. S. High-temperature thermal diffusivity measurements using a modified Ångström's method with transient infrared thermography. *Journal of Heat Transfer* **144,** 023502. ISSN: 0022-1481 (Feb. 2022).

50. Gallo, A., Marzo, A., Fuentealba, E. & Alonso, E. High flux solar simulators for concentrated solar thermal research: A review. *Renewable and Sustainable Energy Reviews* **77,** 1385–1402. ISSN: 13640321 (2017).

51. Steinfeld, A., Brack, M., Meier, A., Weidenkaff, A. & Wuillemin, D. A solar chemical reactor for co-production of zinc and synthesis gas. *Energy* **23,** 803–814. ISSN: 03605442 (1998).

52. Abuseada, M., Ophoff, C. & Ozalp, N. Characterization of a New 10 kWe High Flux Solar Simulator Via Indirect Radiation Mapping Technique. *Journal of Solar Energy Engineering* **141,** 1–14. ISSN: 0199-6231 (2019).

53. Levêque, G., Bader, R., Lipiński, W. & Haussener, S. Experimental and numerical characterization of a new 45 kW_el multisource high-flux solar simulator. *Optics Express* **24,** A1360. ISSN: 1094-4087 (2016).

54. Gill, R., Bush, E., Haueter, P. & Loutzenhiser, P. Characterization of a 6 kW high-flux solar simulator with an array of xenon arc lamps capable of concentrations of nearly 5000 suns. *Review of Scientific Instruments* **86,** 125107. ISSN: 0034-6748 (2015).

55. Krueger, K. R., Lipiński, W. & Davidson, J. H. Operational performance of the University of Minnesota 45 kWe high-flux solar simulator. *Journal of Solar Energy Engineering* **135,** 044501. ISSN: 0199-6231 (2013).

56. Lei, F. *et al.* Non-catalytic ethane cracking using concentrated solar energy. *Chemical Engineering Journal* **355,** 58–64. ISSN: 13858947 (2019).

57. Sarwar, J., Georgakis, G., LaChance, R. & Ozalp, N. Description and characterization of an adjustable flux solar simulator for solar thermal, thermochemical and photovoltaic applications. *Solar Energy* **100,** 179–194. ISSN: 0038092X (2014).

58. Abuseada, M. *An experimental and numerical study on the heat transfer driven dynamics and control of transient variations in a solar reactor* MA thesis (University of Minnesota, 2019), 1–149.

59. Xiao, J., Yang, H., Wei, X. & Li, Z. A novel flux mapping system for high-flux solar simulators based on the indirect method. *Solar Energy* **179,** 89–98. ISSN: 0038092X (2019).

60. Kuhn, P. & Hunt, A. A new solar simulator to study high temperature solid-state reactions with highly concentrated radiation. *Solar Energy Materials* **24,** 742–750. ISSN: 01651633 (1991).

61. Wang, W., Aichmayer, L., Garrido, J. & Laumert, B. Development of a Fresnel lens based high-flux solar simulator. *Solar Energy* **144,** 436–444. ISSN: 0038092X (2017).

62. Garrido, J., Aichmayer, L., Wang, W. & Laumert, B. Characterization of the KTH high-flux solar simulator combining three measurement methods. *Energy* **141,** 2091–2099. ISSN: 03605442 (2017).

63. Pozzobon, V. & Salvador, S. High heat flux mapping using infrared images processed by inverse methods: An application to solar concentrating systems. *Solar Energy* **117,** 29–35. ISSN: 0038092X (2015).

64. Ngo, T.-T., Huang, J.-H. & Wang, C.-C. Inverse simulation and experimental verification of temperature-dependent thermophysical properties. *International Communications in Heat and Mass Transfer* **71,** 137–147. ISSN: 07351933 (2016).

65. Alifanov, O. M. Solution of an inverse problem of heat conduction by iteration methods. *Journal of Engineering Physics* **26,** 471–476. ISSN: 0022-0841 (1974).

66. Alifanov, O. M. & Egorov, Y. V. Algorithms and results of solving the inverse heat-conduction boundary problem in a two-dimensional formulation. *Journal of Engineering Physics* **48,** 489–496. ISSN: 0022-0841 (1985).

67. Su, J. & Silva Neto, A. J. Two-dimensional inverse heat conduction problem of source strength estimation in cylindrical rods. *Applied Mathematical Modelling* **25,** 861–872. ISSN: 0307904X (2001).

68. Kim, S., Kim, M. C. & Kim, K. Y. An integral approach to the inverse estimation of temperature-dependent thermal conductivity without internal measurements. *International Communications in Heat and Mass Transfer* **29,** 107–113. ISSN: 07351933 (2002).

69. Kim, S., Kim, M. C. & Kim, K. Y. Non-iterative estimation of temperature-dependent thermal conductivity without internal measurements. *International Journal of Heat and Mass Transfer* **46,** 1801–1810. ISSN: 00179310 (2003).

70. Chang, C.-L. & Chang, M. Non-iteration estimation of thermal conductivity using finite volume method. *International Communications in Heat and Mass Transfer* **33,** 1013–1020. ISSN: 07351933 (2006).

71. Li, H., Lei, J. & Liu, Q. An inversion approach for the inverse heat conduction problems. *International Journal of Heat and Mass Transfer* **55,** 4442–4452. ISSN: 00179310 (2012).

72. Singhal, M., Singh, S., Singla, R. K., Goyal, K. & Jain, D. Experimental and computational inverse thermal analysis of transient, non-linear heat flux in circular pin fin with temperature-dependent thermal properties. *Applied Thermal Engineering* **168,** 114721. ISSN: 13594311 (2020).

73. Singh, N. P. & Reddy, K. Inverse heat transfer technique for estimation of focal flux distribution for a concentrating photovoltaic (CPV) square solar parabola dish collector. *Renewable Energy* **145,** 2783–2795. ISSN: 09601481 (2020).

74. Krueger, K. R. *Design and characterization of a concentrating solar simulator* PhD (University of Minnesota, Minneapolis, MN, 2012), 1–151. `https://hdl.handle.net/11299/137873`.

75. Abuseada, M. & Ozalp, N. Experimental and numerical study on a novel energy efficient variable aperture mechanism for a solar receiver. *Solar Energy* **197,** 396–410. ISSN: 0038092X (2020).

76. Learn, D., Forbes, P. & Sambuco, C. Photosafety Assessment. *A Comprehensive Guide to Toxicology in Nonclinical Drug Development,* 585–614 (2017).

77. Ballestrín, J. *et al.* Systematic error in the measurement of very high solar irradiance. *Solar Energy Materials and Solar Cells* **80,** 375–381. ISSN: 09270248 (Nov. 2003).

78. Nelder, J. A. & Mead, R. A simplex method for function minimization. *The computer journal* **7,** 308–313 (1965).

79. Gao, F. & Han, L. Implementing the Nelder-Mead simplex algorithm with adaptive parameters. *Computational Optimization and Applications* **51,** 259–277 (2012).

80. Howell, J. R. The Monte Carlo Method in Radiative Heat Transfer. *Journal of Heat Transfer* **120,** 547–560. ISSN: 0022-1481 (1998).

81. Delatorre, J. *et al.* Monte Carlo advances and concentrated solar applications. *Solar Energy* **103,** 653–681. ISSN: 0038092X (2014).

82. Abuseada, M. & Ozalp, N. Numerical Characterization of a High Flux Solar Simulator Using Forward and Inverse Methods. *Journal of Heat Transfer* **142,** 022105. ISSN: 0022-1481 (2020).

83. Vauhkonen, M., Tarvainen, T. & Lähivaara, T. in *Mathematical Modelling* 207–227 (Springer, 2016).

84. Aster, R. C., Borchers, B. & Thurber, C. H. *Parameter Estimation and Inverse Problems* 3rd Editio, 1–209 (Elsevier, 2018).

85. Dai, S., Chang, Z., Ma, T., Wang, L. & Li, X. Experimental study on flux mapping for a novel 84 kWe high flux solar simulator. *Applied Thermal Engineering* **162,** 114319. ISSN: 13594311 (2019).

86. Gomez-Garcia, F., Santiago, S., Luque, S., Romero, M. & Gonzalez-Aguilar, J. *A new laboratory-scale experimental facility for detailed aerothermal characterizations of volumetric absorbers* in *AIP Conference Proceedings* **1734** (2016), 030018.

87. Xiao, J., Wei, X., Gilaber, R. N., Zhang, Y. & Li, Z. Design and characterization of a high-flux non-coaxial concentrating solar simulator. *Applied Thermal Engineering* **145,** 201–211. ISSN: 13594311 (2018).

88. Fisher, T. S. in *Thermal Energy at the Nanoscale* 113–156 (WORLD SCIENTIFIC, 2013).

89. Bapat, S. & Nickel, H. Thermal conductivity and electrical resistivity of poco grade AXF-Q1 graphite to 3300° K. *Carbon* **11,** 323–327. ISSN: 00086223 (1973).

90. Kittel, C. *Introduction to solid state physics* 8th, 155–157. ISBN: 047141526X (Wiley, 2004).

91. Pavlov, T. *et al.* A new numerical method and modified apparatus for the simultaneous evaluation of thermo-physical properties above 1500 K: A case study on isostatically pressed graphite. *Thermochimica Acta* **652,** 39–52. ISSN: 00406031 (2017).

92. Entegris. *Properties and characteristics of graphite* 2013. `https://www.entegris.com/content/dam/web/resources/brochures/brochure-properties-and-characteristics-of-graphite-7329.pdf`.

93. Autio, G. & Scala, E. The normal spectral emissivity of isotropic and anisotropic materials. *Carbon* **4,** 13–28. ISSN: 00086223 (1966).

94. Plunkett, J. D. & Kingery, W. D. in *Carbon* 457–472 (Pergamon, 1960). ISBN: 978-1-4831-9835-4.

95. Champetier, R. J. *Basal plane emittance of pyrolytic graphite at elevated temperatures* tech. rep. (AEROSPACE CORP EL SEGUNDO CA LAB OPERATIONS, 1967).

96. Thorn, R. J. & Simpson, O. C. Spectral Emissivities of Graphite and Carbon. *Journal of Applied Physics* **24,** 633–639. ISSN: 0021-8979 (1953).

97. Abbott, G., Alvares, N. & Parker, W. *Total normal and total hemispherical emittance of polished metals* tech. rep. WADD-TR-61-94 (Naval Radiological Defense Lab San Francisco, CA, 1961).

98. Modest, M. F. *Radiative Heat Transfer* 3rd, 73–82 and 829. ISBN: 9780123869449 (Elsevier, 2013).

99. Djurišić, A. B. & Li, E. H. Optical properties of graphite. *Journal of Applied Physics* **85,** 7404–7410. ISSN: 0021-8979 (1999).

100. Philipp, H. R. Infrared optical properties of graphite. *Physical Review B* **16,** 2896 (1977).

101. Gurwich, I. & Spector, M. The thermal lens effect on laser heating of a metal nanosphere particle immersed in oil. *Journal of Quantitative Spectroscopy and Radiative Transfer* **252,** 107066. ISSN: 00224073 (Sept. 2020).

102. Steinfeld, A. Solar thermochemical production of hydrogen—a review. *Solar Energy* **78,** 603–615. ISSN: 0038092X (May 2005).

103. Romero, M. & Steinfeld, A. Concentrating solar thermal power and thermochemical fuels. *Energy & Environmental Science* **5,** 9234. ISSN: 1754-5692 (2012).

104. Chueh, W. C. *et al.* High-Flux Solar-Driven Thermochemical Dissociation of CO2 and H2O Using Nonstoichiometric Ceria. *Science* **330,** 1797–1801. ISSN: 0036-8075 (Dec. 2010).

105. Ozalp, N., Epstein, M. & Kogan, A. Cleaner pathways of hydrogen, carbon nanomaterials and metals production via solar thermal processing. *Journal of Cleaner Production* **18,** 900–907. ISSN: 09596526 (June 2010).

106. Petrasch, J. *et al.* A novel 50 kW 11,000 suns high-flux solar simulator based on an array of xenon arc lamps. *Journal of Solar Energy Engineering, Transactions of the ASME* **129,** 405–411. ISSN: 01996231 (Nov. 2007).

107. Abuseada, M., Ophoff, C. & Ozalp, N. Characterization of a New 10 kWe High Flux Solar Simulator Via Indirect Radiation Mapping Technique. *Journal of Solar Energy Engineering* **141.** ISSN: 0199-6231 (Apr. 2019).

108. Abuseada, M. & Ozalp, N. Numerical Characterization of a High Flux Solar Simulator Using Forward and Inverse Methods. *Journal of Heat Transfer* **142.** ISSN: 0022-1481 (Feb. 2020).

109. Pae, J. Y., Medwal, R., Vas, J. V., Matham, M. V. & Rawat, R. S. Remote plasma-assisted low-temperature large-area graphene synthesis. *Journal of Vacuum Science & Technology B* **37.** ISSN: 2166-2746 (4 2019).

110. Katz, D., Lee, S. W., Lopez, D., Kornblit, A. & Grebel, H. Synthesis of carbon nanotubes: Controlled fabrication of intraconnects. *Journal of Vacuum Science & Technology B: Microelectronics and Nanometer Structures* **25.** ISSN: 10711023 (2007).

111. Franklin, A. D., Sayer, R. A., Sands, T. D., Fisher, T. S. & Janes, D. B. Toward surround gates on vertical single-walled carbon nanotube devices. *Journal of Vacuum Science & Technology B: Microelectronics and Nanometer Structures* **27.** ISSN: 10711023 (2009).

112. Mogera, U., Kurra, N., Radhakrishnan, D., Narayana, C. & Kulkarni, G. U. Low cost, rapid synthesis of graphene on Ni: An efficient barrier for corrosion and thermal oxidation. *Carbon* **78,** 384–391. ISSN: 00086223 (Nov. 2014).

113. Hust, J G; Lankford, A. B. Thermal conductivity of aluminum, copper, iron, and tungsten for temperatures from 1 K to the melting point. *National Bureau of Standards, Boulder, CO (USA). Chemical Engineering Science Div.* (1984).

114. Ramanathan, K. & Yen, S. High-temperature emissivities of copper, aluminum, and silver. *JOSA* **67,** 32–38 (1977).

115. Bauer, W., Oertel, H. & Rink, M. *Spectral emissivities of bright and oxidized metals at high temperatures* in *15th Symposium on Thermophysical Properties* (2003), 22–27.

116. Shanks, K., Senthilarasu, S. & Mallick, T. K. Optics for concentrating photovoltaics: Trends, limits and opportunities for materials and design. *Renewable and Sustainable Energy Reviews* **60,** 394–407 (2016).

117. Dauphin, M., Albin, S., El-Hafi, M., Le Maoult, Y. & Schmidt, F. *Towards thermal model of automotive lamps* in *QIRT 2012-11th International Conference on Quantitative InfraRed Thermography* (2012), 10–p.

118. Setién-Fernández, I., Echániz, T., González-Fernández, L., Pérez-Sáez, R. & Tello, M. Spectral emissivity of copper and nickel in the mid-infrared range between 250 and 900 C. *International Journal of Heat and Mass Transfer* **71,** 549–554 (2014).

119. Superior Quartz Products, I. *Air Cooled Short Arc Technical Information* 2013. `https://www.sqpuv.com/acsatechnical.php`.

120. Bergman, T. L., Incropera, F. P., Dewitt, D. P. & Lavine, A. S. *Fundamentals of Heat and Mass Transfer* 717–737 (John Wiley & Sons, 2011).

121. Gale, W. F. & Totemeier, T. C. *Smithells Metals Reference Book* 17/1–17/12 (Butterworth-Heinemann, 2004).

122. Larrabee, R. D. Spectral emissivity of tungsten. *JOSA* **49,** 619–625 (1959).

123. Dmitriev, V. & Kholopov, G. Radiant emissivity of tungsten in the infrared region of the spectrum. *Journal of Applied Spectroscopy* **2,** 315–320 (1965).

124. Aksyutov, L. Normal spectral emissivity of gold, platinum, and tungsten. *Journal of engineering physics* **27,** 913–917 (1974).

125. Watanabe, H., Susa, M., Fukuyama, H. & Nagata, K. Phase dependence (liquid/solid) of normal spectral emissivities of noble metals at melting points. *International Journal of Thermophysics* **24,** 223–237 (2003).

126. Watanabe, H., Susa, M., Fukuyama, H. & Nagata, K. Near-infrared spectral emissivity of Cu, Ag, and Au in the liquid and solid states at their melting points. *International Journal of Thermophysics* **24,** 1105–1120 (2003).

127. Torrance, K. E. & Rockett, J. A. Numerical study of natural convection in an enclosure with localized heating from below—creeping flow to the onset of laminar instability. *Journal of Fluid Mechanics* **36,** 33–54. ISSN: 0022-1120 (Mar. 1969).

128. Ordal, M. A. *et al.* Optical properties of the metals Al, Co, Cu, Au, Fe, Pb, Ni, Pd, Pt, Ag, Ti, and W in the infrared and far infrared. *Applied Optics* **22,** 1099. ISSN: 0003-6935 (Apr. 1983).

129. Abbott, G., Alvares, N. & Parker, W. *Total Normal and Total Hemispherical Emittance of Polished Metals-Part 2* tech. rep. WADD-TR-61-94 (Naval Radiological Defense Lab San Francisco, CA, 1963).

130. Abbott, G. *Total normal and total hemispherical emittance of polished metals-Part 3* tech. rep. WADD-TR-61-94 (Naval Radiological Defense Lab San Francisco, CA, 1963).

131. Gaumer, R., McKellar, L., Streed, E., Frame, K. & Grammer, J. in *Progress in International Research on Thermodynamic and Transport Properties* 575–587 (Elsevier, 1962).

132. Best, G. Emissivities of copper and aluminum. *JOSA* **39,** 1009–1011 (1949).

133. Mooradian, A. Photoluminescence of metals. *Physical Review Letters* **22.** ISSN: 00319007 (1969).

134. Novoselov, K. S. *et al.* Two-dimensional atomic crystals. *Proceedings of the National Academy of Sciences* **102,** 10451–10453 (2005).

135. Novoselov, K. S. *et al.* Two-dimensional gas of massless Dirac fermions in graphene. *nature* **438,** 197–200 (2005).

136. Al-Hilfi, S. H., Derby, B., Martin, P. A. & Whitehead, J. C. Chemical vapour deposition of graphene on copper-nickel alloys: The simulation of a thermodynamic and kinetic approach. *Nanoscale* **12,** 15283–15294. ISSN: 20403372 (2020).

137. Hofmann, S., Braeuninger-Weimer, P. & Weatherup, R. S. CVD-Enabled Graphene Manufacture and Technology. *The Journal of Physical Chemistry Letters* **6.** PMID: 26240694, 2714–2721 (2015).

138. Wu, CF Jeff and Hamada, M. S. *Experiments: planning, analysis, and optimization* (John Wiley & Sons, 2011).

139. Pandita, P. *et al.* STOCHASTIC MULTIOBJECTIVE OPTIMIZATION ON A BUDGET: APPLICATION TO MULTIPASS WIRE DRAWING WITH QUANTIFIED UNCERTAINTIES. *International Journal for Uncertainty Quantification* **8,** 233–249. ISSN: 2152-5080 (2018).

140. Mockus, J. *Bayesian approach to global optimization: theory and applications* (Springer Science & Business Media, 2012).

141. Rasmussen, C. E. & Williams, C. K. I. *Gaussian Processes for Machine Learning* (2018).

142. Suk, J. W. *et al.* Transfer of CVD-Grown Monolayer Graphene onto Arbitrary Substrates. *ACS Nano* **5,** 6916–6924. ISSN: 1936-0851 (Sept. 2011).

143. Nayan, N. A. & Ramli, N. Analysis of metal catalyst etching in graphene transfer process. *International Journal of Applied Engineering Research* **11,** 7815–7822. ISSN: 09739769 (2016).

144. Zhao, W. *et al.* Low-energy transmission electron diffraction and imaging of large-area graphene. *Science Advances* **3.** ISSN: 2375-2548 (Sept. 2017).

145. Yu, S. U. *et al.* Simultaneous visualization of graphene grain boundaries and wrinkles with structural information by gold deposition. *ACS nano* **8,** 8662–8668 (2014).

146. Liu, N. *et al.* The origin of wrinkles on transferred graphene. *Nano Research* **4,** 996–1004 (2011).

147. Huang, M. *et al.* Large-area single-crystal AB-bilayer and ABA-trilayer graphene grown on a Cu/Ni(111) foil. *Nature Nanotechnology* **15,** 289–295. ISSN: 17483395 (2020).

148. Liao, C.-D., Lu, Y.-Y., Tamalampudi, S. R., Cheng, H.-C. & Chen, Y.-T. Chemical Vapor Deposition Synthesis and Raman Spectroscopic Characterization of Large-Area Graphene Sheets. *The Journal of Physical Chemistry A* **117.** PMID: 23461419, 9454–9461 (2013).

149. Ferrari, A. C. *et al.* Raman spectrum of graphene and graphene layers. *Physical Review Letters* **97,** 187401(1–4). ISSN: 00319007 (2006).

150. Mattevi, C., Kim, H. & Chhowalla, M. A review of chemical vapour deposition of graphene on copper. *J. Mater. Chem.* **21,** 3324–3334 (10 2011).

151. Li, Q. *et al.* Growth of Adlayer Graphene on Cu Studied by Carbon Isotope Labeling. *Nano Letters* **13.** PMID: 23278710, 486–490 (2013).

152. Nie, S. *et al.* Growth from below: bilayer graphene on copper by chemical vapor deposition. *New Journal of Physics* **14,** 093028 (Sept. 2012).

153. Malard, L. M. *et al.* Probing the electronic structure of bilayer graphene by Raman scattering. *Physical Review B - Condensed Matter and Materials Physics* **76,** 20140. ISSN: 10980121 (2007).

154. Subramaniam, B., Licence, P., Moores, A. & Allen, D. T. Shaping Effective Practices for Incorporating Sustainability Assessment in Manuscripts Submitted to ACS Sustainable Chemistry & Engineering: An Initiative by the Editors. *ACS Sustainable Chemistry & Engineering* **9,** 3977–3978 (2021).

155. Debecker, D. P. *et al.* Shaping Effective Practices for Incorporating Sustainability Assessment in Manuscripts Submitted to ACS Sustainable Chemistry & Engineering: Catalysis and Catalytic Processes. *ACS Sustainable Chemistry & Engineering* **9,** 4936–4940 (2021).

156. Yamada, T., Ishihara, M. & Hasegawa, M. Large area coating of graphene at low temperature using a roll-to-roll microwave plasma chemical vapor deposition. *Thin Solid Films* **532.** The 9th International Conference on Coatings on Glass and Plastics, 89–93. ISSN: 0040-6090 (2013).

157. Yamada, T., Ishihara, M., Kim, J., Hasegawa, M. & Iijima, S. A roll-to-roll microwave plasma chemical vapor deposition process for the production of 294mm width graphene films at low temperature. *Carbon* **50,** 2615–2619. ISSN: 0008-6223 (2012).

158. Hesjedal, T. Continuous roll-to-roll growth of graphene films by chemical vapor deposition. *Applied Physics Letters* **98,** 133106 (2011).

159. Kobayashi, T. *et al.* Production of a 100-m-long high-quality graphene transparent conductive film by roll-to-roll chemical vapor deposition and transfer process. *Applied Physics Letters* **102,** 023112 (2013).

160. Polsen, E. S., McNerny, D. Q., Viswanath, B., Pattinson, S. W. & John Hart, A. High-speed roll-to-roll manufacturing of graphene using a concentric tube CVD reactor. *Scientific reports* **5,** 1–12 (2015).

161. Karwe, M. V. & Jaluria, Y. Thermal Transport From a Heated Moving Surface. *Journal of Heat Transfer* **108,** 728–733. ISSN: 0022-1481 (Nov. 1986).

162. Tsou, F., Sparrow, E. & Goldstein, R. Flow and heat transfer in the boundary layer on a continuous moving surface. *International Journal of Heat and Mass Transfer* **10,** 219–235. ISSN: 0017-9310 (1967).

163. Char, M.-I., Chen, C.-K. & Cleaver, J. W. Conjugate forced convection heat transfer from a continuous, moving flat sheet. *International Journal of Heat and Fluid Flow* **11,** 257–261. ISSN: 0142-727X (1990).

164. Sakiadis, B. Boundary-layer behavior on continuous solid surfaces: II. The boundary layer on a continuous flat surface. *AiChE journal* **7,** 221–225 (1961).

165. Karwe, M. V. & Jaluria, Y. Numerical Simulation of Thermal Transport Associated With a Continuously Moving Flat Sheet in Materials Processing. *Journal of Heat Transfer* **113,** 612–619. ISSN: 0022-1481 (Aug. 1991).

166. Meng, J.-A., Liang, X.-G., Chen, Z.-J. & Li, Z.-X. Experimental study on convective heat transfer in alternating elliptical axis tubes. *Experimental Thermal and Fluid Science* **29,** 457–465. ISSN: 0894-1777 (2005).

167. Comini, G., Savino, S., Magriotis, N. & Muratori, S. Thermal modeling of vacuum web coating. *Applied Thermal Engineering* **27,** 611–618. ISSN: 1359-4311 (2007).

168. Alrefae, M. A. & Fisher, T. S. A Heat Transfer Model for Graphene Deposition on Ni and Cu Foils in a Roll-to-Roll Plasma Chemical Vapor Deposition System. *Journal of Heat Transfer* **143.** 103401. ISSN: 0022-1481 (Sept. 2021).

169. Cobos Torres, E. O. & Pagilla, P. R. Temperature Distribution in Moving Webs Heated by Radiation Panels: Model Development and Experimental Validation. *Journal of Dynamic Systems, Measurement, and Control* **139.** 051003. ISSN: 0022-0434 (Mar. 2017).

170. Alrefae, M. A. & Fisher, T. S. A Heat Transfer Model for Graphene Deposition on Ni and Cu Foils in a Roll-to-Roll Plasma Chemical Vapor Deposition System. *Journal of Heat Transfer* **143.** 103401. ISSN: 0022-1481 (Sept. 2021).

171. Zhu, S.-E., Yuan, S. & Janssen, G. C. A. M. Optical transmittance of multilayer graphene. *Europhysics Letters* **108,** 17007 (Sept. 2014).

172. Roddaro, S., Pingue, P., Piazza, V., Pellegrini, V. & Beltram, F. The Optical Visibility of Graphene: Interference Colors of Ultrathin Graphite on SiO2. *Nano Letters* **7.** PMID: 17665963, 2707–2710 (2007).

173. Krasheninnikov, A. V. & Nordlund, K. Ion and electron irradiation-induced effects in nanostructured materials. *Journal of Applied Physics* **107,** 071301 (2010).

174. Johansson, K. O., Head-Gordon, M. P., Schrader, P. E., Wilson, K. R. & Michelsen, H. A. Resonance-stabilized hydrocarbon-radical chain reactions may explain soot inception and growth. *Science* **361,** 997–1000 (2018).

175. Chen, C., Zhang, Z., Huang, Z., Jian, N. & Diao, D. Photon excitation effect on formation of graphene nanocrystallites during carbon film growth process. *AIP Advances* **12,** 055014 (2022).

176. Golnabi, H. Diffuse reflectance measurements from different surfaces. *Journal of Sciences Islamic Republic of Iran* **12,** 359–364 (2001).

177. Van Ginneken, B., Stavridi, M. & Koenderink, J. J. Diffuse and specular reflectance from rough surfaces. *Applied Optics* **37,** 130–139. ISSN: 0003-6935 (Jan. 1998).

178. Beder, E. C., Bass, C. D. & Shackleford, W. L. Transmissivity and absorption of fused quartz between 0.22 μ and 3.5 μ from room temperature to 1500°C. *Applied Optics* **10,** 2263–2268 (1971).

179. Madhavan, S., Qu, J. J. & Hao, X. Saharan dust detection using multi-sensor satellite measurements. *Heliyon* **3,** e00241. ISSN: 24058440 (Feb. 2017).